SEARCH FOR THE FLAVOR-CHANGING NEUTRAL CURRENT IN TOP PAIR EVENTS IN $\sqrt{s} = 8$ TEV PROTON-PROTON COLLISIONS AT THE LARGE HADRON COLLIDER USING THE ATLAS DETECTOR

by

ELIZABETH CAITLIN BROST

A DISSERTATION

Presented to the Department of Physics
and the Graduate School of the University of Oregon
in partial fulfillment of the requirements
for the degree of
Doctor of Philosophy

March 2016

DISSERTATION APPROVAL PAGE

Student: Elizabeth Caitlin Brost

Title: Search for the Flavor-Changing Neutral Current in Top Pair Events in $\sqrt{s} = 8$ TeV Proton-Proton Collisions at the Large Hadron Collider Using the ATLAS Detector

This dissertation has been accepted and approved in partial fulfillment of the requirements for the Doctor of Philosophy degree in the Department of Physics by:

Stephanie Majewski	Chair
James Brau	Advisor
Graham Kribs	Core Member
Miriam Deutsch	Core Member
Marina Guenza	Institutional Representative

and

Scott L. Pratt	Dean of the Graduate School

Original approval signatures are on file with the University of Oregon Graduate School.

Degree awarded March 2016

DISSERTATION ABSTRACT

Elizabeth Caitlin Brost

Doctor of Philosophy

Department of Physics

March 2016

Title: Search for the Flavor-Changing Neutral Current in Top Pair Events in $\sqrt{s} = 8$ TeV Proton-Proton Collisions at the Large Hadron Collider Using the ATLAS Detector

In this dissertation, a search for the flavor-changing neutral current in top-antitop events is presented. The flavor-changing neutral current is forbidden at tree level in the Standard Model and suppressed at higher order due to the GIM mechanism. In the Standard Model, the top quark is expected to decay to a W boson and a bottom quark nearly 100 percent of the time. While the Standard Model branching fractions for flavor-changing neutral currents in top decays are well beyond current experimental reach, there exist theoretical models which predict large enhancements to those branching fractions. Observation of the flavor-changing neutral current in top decays would be an unambiguous confirmation of new physics.

This search was conducted in data from proton-proton collisions at the Large Hadron Collider, running at a center-of-mass energy of $\sqrt{s} = 8$ TeV, which were collected with the ATLAS detector in 2012. These data correspond to an integrated luminosity of 20.3 fb^{-1}. Candidate events include a lepton (electron or muon), a photon, at least two jets (one of which is b-tagged), and missing transverse energy. As no signal is observed, an observed (expected) upper limit on the branching ratio $\text{BR}(t \rightarrow q\gamma)$ of 0.063% (0.062%) is presented.

CURRICULUM VITAE

NAME OF AUTHOR: Elizabeth Caitlin Brost

GRADUATE AND UNDERGRADUATE SCHOOLS ATTENDED:

University of Oregon, Eugene, Oregon
Grinnell College, Grinnell, Iowa

DEGREES AWARDED:

Doctor of Philosophy in Physics, 2016, University of Oregon
Bachelor of Arts in Physics and French, 2010, Grinnell College

AREAS OF SPECIAL INTEREST:

High-energy hadron collider physics, properties of the top quark, BSM top couplings, trigger, tau trigger signatures, signatures of boosted objects, jet substructure, Monte Carlo event generation

PROFESSIONAL EXPERIENCE:

University of Oregon Graduate Research Assistant, ATLAS experiment, January 2012 - present

University of Oregon Graduate Research Assistant, International Linear Collider and ATLAS experiment, June 2010 - December 2011

University of Oregon Graduate Teaching Assistant,
September 2010 - March 2011

Cornell Laboratory for Accelerator-Based Sciences and Education
REU student, Cornell High-Energy Synchrotron Source,
June - August 2009

Purdue University REU student, STAR experiment,
June - August 2008

PUBLICATIONS:

ATLAS Collaboration, G. Aad *et al.*, "Identification and energy calibration of hadronically decaying tau leptons with the ATLAS experiment in pp collisions at $\sqrt{s}$=8 TeV," (2014) `arXiv:1412.7086 [hep-ex]`.

ATLAS Collaboration, E. Brost, "Top Quark Pair Properties - Spin Correlation, Charge Asymmetry, and Complex Final States - at ATLAS," (2013) vol. 71, p. 00023.

Snowmass Top Quark Working Group, K. Agashe *et al.*, "Working Group Report: Top Quark," (2013) `arXiv:1311.2028 [hep-ph]`.

P. J. H. Tjossem and E. C. Brost, "Optimizing Thomson's jumping ring," *American Journal of Physics* **79** no. 4, (2011) 353–358.

ACKNOWLEDGEMENTS

For his constant support, advice, and guidance over the past five and half years: Thank you to my advisor, Jim Brau.

For teaching me about physics and computers and life at CERN: Thank you to the University of Oregon ATLAS group (past and present): Jim Brau, David Strom, Eric Torrence, Stephanie Majewksi, Mansoora Shamim, Chris Potter, Walter Hopkins, Kate Whalen, Jake Searcy, Andreas Reinsch, Peter Radloff, Elizabeth Ptacek, Chaowaroj Wanotayaroj, Ian Snyder, Ben Allen, Jason Barkeloo, John Myers, and Johan Bonilla.

For their companionship and commiseration: Thank you to my class at the University of Oregon: Jason Boucher, Jeremy Copperman, Andrea Goering, Yasin Karim, Erik Keever, Kyle Lynch-Klarup, Chris Newby, Dileep Reddy, and Alex Trevelyan.

For their love and their unending belief in me: Thank you to my family and to my Chris.

For my parents and my teachers, who have always believed in me.

TABLE OF CONTENTS

Chapter Page

Chapter Page

APPENDICES

LIST OF FIGURES

Figure Page

Figure Page

LIST OF TABLES

Table Page

CHAPTER I

INTRODUCTION

The Standard Model [1, 2, 3] of particle physics is famously successful, having stood up to the vast majority of experimental test to date. The experimental high-energy physicist has two choices, then: to measure the Standard Model predictions to greater and greater accuracy (compare theory and observation), or to push the boundaries of the Standard Model until it breaks.

It is interesting to study the inconsistencies that are observed between the Standard Model predictions and nature. Such problems include:

- Why do neutrinos have mass?
- What is dark matter, and does it interact with SM particles (and if so, how)?
- What is the origin of the matter-antimatter asymmetry?

The Standard Model describes the fundamental particles (quarks, leptons, and gauge bosons) and their interactions. There are six flavors of quarks: up, down, charm, strange, bottom, and top. There are three flavors of leptons: electron, muon, and tau. The quarks experience the electromagnetic, weak, and strong interactions, and the leptons experience the electromagnetic and weak interactions.

1.1. The Top Quark and the Standard Model

The top quark is the heaviest fundamental particle, with mass 173.21 ± 0.51 ± 0.71 GeV [4] (for comparison, the proton weighs about 1 GeV). The top quark was discovered in 1995 at the Tevatron [5, 6]. The top quark's enormous mass also

FIGURE 1. Top quark decays through the charged (a) and neutral (b) currents

means that it has a very short lifetime ($0.5 * 10^{-24}$ s) [4]. The top quark decays before it can hadronize, so studying top quarks is a unique opportunity to study bare quarks.

In the Standard Model (SM), the top quark is expected to decay to a W boson and a bottom quark (t $\rightarrow W$ b) nearly 100 percent of the time, as in Figure 1a. The flavor-changing neutral current (FCNC), where the top decays to a neutral boson and an up or charm quark ($t \rightarrow q\gamma$, for example, as in Figure 1b), is highly suppressed in the Standard Model. Flavor-changing neutral top decays can still occur very rarely through loops (at a level $< 10^{-14}$). The SM branching ratio is so far below the current experimental sensitivity that any observation of FCNC decays could be indicative of new physics. Even if FCNC decays are not observed, the setting of upper limits can help to constrain possible new physics models. The most stringent upper limits on the branching ratio BR($t \rightarrow q\gamma$) are 0.013% ($t \rightarrow u\gamma$) and 0.17% ($t \rightarrow c\gamma$), in single top production, set by the CMS Collaboration in 2015 [7].

1.2. Studying the Top Quark

Some of the top quark's properties were studied at the Tevatron, but more careful studies require a larger dataset.

The Large Hadron Collider (LHC) [8], located at CERN, outside Geneva, Switzerland, is the world's largest particle accelerator, at 27 km in circumference.

The LHC just completed Run 1 in February 2013, after 3 years of enormously successful running. Nearly 25 fb^{-1} of data from proton-proton collisions at a center-of-mass energy of 8 TeV were delivered in 2012 alone. This is an unprecedented dataset (both in size and energy), and it will allow us to make precision measurements that were not possible in the past. The Large Hadron Collider is a top quark factory, and it provides enough statistics to make precise measurements of the top quark's properties, such as mass, spin, and charge. It is also possible to search for unexpected behaviors (such as new decay processes) which would hint at new physics, like supersymmetric or technicolor models. Since the top coupling to the Higgs boson is of order 1, it is of great interest for new theoretical models. The top pair production cross-section at 8 TeV is about 240 pb [4], so this dataset corresponds to $\sim$ 6 million top quark pairs delivered to each of the large experiments, ATLAS and CMS in 2012.

1.3. Searching for FCNC with Top Quarks

Many searches for new physics beyond the Standard Model (commonly abbreviated BSM) in the top sector have already been performed by the ATLAS Collaboration during LHC Run I. For example, ATLAS has performed several searches for the flavor-changing neutral current (FCNC). FCNCs are interesting, because they violate a fundamental property of the Standard Model: in the Standard Model, the neutral current conserves flavor at tree level. FCNCs can occur in the Standard Model through loops, but even that is very rare. However, there exist theoretical models which predict enhancements to that branching ratio of many orders of magnitude: for example, R-parity-violating SUSY models [9] and two Higgs doublet models [10]. Observation of the FCNC in top decays would be an unambiguous confirmation of new physics.

In this dissertation, a search for the flavor-changing neutral current in top decays in 20.3 $\text{fb}^{-1}$of data from pp collisions at $\sqrt{s} = 8$ TeV by the ATLAS detector at the Large Hadron Collider (LHC) will be presented. In Chapter II, the theoretical background is studied. In Chapter III, the LHC and the ATLAS detector are described. In Chapter IV, the simulation of signal and background simulation are discussed. In Chapter V, the details of the search method are described. In Chapter VI, the search results are presented. In Chapter VII, conclusions are made and plans for future work are recommended.

CHAPTER II

THEORETICAL BACKGROUND

In this chapter, the Standard Model of particle physics is described. I discuss why there is no flavor-changing neutral current at tree-level in the Standard Model, and why it is particularly interesting to study the flavor-changing neutral current with top quarks.

2.1. The Standard Model

The Standard Model Lagrangian is a function of fields and their derivatives only, and depends on those fields taken at one space-time point x^μ only:

$$\mathcal{L}[\phi_i(x), \partial_\mu \phi_i(x)]$$

It is invariant under certain internal symmetry groups.

The Standard Model predicts a local symmetry:

$$SU(3)_C \times SU(2)_L \times U(1)_Y$$

which will eventually be spontaneously broken:

$$SU(3)_C \times SU(2)_L \times U(1)_Y \rightarrow SU(3)_C \times U(1)_{EM}.$$

The most general Standard Model Lagrangian can be written as

$$\mathcal{L}_{SM} = \mathcal{L}_{kinetic} + \mathcal{L}_\psi + \mathcal{L}_\phi + \mathcal{L}_{Yukawa}$$

where the four terms are the kinetic, fermion, scalar, and Yukawa interactions.

The particle spectrum of $SU(3)_C \times SU(2)_L \times U(1)_Y$ is as follows:

$$\begin{array}{rl} \text{Quarks:} & Q_{L_i}(3,2)_{+\frac{1}{6}},\ U_{R_i}(3,1)_{+\frac{2}{3}},\ D_{R_i}(3,1)_{-\frac{1}{3}} \\ \text{Leptons:} & L_{L_i}(1,2)_{-\frac{1}{2}},\ E_{R_i}(1,1)_{-1} \\ \text{Scalars:} & \phi(1,2)_{+\frac{1}{2}} \end{array}$$

and there are twelve generators,

$$\begin{array}{ll} 8 & L_a = \frac{1}{2}\lambda_a \ (0) \text{ for } SU(3)_C \text{ triplets (singlets)} \\ 3 & T_b = \frac{1}{2}\sigma_b \ (0) \text{ for } SU(2)_L \text{ triplets (singlets)} \\ 1 & Y \text{ for } U(1)_Y \end{array}$$

three coupling constants,

$$\begin{array}{r} g_S \text{ for } SU(3)_C \\ g \text{ for } SU(2)_L \\ g' \text{ for } U(1)_Y \end{array}$$

twelve gauge bosons, $G^\mu_a(8,1)_0$, $W^\mu_b(1,3)_0$, and $B^\mu(1,1)_0$, and a covariant derivative, $D^\mu = \partial^\mu + ig_S G^\mu_a L_a + igW^\mu_a T_a + ig'YB^\mu$. Then, the kinetic term is:

$$\begin{aligned} \mathcal{L}_{kinetic} \;=\; & -\tfrac{1}{4}G^{\mu\nu}_a G_{a\mu\nu} - \tfrac{1}{4}W^{\mu\nu}_a W_{a\mu\nu} - \tfrac{1}{4}B^{\mu\nu}B_{\mu\nu} + (D^\mu\phi)^\dagger(D_\mu\phi) + \\ & i\overline{Q_{L_i}}\not{D}Q_{L_i} + i\overline{U_{R_i}}\not{D}U_{R_i} + i\overline{D_{R_i}}\not{D}D_{R_i} + \\ & i\overline{L_{L_i}}\not{D}L_{L_i} + i\overline{E_{R_i}}\not{D}E_{R_i} \end{aligned}$$

Thus far, $\mathcal{L}_\psi = 0$, since the quarks and leptons are in a chiral representations and charged under $U(1)_Y$, and therefore have no Dirac or Majorana mass terms.

To find those masses, one can write the Yukawa interaction Lagrangian:

$$\mathcal{L}_{Yukawa} = Y^u_{ij}\overline{Q_{L_i}}U_{R_j}\phi + Y^d_{ij}\overline{Q_{L_i}}D_{R_j}\phi + Y^e_{ij}\overline{L_{L_i}}E_{R_j}\phi + h.c.$$

where $Y^{u,d,e}$ are complex 3×3 matrices of dimensionless couplings. Without loss of generality, one can choose a basis where these matrices are diagonal:

$$\begin{aligned} Y^e \to V_{eL}Y^eV^\dagger_{eR} &= \hat{Y}^e = \text{diag}(y_e, y_\mu, y_\tau) \\ Y^u \to V_{uL}Y^eV^\dagger_{uR} &= \hat{Y}^u = \text{diag}(y_u, y_c, y_t) \\ Y^d \to V_{dL}Y^eV^\dagger_{dR} &= \hat{Y}^d = \text{diag}(y_d, y_s, y_b) \end{aligned}$$

The entries y are the Yukawa couplings to each fermion.

This leads to the CKM matrix, $V = V_{uL}V^\dagger_{dL}$, which will be discussed in more detail in Section 2.1.3. Then, in the basis where $Y^u = \hat{Y}^u$, $Y^d = V\hat{Y}^d$, and vice versa.

$$\begin{aligned} V &= \begin{pmatrix} V_{ud} & V_{us} & V_{ub} \\ V_{cd} & V_{cs} & V_{cb} \\ V_{td} & V_{ts} & V_{tb} \end{pmatrix} \\ &= \begin{pmatrix} 0.97427 \pm 0.00015 & 0.22534 \pm 0.00065 & 0.00351^{+0.00015}_{-0.00014} \\ 0.22520 \pm 0.00065 & 0.97344 \pm 0.00016 & 0.0412^{+0.0011}_{-0.0005} \\ 0.00867^{+0.00029}_{-0.00031} & 0.0404^{+0.0011}_{-0.0005} & 0.999146^{+0.000021}_{-0.000046} \end{pmatrix} \end{aligned}$$

Finally, the scalar Lagrangian is:

$$\mathcal{L}_\phi \; = \; -\mu^2\phi^\dagger\phi \; - \; \lambda(\phi^\dagger\phi)^2$$

Choosing $\mu^2 < 0$ and $\lambda > 0$ leads to spontaneous symmetry breaking with $| < \phi > | = \frac{\nu}{\sqrt{2}}$. Since ϕ is an $SU(3)_C$ singlet, $SU(3)_C$ is unbroken. The full local symmetry, $SU(3)_C \times SU(2)_L \times U(1)_Y$, however, is broken to $SU(3)_C \times U(1)_{EM}$.

2.1.1. Particles

The local $SU(3)_C \times U(1)_{EM}$ symmetry implies a massless color octet gluon, and a massless neutral photon. The spontaneous symmetry breaking $SU(2)_L \times U(1)_Y \rightarrow SU(3)_C \times U(1)_{EM}$ implies 3 massive vector bosons $(W^\pm, Z)$ and one massive Higgs boson. The charged fermions acquire Dirac masses $m_f = \frac{y_f \nu}{\sqrt{2}}$. Thusly, the full particle spectrum is shown in Table 1.

TABLE 1. The particles in the Standard Model

particle	spin	color	charge	mass
$W^{\pm}$	1	(1)	± 1	$1/2g$
Z	1	(1)	0	$\frac{1}{2}\sqrt{g^2+g'^2}$
γ	1	(1)	0	0
g	1	(8)	0	0
h	0	(1)	0	$\sqrt{2\lambda}$
e, μ, τ	1/2	(1)	-1	$y_{e,\mu,\tau}/\sqrt{2}$
ν_e, ν_μ, ν_τ	1/2	(1)	0	0
u, c, t	1/2	(3)	+2/3	$y_{u,c,t}/\sqrt{2}$
d, s, b	1/2	(3)	-1/3	$y_{d,s,b}/\sqrt{2}$

2.1.1.1. Leptons and Quarks

The charged fermions, which existed in chiral representations of $SU(2)_L \times U(1)_Y$ are now in vectorial representations of $SU(3)_C \times U(1)_{EM}$.

In the Standard Model, there are three massive, charged leptons, called the electron, the muon, and the tau. There are also three massless, neutral leptons, called neutrinos. There are six charged, massive quarks.

$$\begin{aligned} e, \mu, \tau : &\quad (1)_{-1} \\ \nu_e, \nu_\mu, \nu_\tau : &\quad (1)_0 \\ u, c, t : &\quad (3)_{+\frac{2}{3}} \\ d, s, b : &\quad (3)_{-\frac{1}{3}} \end{aligned}$$

Free quarks do not exist in nature. One can observe quarks as part of bound states called hadrons. Hadrons can contain quark-antiquark pairs ($q\bar{q}$), called mesons, or sets of three quarks or antiquarks (qqq or $\bar{q}\bar{q}\bar{q}$), called baryons or antibaryons.

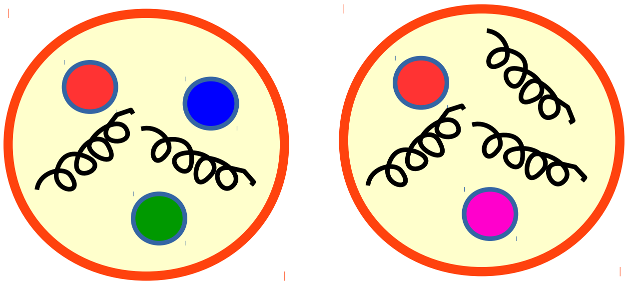

FIGURE 2. A baryon (qqq) and a meson ($q\bar{q}$)

The proton (uud) and the neutron (udd), which make up the nuclei of atoms, are baryons. An artist's rendition of a baryon and a meson is shown in Figure 2.

2.1.2. Interactions

The Standard Model also describes the ways that particles are allowed to interact. The fundamental interactions in the Standard Model are shown in Table 2.

TABLE 2. Interactions between Standard Model particles

interaction	force carrier	coupling	range
Yukawa	h	y_q	short
Electromagnetism	γ	eQ	long
Strong	g	g_S	long
Weak (neutral current)	Z	$\frac{e(T_3 - s_W^2 Q)}{s_W c_W}$	short
Weak (charged current)	$W^\pm$	qV	short

2.1.2.1. Yukawa Interaction

The charged fermions and the massive vector bosons acquire mass through their interactions with the Higgs boson:

$$\begin{aligned}\mathcal{L}_h \;=\; & \tfrac{1}{2}\partial_\mu h \partial^\mu h \;-\; \tfrac{1}{2}m_h^2 h^2 \;-\; \tfrac{m_h^2}{2\nu}h^2 \;-\; \tfrac{m_h^2}{8\nu^2}h^4 \\ & + m_W^2 W_\mu^- W^{\mu+}(\tfrac{2h}{\nu} \;+\; \tfrac{h^2}{\nu^2}) \;+\; \tfrac{1}{2}m_Z^2 Z_\mu Z^\mu(\tfrac{2h}{\nu} \;+\; \tfrac{h^2}{\nu^2}) \\ & - \tfrac{h}{\nu}(m_e \overline{e_L} e_R \;+\; m_\mu \overline{\mu_L}\mu_R \;+\; m_\tau \overline{\tau_L}\tau_R \\ & + m_u \overline{u_L} u_R \;+\; m_c \overline{c_L} c_R \;+\; m_t \overline{t_L} t_R \\ & + m_d \overline{d_L} d_R \;+\; m_s \overline{s_L} s_R \;+\; m_b \overline{b_L} b_R \;+\; \text{h.c.})\end{aligned}$$

The Higgs boson couples diagonally to mass eigenstates. These couplings are NOT universal, instead they are proportional to the mass of the particle ($y_f \propto m_f$). The Yukawa couplings are diagonal, however – Standard Model fermions are chiral, so no bare mass terms. This fact is supported by experimental evidence in the quark and lepton sectors. ATLAS [11] and CMS [12] have set stringent limits on the quark-flavor violating process $t \rightarrow qH$, where the top quark decays to a light quark and a Higgs boson, and on the lepton-flavor violating process $H \rightarrow \tau\mu$ [13, 14], where the Higgs boson decays to a tau and a muon.

2.1.2.2. Strong and Electromagnetic Interactions

The strong and electromagnetic interactions in the Standard Model are universal. The strong interaction is mediated by the gluon (g), which couples to color. Therefore, quarks, which are charged under QCD, participate in the strong interaction. Leptons, which are color singlets, do not.

$$\begin{aligned}\mathcal{L}_{QCD}\,(fermions) &= -\tfrac{1}{2} g_S \bar{q} \lambda \not{G}_a q \\ &\qquad (q \;=\; u, d, c, s, b, t)\end{aligned}$$

The electromagnetic interaction is mediated by the photon (γ), which couples to electric charge. The quarks and the charged leptons (e, μ, τ) participate in the electromagnetic interaction. Neutrinos do not.

$$\begin{aligned}\mathcal{L}_{QED}\,(fermions) &= -e\overline{e_i}\not{A}e_i \;+\; \tfrac{2}{3}e\overline{u_i}\not{A}u_i \;-\; \tfrac{e}{3}\overline{d_i}\not{A}d_i \\ &\qquad (e_i \;=\; e, \mu, \tau \;\; u_i \;=\; u, c, t \;\; d_i \;=\; d, s, b)\end{aligned}$$

2.1.2.3. Weak Interaction

The neutral current interaction is mediated by the Z boson. It is chiral, parity-violating, diagonal, and universal.

$$\begin{aligned}\mathcal{L}_{NC} \;=\; \tfrac{e}{s_W c_W}&[-(\tfrac{1}{2} \;-\; s_W^2)\overline{e_L}\not{Z}e_L \;+\; s_W^2\overline{e_R}\not{Z}e_R \;+\; \tfrac{1}{2}\overline{\nu_L}\not{Z}\nu_L \\ &+ (\tfrac{1}{2} \;-\; \tfrac{2}{3}s_W^2)\overline{u_L}\not{Z}u_L \;-\; \tfrac{2}{3}s_W^2)\overline{u_R}\not{Z}u_R \\ &- (\tfrac{1}{2} \;-\; \tfrac{1}{3}s_W^2)\overline{d_L}\not{Z}d_L \;+\; \tfrac{1}{3}s_W^2)\overline{d_R}\not{Z}d_R]\end{aligned}$$

The charged current weak interaction is mediated by the W boson. The interaction with leptons is simpler than that with quarks, since the interaction basis is the same as the mass basis for leptons. This can be seen in the charged current Lagrangian $\mathcal{L}_{CC}$:

$$
\begin{aligned}
\mathcal{L}_{CC} \;&=\; -\tfrac{g}{\sqrt{2}}[\overline{\nu_{eL}}\not{W}^{+}e_L^- \;+\; \overline{\nu_{\mu L}}\not{W}^{+}\mu_L^- \;+\; \overline{\nu_{\tau L}}\not{W}^{+}\tau_L^- \;+\; \text{h.c.}] \\
&\quad -\tfrac{g}{\sqrt{2}}[\begin{pmatrix} \overline{u_L} & \overline{c_L} & \overline{t_L} \end{pmatrix} V\not{W}^{+} \begin{pmatrix} d_L \\ s_L \\ b_L \end{pmatrix} \;+\; \text{h.c.}]
\end{aligned}
$$

where V is the CKM matrix. Only left-handed particles participate in the charged current weak interaction. Parity is violated. This process is NOT diagonal and NOT universal.

2.1.3. The CKM Matrix

The Cabibbo–Kobayashi–Maskawa (CKM) matrix [15, 16] is a 3×3 unitary matrix that relates the flavor and mass eigenstates of the down-type quarks.

$$
\begin{pmatrix} d' \\ s' \\ b' \end{pmatrix} = \begin{pmatrix} V_{ud} & V_{us} & V_{ub} \\ V_{cd} & V_{cs} & V_{cb} \\ V_{td} & V_{ts} & V_{tb} \end{pmatrix} \begin{pmatrix} d \\ s \\ b \end{pmatrix}
$$

One could equally well express this information in terms of the up-type quarks, but this is the traditional way. Its entries have been determined experimentally. The CKM matrix is nearly diagonal, which tells us that the up and down quarks, charm and strange quarks, and top and bottom quarks experience the strongest mixing. In particular, the parameter V_{tb} is nearly 1, while V_{ts} and V_{td} are very small.

$$V_{\mathrm{CKM}} = \begin{pmatrix} 0.97427 \pm 0.00015 & 0.22534 \pm 0.00065 & 0.00351^{+0.00015}_{-0.00014} \\ 0.22520 \pm 0.00065 & 0.97344 \pm 0.00016 & 0.0412^{+0.0011}_{-0.0005} \\ 0.00867^{+0.00029}_{-0.00031} & 0.0404^{+0.0011}_{-0.0005} & 0.999146^{+0.000021}_{-0.000046} \end{pmatrix}$$

2.2. The Top Quark

The top quark is the most awesome of all the quarks. It is also the heaviest, by an order of magnitude. Since it is so heavy, it decays before it can be observed, and it does not combine with other quarks to form hadrons. Thus, studying the top quark is a unique opportunity to study a bare quark.

The presence of the a third generation up-type quark could be inferred from many sources: 1) from symmetry – there are three down-type quarks, and three generations of leptons, so there are probably three up-type quarks as well 2) from precision measurements of electroweak observables in the Standard Model (such as the W mass, the Higgs mass, and the FCNC process $B_S \rightarrow \mu^+\mu^-$) and 3) from measurements of the flavor-changing neutral current in B meson decays, which suggested $\Delta m(c, t)$.

2.2.1. Discovery

The top quark was discovered in 1995 [5, 6] at the Tevatron at Fermilab, by the CDF and D0 experiments. The experiments at the Tevatron made the first measurements of the top quark, but they lacked the statistics to make detailed studies of its properties.

The LHC is a top quark factory, with nearly 6 million top quark events delivered to each of ATLAS and CMS in 2012 alone. This unprecedented dataset made possible accurate measurements of the top quark's properties, such as production cross section, mass, and charge. There are 5 experiments capable of studying the top quark: CDF, D0, ATLAS, CMS, and now LHCb, with a first measurement of top production in the forward region [17].

2.2.2. Production and Decay

The study of top quarks can be characterized by their production and decay mechanisms.

The top quark is dominantly produced in pairs with its antiquark, the anti-top or $\bar{t}$. Top/anti-top (top pair) production is a strong process, and therefore common. Top pair production is shown in Figure 3. Top quarks can also be produced singly through weak interactions, which is less common. Single top quark production is shown in Figure 4. Least commonly, top quarks can be produced in association with a boson, as in Figure 5.

At the LHC, in proton-proton collisions, $t\bar{t}$ pairs are dominantly produced through gluon-gluon fusion, as in Figure 3a. At the Tevatron, since they were colliding protons and anti-protons, the dominant production mechanism for $t\bar{t}$ pairs was through quark/antiquark annihilation, as in Figure 3b.

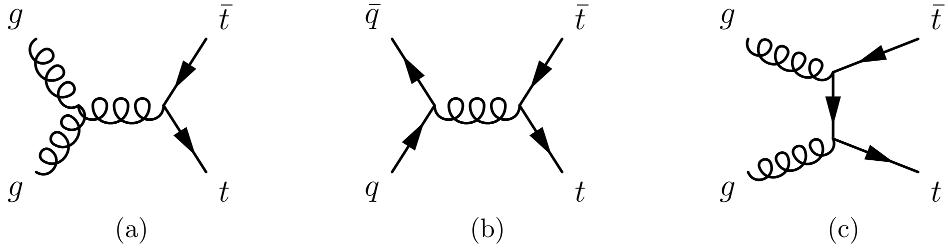

(a) (b) (c)

FIGURE 3. Top quark pair production mechanisms

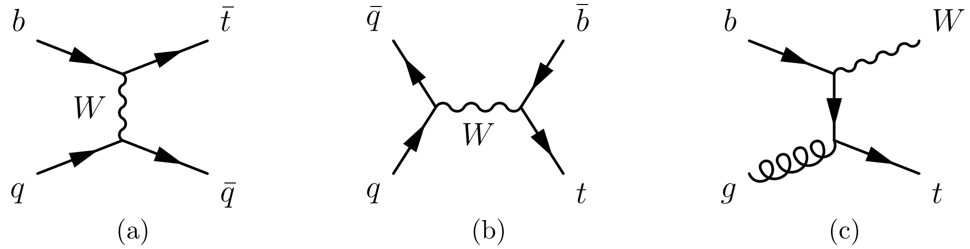

FIGURE 4. Single top quark production mechanisms

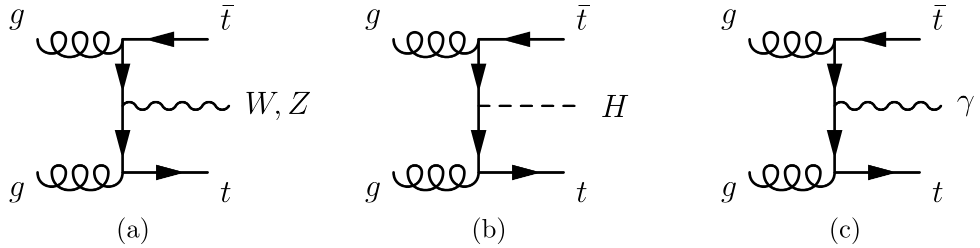

FIGURE 5. Top quark production in association with a boson

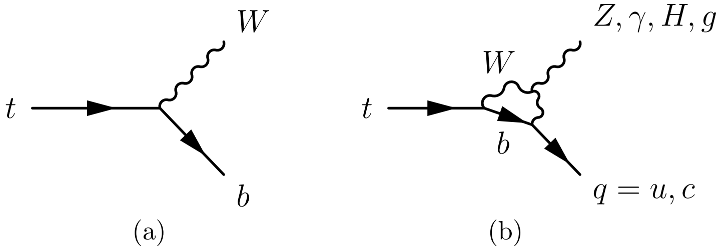

FIGURE 6. Top quark decays in the Standard Model

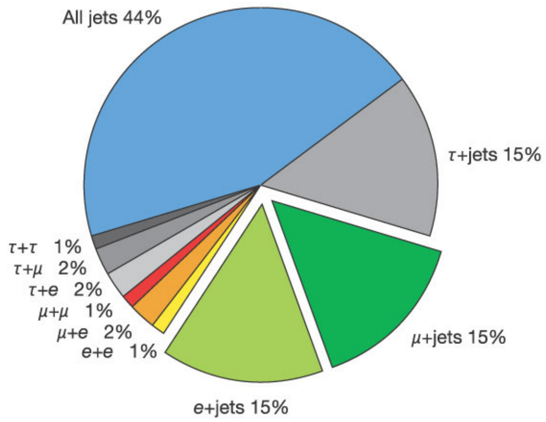

FIGURE 7. Top quark decays in the SM can be further categorized by the decay of the W boson

Since top quarks decay essentially one hundred percent of the time to a W boson and a bottom quark, as in Figure 6a, top pair events are typically further categorized by the decays of the W bosons, as shown in Figure 7. If both W bosons decay leptonically (to an electron or a muon and a neutrino– events with taus are generally treated separately), the event is categorized as "leptonic". If both W bosons decay to quarks (hadronically), the event is categorized as "all-hadronic". Finally, if one W boson decays leptonically and the other decays hadronically, the event is categorized as "lepton+jets" or "semi-leptonic".

2.2.3. Top Physics Beyond the Standard Model

It is particularly interesting to probe the properties of the top quark, to see if they agree with Standard Model predictions. There are many reasons to believe that the top quark will to play a large role in the discovery of whatever new physics is out there to discover. For example, the top quark's enormously large mass means that radiative corrections from new massive particles will show up in the top sector before they affect other, lighter fermions. Furthermore, the top quark's large mass implies a correspondingly large coupling to the Higgs boson ("Yukawa coupling," which is about 1), which suggests that the top quark might even play a special part in electroweak symmetry breaking.

2.3. The Flavor-Changing Neutral Current

As presented in the previous two sections, the flavor-changing neutral current is not permitted to occur at tree-level in the Standard Model. The flavor-changing neutral current is also CKM-suppressed for heavy quarks.

2.3.1. Flavor in the Standard Model

Here, the word "flavor" refers to copies of the same $SU(3)_C \times U(1)_{EM}$ representation, as shown in Table 3:

The flavor-changing neutral current is a process that involves either up- or down-type quarks (but not both), or involves charged or neutral leptons (but not both). The flavor of the quark or lepton is changed, but the electric charge is conserved. These processes are forbidden at tree-level in the Standard Model, but can occur through higher-order processes, such as loops.

FCNC cannot be mediated by any of the Standard Model bosons at tree-level. The W boson cannot mediate– charge must be conserved; so FCNC must be mediated by a neutral boson. The photon and gluon have diagonal, flavor-universal

TABLE 3. Quark and Lepton flavor in the Standard Model

	Electric charge	Flavors
up-type quarks	+2/3	u, c, t
down-type quarks	-1/3	d, s, b
charged leptons	-1	e, μ, τ
neutrinos	0	ν_e, ν_μ, ν_τ

couplings. The SM Higgs boson cannot couple to fermions of different flavors– SM fermions are chiral (which means there are no bare mass terms). Since there is a single Higgs doublet in the Standard Model, the Higgs boson is out as well.

2.3.2. The GIM Mechanism

In the late 1960s, studies of kaon decays suggested that there was no neutral current in the Standard Model. There was an observation of $K^+ \rightarrow \mu^+\nu_\mu$ but not $K_L^0 \rightarrow \mu^+\mu^-$. In the Cabibbo model, there were only three quarks (u,d,s), so even in the absence of a tree level decay through the neutral current, the box diagram $d\bar{s} \rightarrow \mu\mu$ should have been possible though the exchange of Ws.

$$\Delta S = 0 : u\bar{u} + d\bar{d}cos^2\Theta_C + s\bar{s}sin^2\Theta_C$$
$$\Delta S = 1 : (s\bar{d} + d\bar{s})sin\Theta_C cos\Theta_C$$

The non-observation of that process led Glashow, Iliopoulos, and Maiani to predict the existence of a fourth quark in 1970. The addition of that fourth quark, the charm quark, led to two quark doublets, as well as an almost perfect cancellation between the box diagrams involving a charm and an up quark in neutral kaon decays.

$$\Delta S = 0 : u\bar{u} + c\bar{c} + (d\bar{d} + s\bar{s})cos^2\Theta_C + (s\bar{s} + d\bar{d})sin^2\Theta_C$$
$$\Delta S = 1 : (s\bar{d} + d\bar{s} - d\bar{s} - s\bar{d})sin\Theta_C cos\Theta_C$$

Now, with the addition of the charm quark, the $\Delta S = 1$ terms cancel exactly (in the approximation where the charm and up quarks have the same mass). This can be seen in Figure 8, the box diagram contributions to neutral kaon decay.

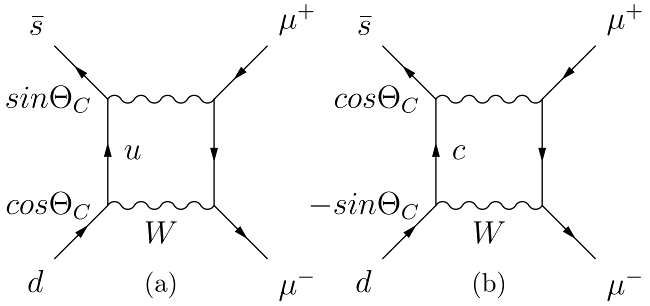

FIGURE 8. Neutral kaon decays through FCNC to a pair of muons

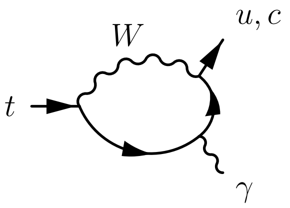

FIGURE 9. Top quark decay to a light quark and a photon, through a loop

The flavor-changing neutral current in top decays is CKM- as well as GIM-suppressed. Flavor-changing processes are proportional to off-diagonal entries in the CKM matrix, which are all very small. (FCNC $\propto \Delta m^2$ between quarks in the same sector). This suppression was used to predict the masses of the charm and top quarks:

$$\begin{aligned}\Delta m_K &\propto (m_c^2 - m_u^2)/m_W^2 \\ \Delta m_K &\propto (m_t^2 - m_c^2)/m_W^2\end{aligned}$$

The flavor-changing neutral current can occur in the Standard Model through loops, although this process is very rare. The SM branching ratios for top FCNC are shown in the first column of Table 4. The SM top quark FCNC decay is shown in Figure 9.

TABLE 4. Flavor-changing neutral current branching ratios in the Standard Model, as well as several BSM scenarios: two-Higgs-doublet models with flavor-violating Yukawa couplings [10, 18], quark singlet models [19, 20], minimal supersymmetric models with 1 TeV squarks and gluinos [21], R-parity-violating supersymmetric models [9], and models with extra dimensions [22]

Process	SM	2HDM	QS	MSSM	RPV	XD
$t \to u\gamma$	$4 * 10^{-16}$	-	$\leq 4 * 10^{-8}$	$\leq 10^{-8}$	$\leq 10^{-9}$	-
$t \to c\gamma$	$5 * 10^{-14}$	$\leq 10^{-7}$	$\leq 4 * 10^{-8}$	$\leq 10^{-8}$	$\leq 10^{-9}$	$\leq 10^{-9}$
$t \to uZ$	$7 * 10^{-17}$	-	$\leq 6 * 10^{-4}$	$\leq 10^{-7}$	$\leq 10^{-6}$	-
$t \to cZ$	$1 * 10^{-14}$	$\leq 10^{-6}$	$\leq 6 * 10^{-4}$	$\leq 10^{-7}$	$\leq 10^{-6}$	$\leq 10^{-5}$
$t \to ug$	$4 * 10^{-14}$	-	$\leq 9 * 10^{-7}$	$\leq 10^{-7}$	$\leq 10^{-6}$	-
$t \to cg$	$5 * 10^{-12}$	$\leq 10^{-4}$	$\leq 9 * 10^{-7}$	$\leq 10^{-7}$	$\leq 10^{-6}$	$\leq 10^{-10}$
$t \to uH$	$2 * 10^{-17}$	$\leq 6 * 10^{-6}$	-	$\leq 10^{-5}$	$\leq 10^{-9}$	-
$t \to cH$	$3 * 10^{-15}$	$\leq 2 * 10^{-3}$	-	$\leq 10^{-5}$	$\leq 10^{-9}$	$\leq 10^{-4}$

2.3.3. FCNC Beyond the Standard Model

Theoretical models of new physics are designed to solve problems that exist with the Standard Model, or to explain observed phenomena that are not in agreement with the Standard Model. For example, they might present solutions to such problems as the lack of a dark matter candidate in the SM or the unnaturally high fine-tuning of the Higgs mass due to loop corrections.

The flavor-changing neutral current in top decays happens so rarely in the Standard Model that it will be very difficult to observe, even with major advances in collider and detector technology. Beyond the Standard Model, however, there exist many and varied theoretical models which predict large enhancements to the flavor-changing top couplings. In most of these models, the enhancement comes from loop terms with heavy particles moving in the loops. It is particularly interesting to study models of new physics which solve one or more outstanding problems presented by the SM. Example branching ratios for top FCNC decays in a variety of models are shown in Table 4.

2-Higgs-Doublet Models: The two-Higgs-doublet models are a natural extension to the Standard Model that predict a second Higgs doublet. This results in an additional four Higgs bosons after the SM Higgs boson h: a heavy CP-even neutral boson H, a CP-odd pseudoscalar A, and two charged bosons $H^{\pm}$. Many supersymmetric and axion models posit the existence of an extra Higgs doublet. 2HDMS can also explain the baryon asymmetry of the universe, through the flexible mass spectrum of the scalar sector, and additional sources of CP violation [23].

Branching ratios for top FCNC decays in 2HDMs can be particularly large. Extended electroweak symmetry breaking sectors with flavor-violating couplings between the heavy Higgs H or pseudoscalar A can occur through loops involving the extra Higgses, or even at tree-level in these models. Since the couplings generally scale with quarks mass, limits on light quark FCNC are preserved, while allowing for potentially measurable top FCNC [10, 18].

Quark Singlet Models: It is also interesting to imagine extending the SM with an extra vector-like quark singlet (QS), which couples strongly to the top quark. Additional top-partner quarks could explain the fine-tuning to the Higgs mass, by canceling the top loop diagrams.

In models with vector-like quark singlets added to the Standard Model, the CKM matrix is no longer unitary, and top FCNC decays can occur at tree level [19, 20].

MSSM: Supersymmetric (SUSY) extensions to the Standard Model, where each Standard Model particle has a super-partner, are very popular, since they provide solutions to several outstanding questions. For example, the lightest supersymmetric particle is a good candidate for dark matter. In the Minimal Supersymmetric extension to the Standard Model (MSSM) with squarks and gluinos which have mass ~ 1 TeV, top FCNC decays can occur through loops involving stop quarks [21].

R-Parity-Violating SUSY Models: Top decays through FCNC can also occur at one loop in supersymmetric models where R-parity is violated (RPV). These loops can involve baryon or lepton number violation. The values shown in Table 4 correspond to the case where the squarks have mass 1 TeV [9].

Models with Extra Dimensions: Models with warped extra dimensions offer a potential solution to the hierarchy problem, by constructing a mechanism that explains the huge difference between the Planck scale and the electroweak symmetry breaking scale. In models with warped extra dimensions (XD), there can be flavor-violating couplings between the Standard Model fermions and Kaluza-Klein (KK) excitations of Standard Model bosons. In these models, flavor-violating couplings involving the top quark will be largest, because of its overlap with the KK gauge modes [22].

2.3.4. Top FCNC Measurements at ATLAS

It is possible to search for the flavor-changing neutral current in a variety of channels, which are shown in Figure 10. Different channels have their own advantages and challenges. For example, searching for FCNC in single top production allows for a sharp separation between the processes $pp \to u \to tg$

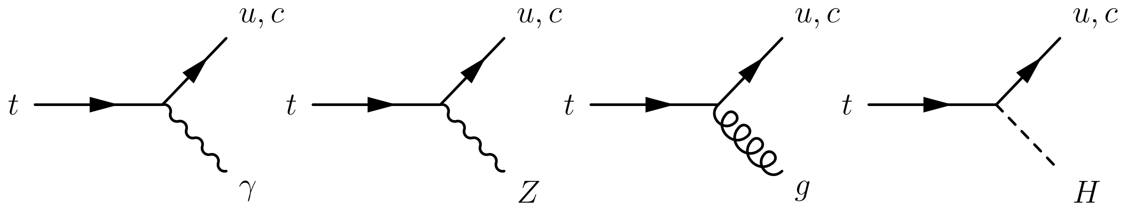

FIGURE 10. Flavor-changing neutral top quark decays (forbidden at tree-level)

and $pp \to c \to tg$, since there are more up quarks in the proton than charm quarks. The process $t \to qZ$ can be observed in a nearly background-less final state by exploiting the three-lepton topology of $t\bar{t} \to WbqZ \to \ell\nu bq\ell\ell$. A search for the process $t \to qH$ can take advantage of the many decay channels of the Higgs boson. Previous searches for FCNC in top quark decays that have been performed by the ATLAS collaboration are shown in Table 5. A summary of previous searches for top FCNC is shown in Figure 11.

TABLE 5. Previous ATLAS limits on top FCNC

Channel	Exp. Limit	Obs. Limit	Reference
BR($t \to cg$), single top	0.015	0.017%	[24]
BR($t \to ug$), single top	0.0035	0.004%	"
BR($t \to qZ$), $Z \to \ell^+\ell^-$	0.08%	0.07%	[25]
BR($t \to cH$), H $\to b\bar{b}$	0.41%	0.56%	[11]
BR($t \to uH$), H $\to b\bar{b}$	0.64%	0.61%	"
BR($t \to cH$), H $\to WW$,$\tau^+\tau^-$	0.54%	0.80%	[11]
BR($t \to uH$), H $\to WW$,$\tau^+\tau^-$	0.57%	0.79%	"
BR($t \to cH$), H $\to \gamma\,\gamma$	0.51%	0.79%	[26]
BR($t \to cH$), combined	0.25%	0.46%	[11]
BR($t \to uH$), combined	0.29%	0.45%	"

It is particularly interesting to search for the flavor-changing neutral current in top decays $t \to q\gamma$, because of the many interesting final-state topologies that correspond to this process.

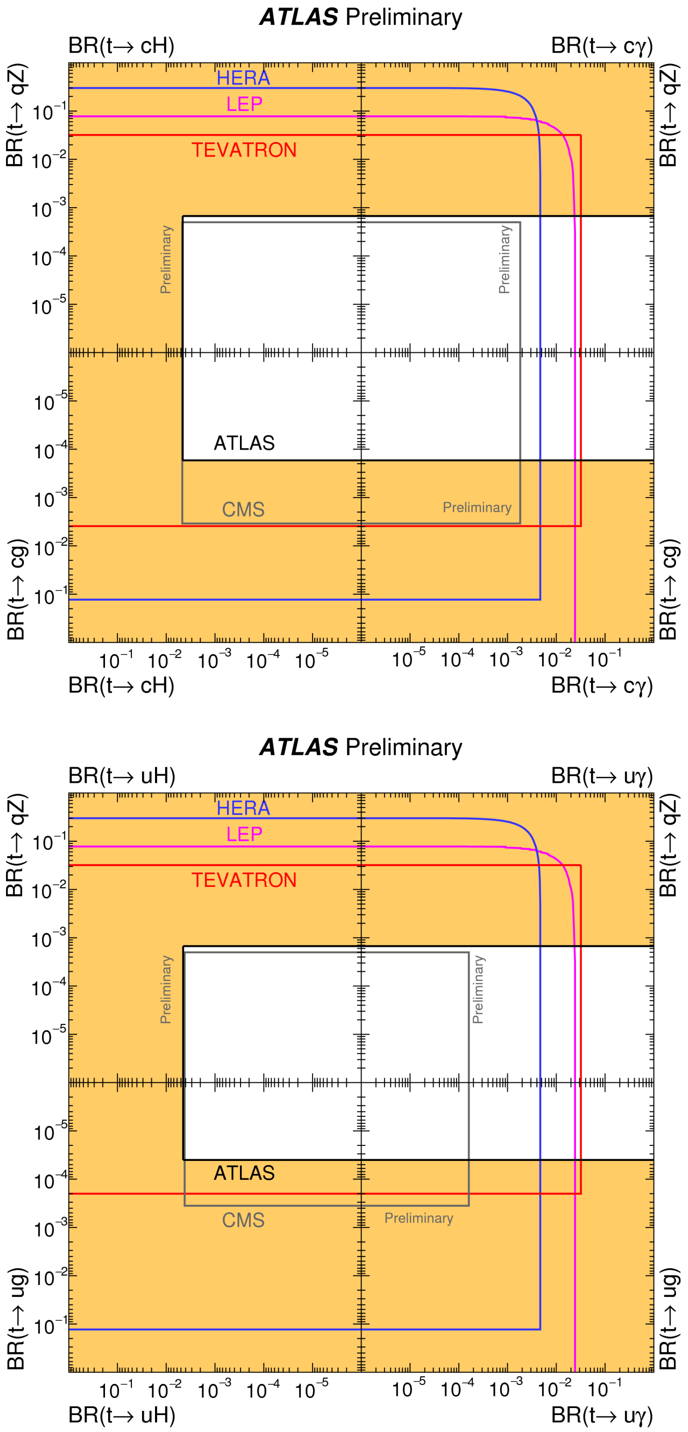

FIGURE 11. Summary of current limits on top FCNC decays, BR($t \rightarrow cX$) (left) and BR($t \rightarrow uX$) (right).

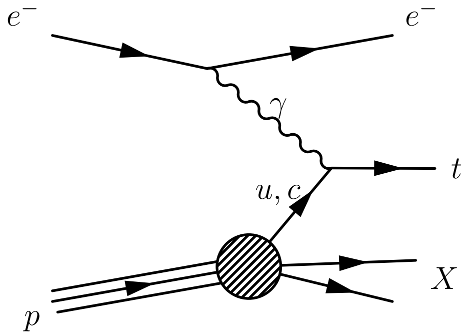

FIGURE 12. FCNC search at HERA in single top production

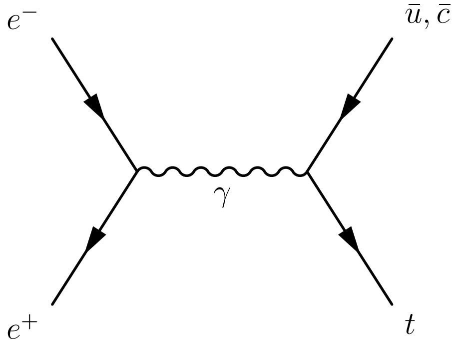

FIGURE 13. FCNC search at LEP in single top production

One can measure the coupling $tq\gamma$ in single top production. Searches for single top production via FCNC were performed at HERA, an electron-proton collider, at LEP, an electron-positron collider, and at the LHC, a proton-proton collider. Searches were performed by the ZEUS and H1 Collaborations in the process $ep \to etX$, as shown in Figure 12. Searches were performed by the LEP collaborations in the process $e^+e^- \to \gamma \to t\bar{q}$, as shown in Figure 13. A search was performed by the CMS Collaboration in the process $pp \to q \to t\gamma$, as shown in Figure 14. One can also search for FCNC in top quark decays. The CDF Collaboration at the Tevatron performed a search in the process $p\bar{p} \to t\bar{t} \to Wbq\gamma$, as shown in Figure 15. Previous limits set on the process $t \to q\gamma$ can be seen in Table 6.

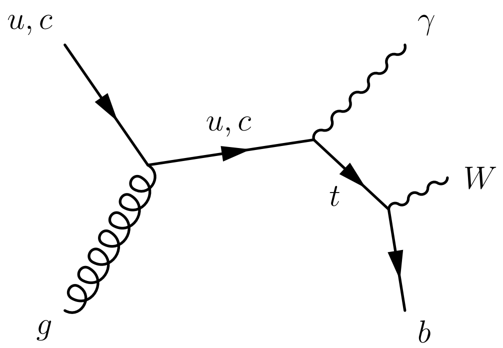

FIGURE 14. FCNC search by CMS in single top production

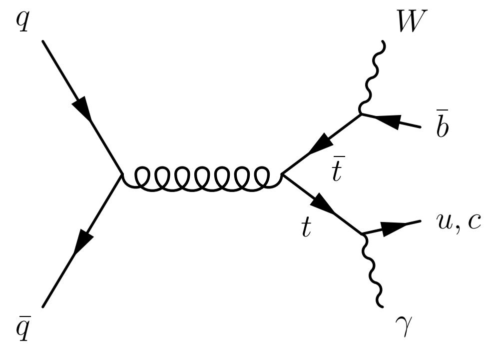

FIGURE 15. FCNC search by CDF in top decays

TABLE 6. Upper limit on BR($t \to q\gamma$) in previous searches

Experiment	Process	Upper Limit	Reference
CMS	$pp \to t\gamma$	BR($t \to u\gamma$)<0.013%	[7]
		BR($t \to c\gamma$)<0.17%	
ZEUS	$ep \to etX$	BR($t \to u\gamma$)<0.59%	[27]
H1	$ep \to etX$	BR($t \to u\gamma$)<0.64%	[28]
DELPHI	$e^+e^- \to \bar{t}q$	BR($t \to q\gamma$)<4.65%	[29]
L3	$e^+e^- \to \bar{t}q$	BR($t \to q\gamma$)<4.1%	[30]
CDF	$t\bar{t} \to Wbq\gamma$	BR($t \to q\gamma$)<3.2%	[31]

The search presented in this dissertation will exploit the final-state topology of top pair events where one top decays $t \to q\gamma$. In this process, $t\bar{t} \to Wbq\gamma \to \ell\nu q\gamma$, there is one of each object that can be reconstructed using the ATLAS detector (except for a tau lepton). There will be one charged lepton (and electron or a muon), one neutrino, two jets (one from the bottom quark and one from the up or charm quark), and one photon. Finally, the excellent mass resolution for the top quark that decays $t \rightarrow q\gamma$ allows for very good separation between this process and others.

CHAPTER III

THE LHC AND THE ATLAS DETECTOR

In this chapter, the experimental apparatus used to collect the data presented in this dissertation is described. The Large Hadron Collider and the ATLAS detector are described in detail, and physics object reconstruction techniques and Monte Carlo simulation techniques are summarized.

3.1. The Large Hadron Collider

The Large Hadron Collider (LHC) [8] is the world's largest particle accelerator, at 27 km in circumference. Located at CERN, 100 m under the French-Swiss border, the LHC accelerates protons clockwise and counter-clockwise around the ring at 99.999997828% of the speed of light. The proton beams are focused, steered and accelerated around the ring using superconducting magnets. The protons are then made to collide at four interaction points, where the four main LHC experiments (ATLAS [32], CMS [33], LHCb [34], and ALICE [35]) are located.

3.1.1. Accelerator Complex

It takes several separate machines to accelerate the protons to LHC collision energy. Figure 16 shows an artist's rendition of the accelerator complex at CERN, which accelerates the protons to high energy for injection into the LHC. The protons that will be collided in the LHC begin inside a small bottle of hydrogen at the main CERN site (each hydrogen atom is composed of one proton and one electron). Hydrogen atoms are placed in an electric field, which separates the protons and electrons. The protons are inserted into the Linac 2 (shown in

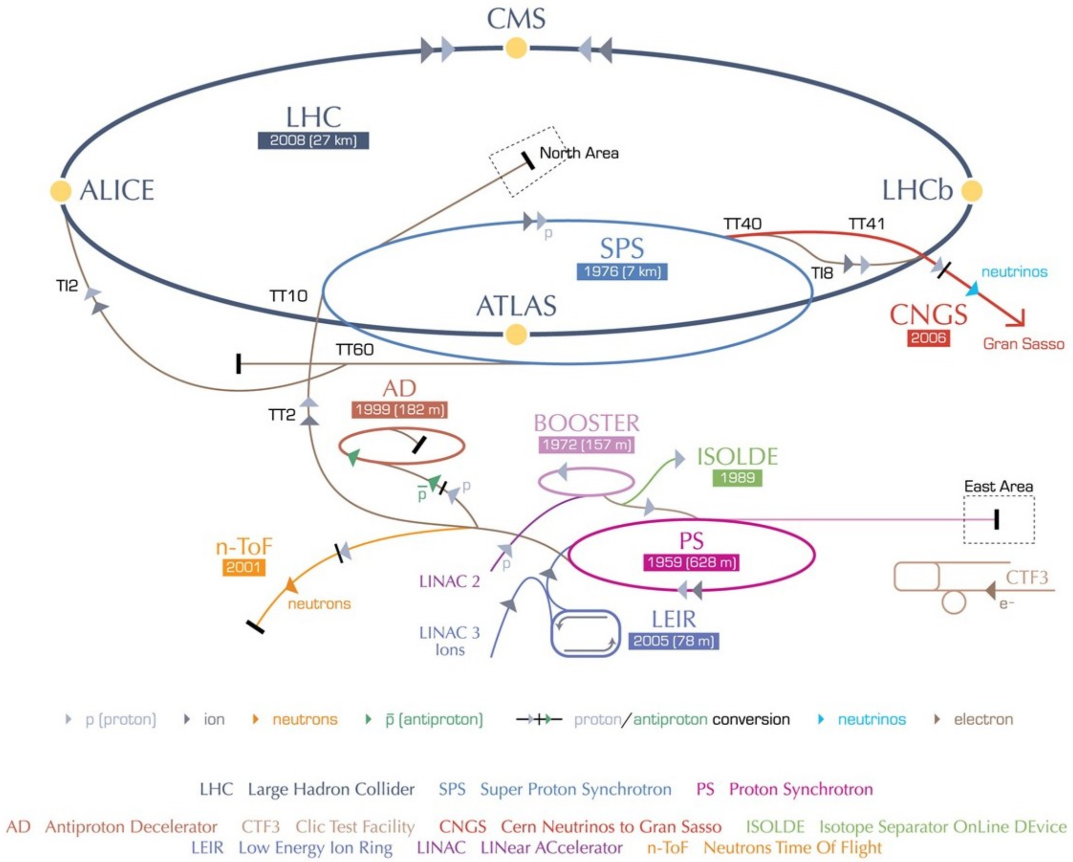

FIGURE 16. The accelerator complex at CERN [36]

purple) accelerates the protons to 50 MeV. They are then injected into the Proton Synchrotron Booster (shown in lilac), and accelerated to 1.4 GeV. Next, they go into the Proton Synchrotron (shown in magenta), and further accelerated to 25 GeV. The protons are then injected into the Super Proton Synchrotron (shown in light blue), where they are accelerated to 450 GeV. Finally, the protons arrive at the LHC (shown in dark blue), where they will be accelerated to collision energy.

The first proton-proton collisions in the LHC in 2008 occurred at the injection energy of $\sqrt{s} = 900$ GeV (450 GeV per beam). Then, after a few years of machine development and improvements, LHC Run I began. In 2010, the then-world-record collision energy of $\sqrt{s} = 7$ TeV was achieved. While there was only a small amount

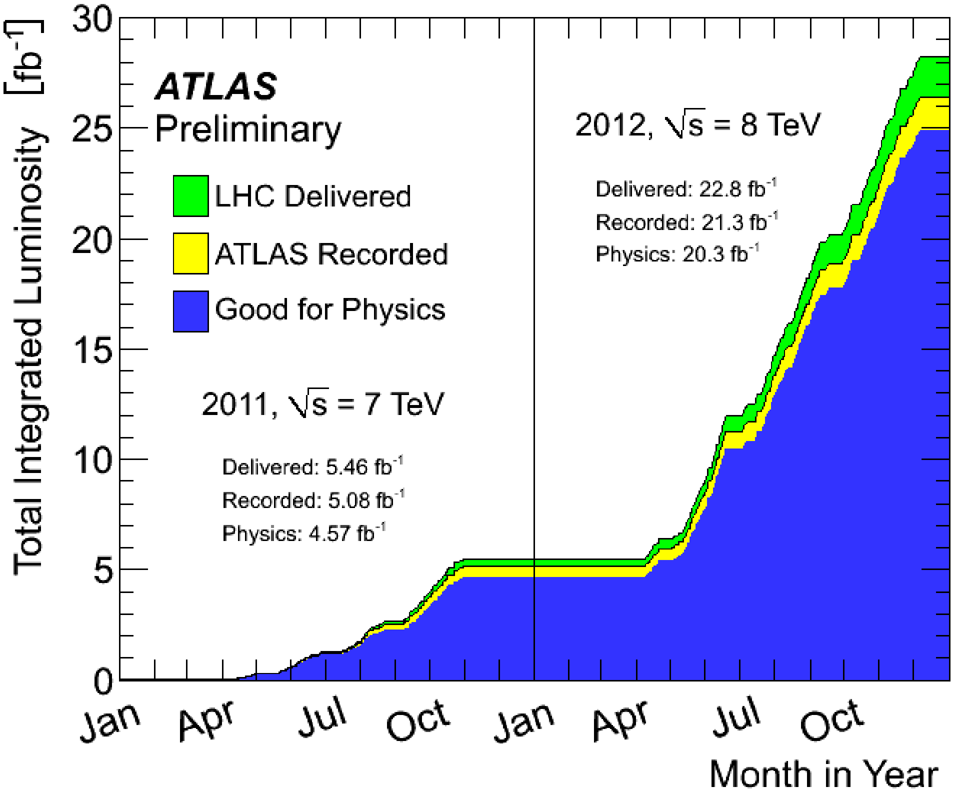

FIGURE 17. Total luminosity versus time delivered to (green), recorded by (yellow), and declared good for analysis by (blue) the ATLAS experiment in 2011 and 2012, during 7 TeV and 8 TeV *pp* collisions.

of data collected in 2010, the short run served as training for the years to come. In 2011, the LHC ran for most of the year at $\sqrt{s} = 7$ TeV, and delivered 5.46 fb^{-1} of data. In 2012, the LHC ran at $\sqrt{s} = 8$ TeV for the majority of the year, and delivered 22.8 $\text{fb}^{-1}$of data. The total luminosity delivered to the ATLAS experiment in 2011 and 2012 is shown in Figure 17, and the peak instantaneous luminosity over time is shown in Figure 18.

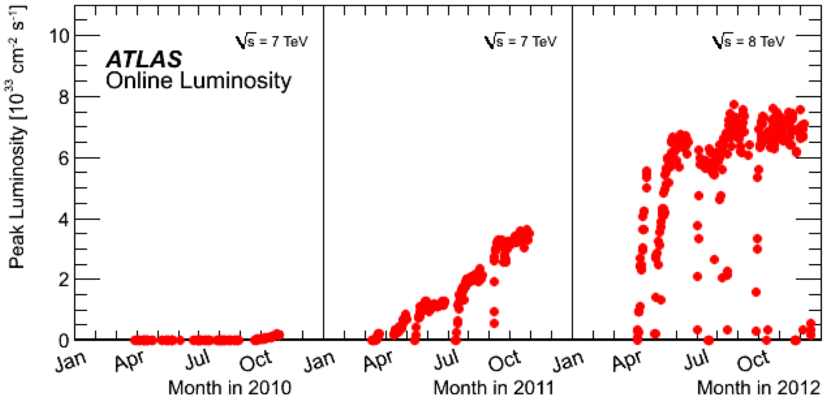

FIGURE 18. Peak instantaneous luminosity delivered to the ATLAS experiment per day in 2010, 2011 and 2012, during 7 TeV and 8 TeV *pp* collisions.

3.1.2. LHC Magnets

The LHC contains thousands of superconducting magnets to move the protons around the 27 km ring. 1232 14.3 meter long dipole magnets steer the proton beams, and 392 5-7 meter long quadrupole magnets focus the beams. The magnets have two apertures, one for each of the counter-rotating proton beams.

3.1.3. Pileup

One of the biggest challenges for data-taking at a proton accelerator is the number of interactions per bunch crossing. This quantity, known as “pileup”, is shown in Figure 19 for the LHC in 2011 and 2012. At the LHC in 2012, the average number of interactions per bunch crossing was 20.7. It is then necessary to separate the tracks and energy deposited in the detector by the hard-scatter event from the other collisions that happened at nearly the same time.

The difficulty of separating one event from another in a high-pileup environment can be seen in Figure 20. This event, captured in 2012, is a $Z \rightarrow \mu^+\mu^-$ event with 20 associated pileup vertices.

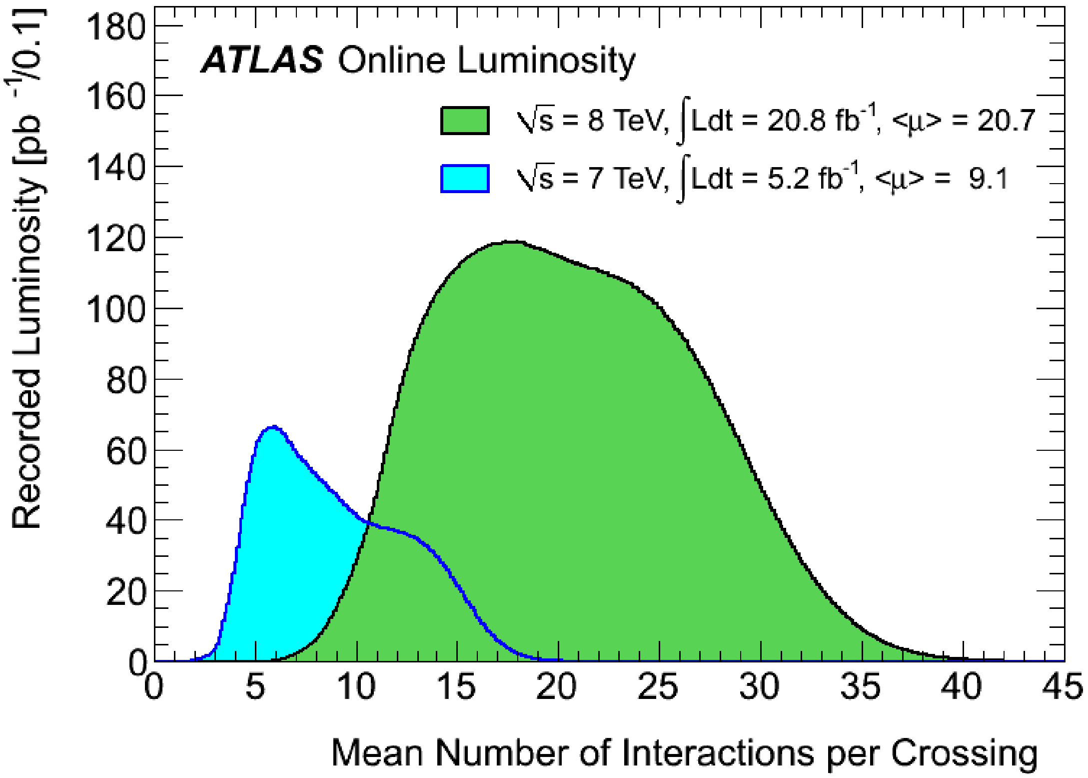

FIGURE 19. Luminosity-weighted distribution of the mean number of interactions per crossing in 2011 and 2012.

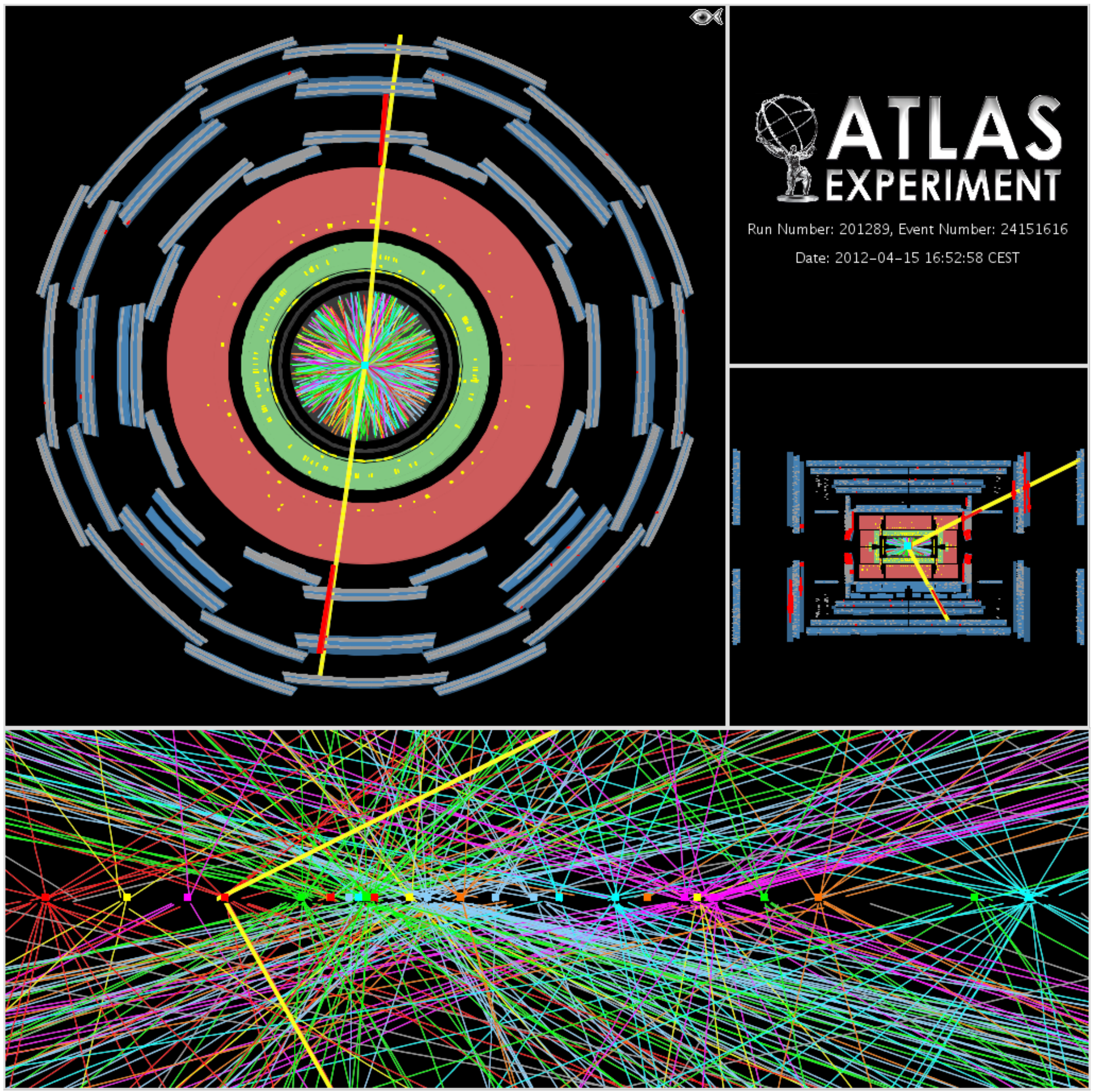

FIGURE 20. $Z \to \mu^+\mu^-$ event with 20 pileup vertices.

3.2. The ATLAS Detector

The ATLAS detector is a general-purpose detector located near the main CERN site at the Large Hadron Collider. A computer-generated image of the ATLAS detector is shown in Figure 21. It is the largest collider detector ever built, at 46 meters long and 23 meters in diameter. It weighs 7000 tons.

The ATLAS detector [37] at the LHC covers nearly the entire solid angle around the collision point. It is comprised of many detector subsystems, each of which is optimized for a different particle signature. From the inner-most part of the detector to the outside, there is an inner detector, which measures the tracks of charged particles, a solenoid, which provides an axial magnetic field, a calorimeter, which measures the energy deposited by electromagnetic particles and charged or neutral hadrons, and a muon system with toroids.

In this search, the final-state particles include an electron or a muon, a photon, jets, and missing transverse energy ($E_{\mathrm{T}}^{\mathrm{miss}}$). Therefore, every subsystem in ATLAS is used to identify one or more of the objects in this search. The subsystems used to identify each species of particle are summarized in Table 7, and illustrated in Figure 22.

TABLE 7. Particles identified by each detector system

Particle	Detector Subsystem	Quantity Measured
Electron	Inner Detector	Track
	Electromagnetic Calorimeter	Energy
Photon	Electromagnetic Calorimeter	Energy
Jets + $E_{\mathrm{T}}^{\mathrm{miss}}$	Inner Detector	Tracks
	Calorimeters	Energy
Muon	Inner Detector	Track
	Muon Spectrometer	Momentum

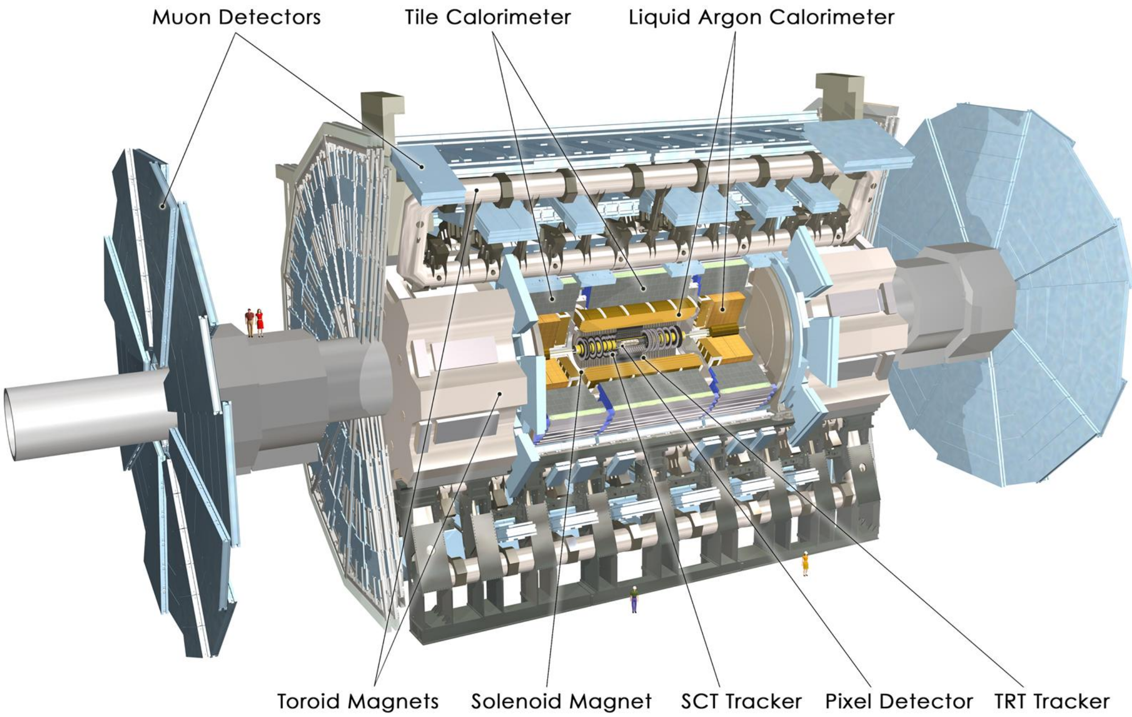

FIGURE 21. The ATLAS detector [38]

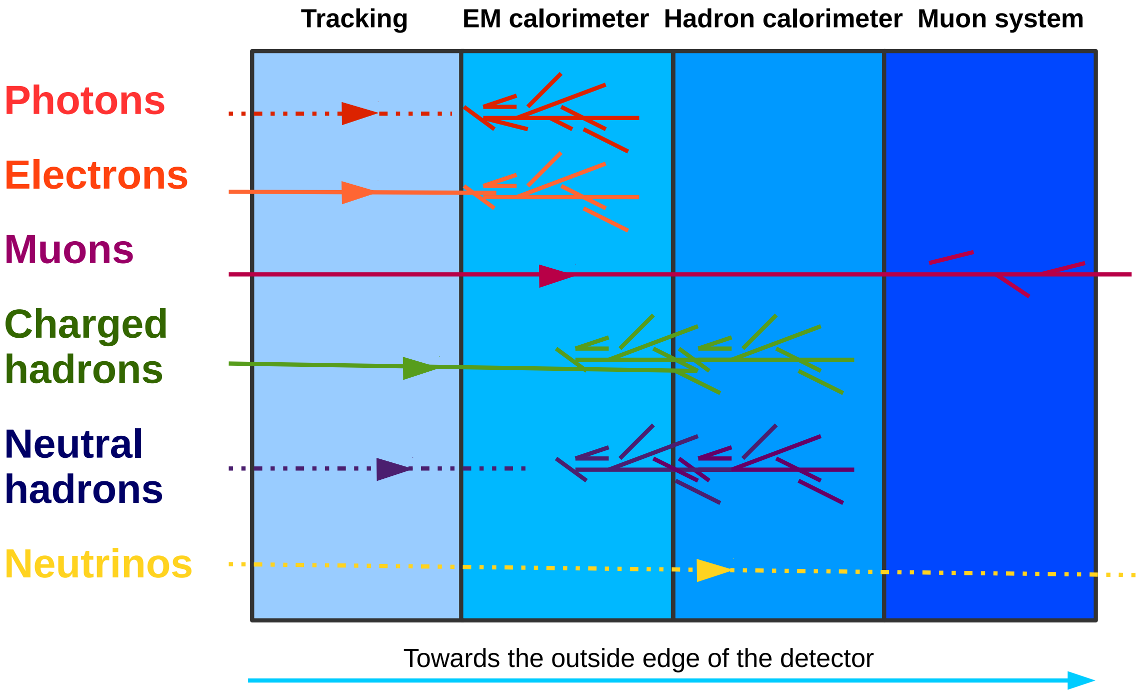

FIGURE 22. A cartoon of a cross-section of the ATLAS detector, and particle identification in each detector subsystem

3.2.1. Coordinate System and Common Variables

ATLAS uses a right-handed coordinate system [37] with its origin at the nominal interaction point (IP) in the center of the detector and the z-axis along the beam pipe, as shown in Figure 23. The x-axis points from the IP to the center of the LHC ring, and the y-axis points upwards. Cylindrical coordinates (r, ϕ) are used in the transverse plane, ϕ being the azimuthal angle around the z-axis. The pseudorapidity η is defined in terms of the polar angle θ as $\eta = -\ln\tan(\theta/2)$. Angular distance is measured in units of $\Delta R \equiv \sqrt{(\Delta\eta)^2 + (\Delta\phi)^2}$.

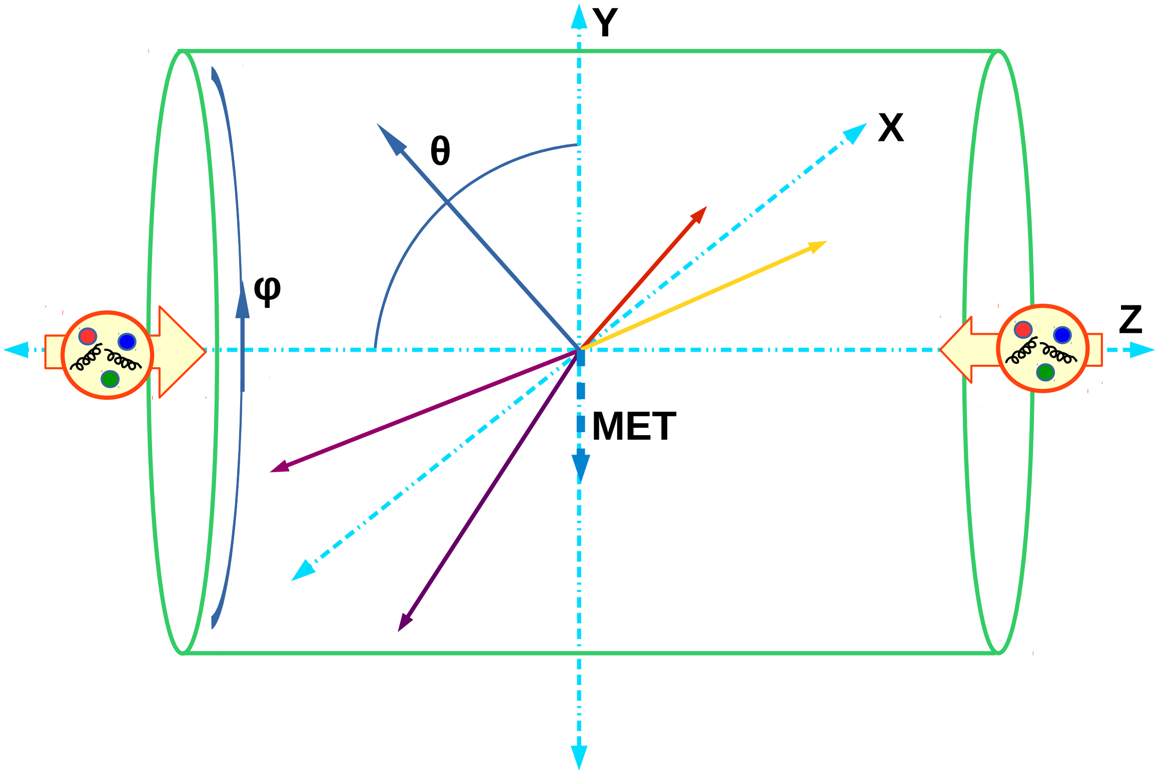

FIGURE 23. The ATLAS coordinate system is shown, detailing the right-handed xyz coordinates, and the variables Θ and ϕ. The missing transverse energy ($E_{\mathrm{T}}^{\mathrm{miss}}$) is represented here by the dotted dark blue line, resulting from the negative vector sum of the particles in this event, which are represented by the colored arrows.

3.2.2. Inner Detector

The inner detector system (ID) is used to reconstruct tracks of charged particles, as they bend in a magnetic field. The inner detector is shown in Figure 24. It is contained in a 2 T axial magnetic field and provides tracking in the range $|\eta| < 2.5$.

The silicon pixel detector covers the vertex region, and provides detailed information about particle tracks and vertex location. Charged particles passing through the pixel detector create current in the silicon detector elements. There are three layers in the pixel detector, and thus typically three hits per track, each of which contribute to the track fit the (x, y, z) position of the hit. The silicon microstrip tracker (SCT) provides up to four additional two-dimensional measurement points per track.

The transition radiation tracker (TRT) complements the silicon detectors, and enables radially extended track reconstruction up to $|\eta| = 2.0$, using 73 straw planes in the barrel, and 160 in the endcap. Charges from gas ionizations are passed down these wires, which provide (x, y) location and z from timing data. Electron identification information can be gathered from the fraction of hits (typically 30 in total) above a higher energy deposit threshold corresponding to transition radiation.

The reconstructed tracks from hits in the inner detector can then be extrapolated back to primary and secondary vertices. The primary vertex corresponds to the hard-scatter *pp* interaction, and secondary vertices arise from decays of long-lived hadrons (B mesons, for example). The primary vertex is chosen to be the one with maximum Σp_{T}^2. Other vertices can occur, due to pile-up.

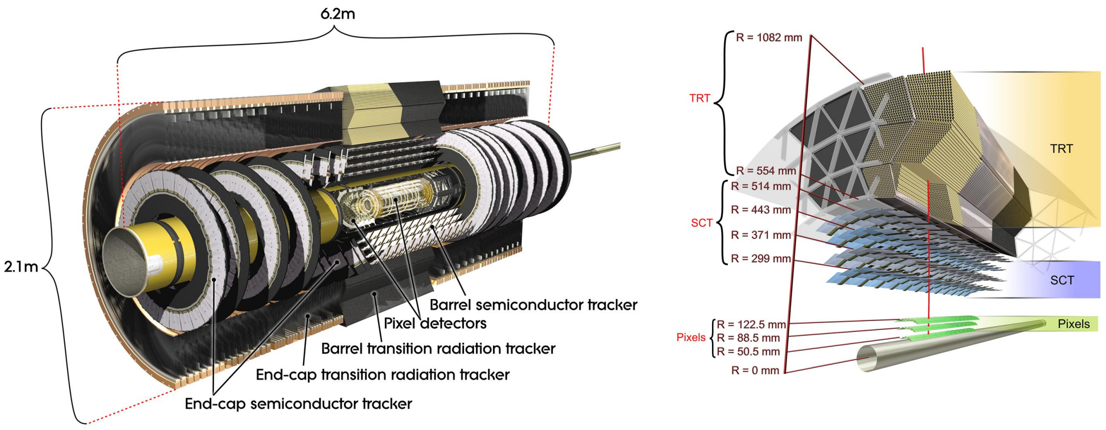

FIGURE 24. The ATLAS inner detector [39]

During Long Shutdown 1 in 2013 and 2014, an additional fourth layer was added to the inner detector. The Insertable B-Layer (IBL) is a high-granularity silicon pixel detector, which consists of 14 staves arranged around the beam pipe to ensure full azimuthal coverage. The average distance of the staves from the beam is 33.25 mm. The silicon pixel size is just 50 x 250 µm. The addition of this new layer to the inner detector necessitated a new, smaller beam pipe, only 25 mm from the beam.

3.2.3. Calorimeters

The ATLAS calorimeter system, shown in Figure 25, is designed to absorb and measure the energy of neutral and charged particles. The signal is created by energy deposited in the calorimeter, so it is important that the energy is completely absorbed before the particle can pass through the back of the calorimeter. This is a sampling calorimeter– it uses dense material for absorption power, combined with active material to measure signal, which is generated from ionizations in the active material. The active material in the electromagnetic calorimeter is liquid argon. This method has limitations: it only directly measures a few tens of percent

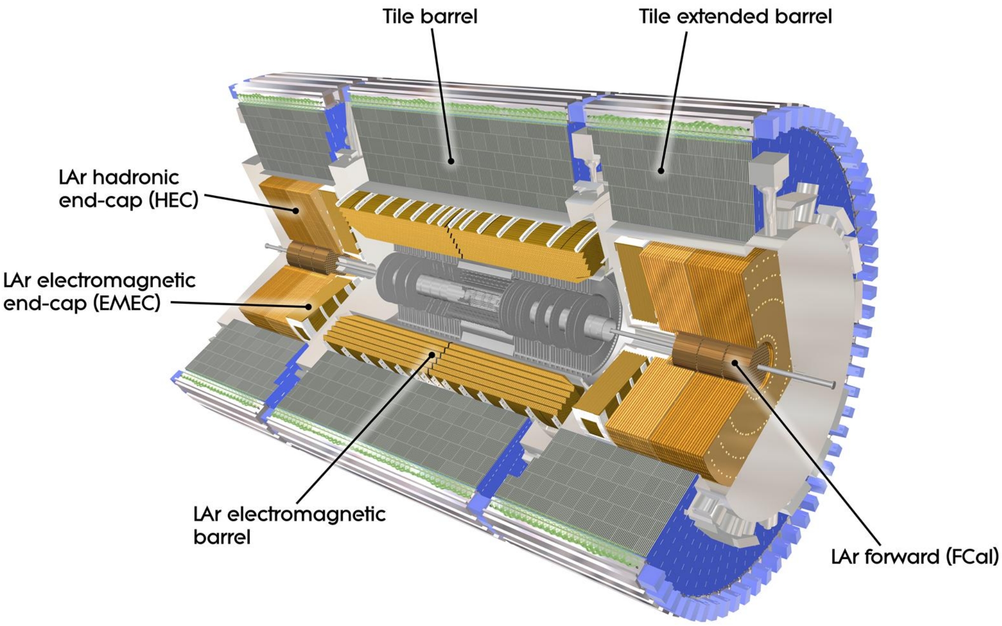

FIGURE 25. The ATLAS calorimeter [40]

of the signal, and so is subject to sampling statistics. Also, hadrons generate less signal than electrons depositing the same energy in a sampling calorimeter. For a sampling calorimter, one wants to know the ratio $\frac{E_{visible}}{E_{deposited}}$ – therefore, one needs to know about multiple scattering in inactive material (since particles can take several paths through the material), which changes the sampling fraction. One has to measure this ratio in test beams where the original beam energy is known very precisely.

The ATLAS calorimeter system covers the pseudorapidity range $|\eta| < 4.9$. Within the region $|\eta| < 3.2$, electromagnetic calorimetry is provided by barrel and endcap high-granularity lead/liquid-argon (LAr) electromagnetic calorimeters, with an additional thin LAr presampler covering $|\eta| < 1.8$, to correct for energy loss in material upstream of the calorimeters. The electromagnetic calorimeter covers 26-35 radiation lengths, depending on exactly where the particle ends up in the

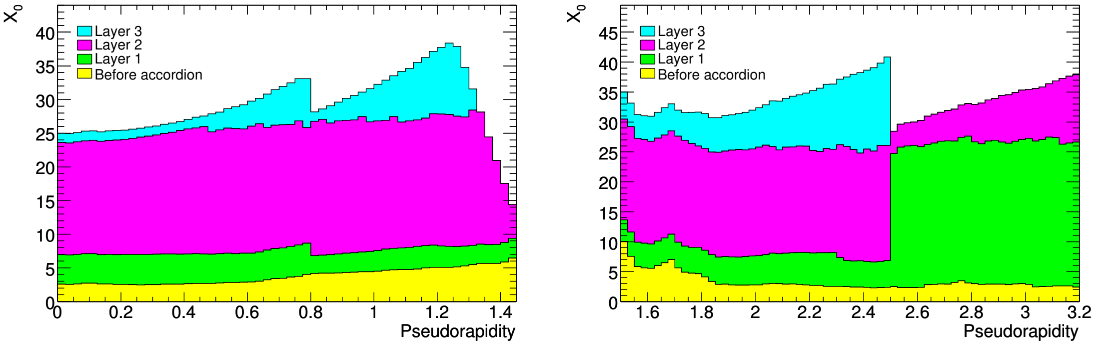

FIGURE 26. The material in each layer of the Electromagnetic Calorimeter, in radiation lengths, as a function of $|\eta|$. [32]

detector. The "accordion" geometry of the LAr calorimeter, shown in Figure 25, provides full azimuthal coverage.

Since the measurement of energy in a sampling calorimeter depends on the amount of material traversed by each particle, it is important to understand not only the detector material, but also the support structures and cables used for data transport, etc. The material in each layer of the electromagnetic calorimeter is shown in Figure 26.

Hadron calorimetry is provided by the steel/scintillating-tile calorimeter, segmented into three barrel structures within $|\eta| < 1.7$, and two copper/LAr hadron endcap calorimeters. The hadron calorimeter extends to 10 interaction lengths. The material in each layer of the hadron calorimeter is shown in Figure 27.

The solid angle coverage is completed with forward copper/LAr and tungsten/LAr calorimeter modules optimized for electromagnetic and hadronic measurements respectively. Although the calorimeter provides nearly 4π coverage around the interaction point, its complex geometry means that there are some "cracks", particularly in the region between the barrel and the endcap. However, there is nearly hermetic coverage in the azimuthal angle ϕ.

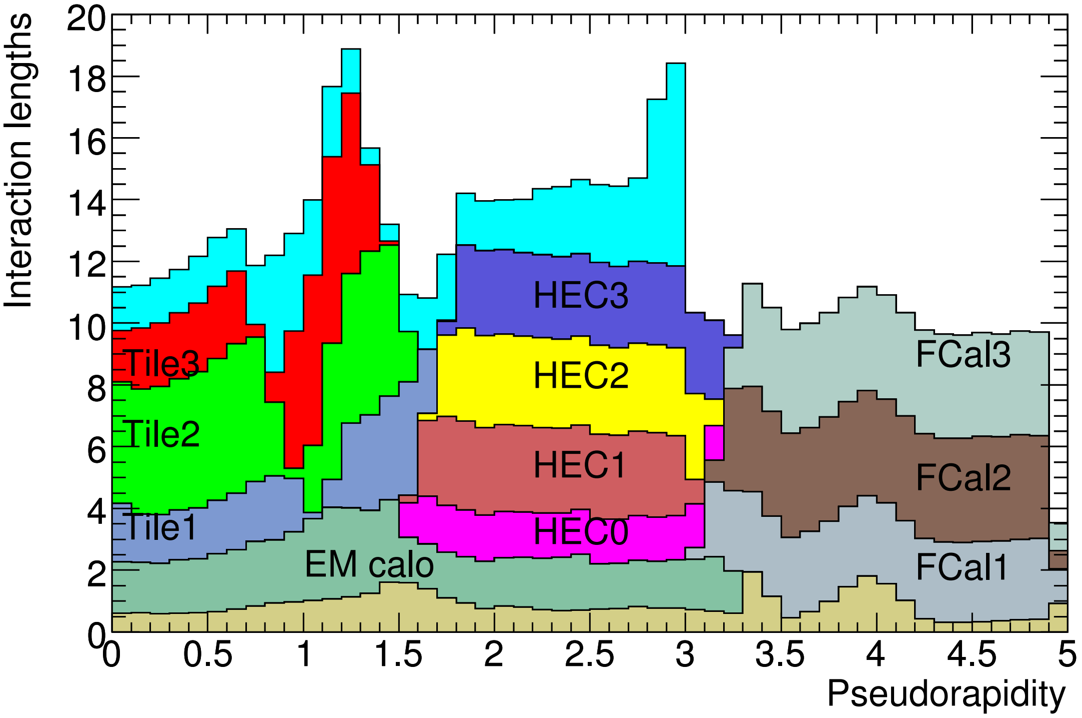

FIGURE 27. The material in each layer of the Hadronic Calorimeter, in interaction lengths, as a function of $|\eta|$. [32]

3.2.4. Solenoid Magnet

The ATLAS superconducting solenoid is aligned with the beam axis, and surrounds the inner detector. It provides a 2T magnetic field, which makes tracking of charged particles possible.

3.2.5. Muon System

The outermost layer of the ATLAS detector is used to measure the momentum of muons, and constists of a separate trigger system and high-precision tracking chambers which measure the deflection of muons in a magnetic field generated by superconducting air-core toroids. The precision chamber in the barrel region, $|\eta| < 2.7$, has three layers of Monitored Drift Tubes (MDTs) for tracking, and Resistive Plate Chambers (RPCs) for triggering. This is complemented by three layers of Cathode Strip Chambers (CSCs) for tracking and Thin Gap Chambers (TGCs) for triggering in the endcap region, where the backgrounds are highest. The various parts of the muon system are shown in Figure 28. Muons will typically hit three layers of the muon system in either the barrel or endcap.

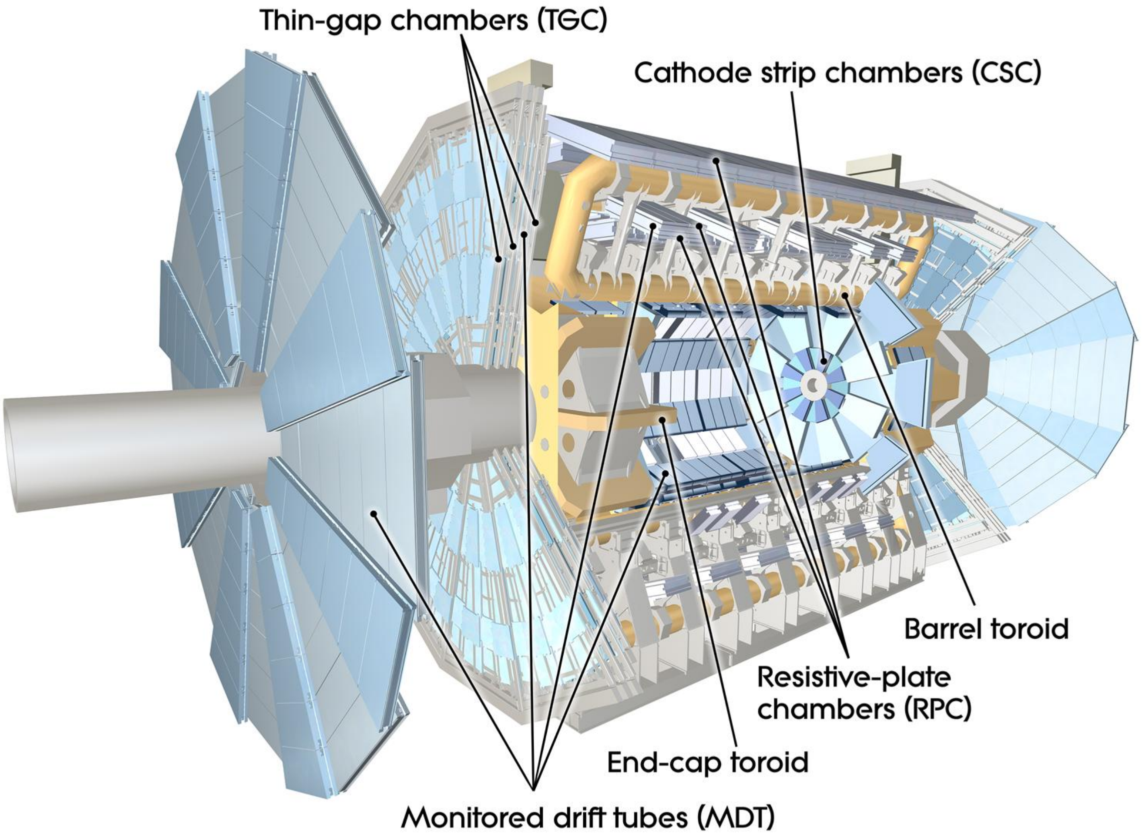

FIGURE 28. The ATLAS muon system [41]

3.2.6. Toroid Magnets

The ATLAS toroid system provides 0.5T and 1T magnetic fields to the barrel and endcap regions, respectively. The barrel toroid has eight-fold symmetry, and consists of eight superconducting air-core toroid coils. The two end-cap toroids also consist of eight coils, which are interleaved with the barrel coils. A magnetic field is provided in the range $|\eta| < 1.4$ by the barrel toroids, and in the range $1.6 < |\eta| < 2.7$ by the endcap toroids. The remaining region is covered by a combination of the barrel and endcap toroids. The goal is to have the muon trajectory be orthogonal to the magnetic field in all areas.

3.2.7. Trigger and Data Acquisition

The ATLAS trigger system selects interesting collisions out of the mountain of data provided by the LHC. The proton bunch crossing rate was 40 MHz in 2012, and we were only able to read out data at a few hundred Hz, so this is a reduction of 5 orders of magnitude. In order to accomplish this reduction, while making sure to keep the best events, ATLAS uses a multi-step hardware and software trigger.

A three-level trigger system is used to select interesting events [42]. The Level 1 (L1) trigger is implemented in hardware and uses a subset of detector information to reduce the event rate to a design value of at most 75 kHz. This is followed by two software-based trigger levels, collectively known as the High-Level Trigger (HLT) which together reduce the event rate to about 200 Hz.

3.2.7.1. Level 1 Trigger

The Level 1 hardware trigger uses coarse information from some of the subdetectors to make fast initial trigger decisions. The L1 trigger uses information from the RPCs and TGCs for muons, and from all of the calorimeter systems for electrons, hadrons, photons, jets, and missing transverse energy. The decision time for the L1 trigger is 25 μs. The L1 trigger identifies one or more regions of interest (RoI), defined in η and ϕ, which are then passed to the HLT.

3.2.7.2. High Level Trigger

The Level 2 (L2) trigger uses the information from the RoIs received from L1, as well as the full detector granularity to make a decision. Finally, the Event Filter (EF) has an additional 4 seconds to make a decision, and can make more detailed selections, such as b-tagging or vertex position.

3.2.7.3. Trigger Menu During Run 1

The trigger system can be configured during data-taking by making changes to what is known as the trigger menu. The trigger menu consists of a set of trigger chains, which are made up of trigger decisions at each of the three trigger levels, L1, L2, and EF. The trigger menu is divided among a variety of trigger signatures, which correspond to the physics objects being selected: electrons, muons, photons, jets, MET, b-tagged jets, and hadronically decaying taus. In order to keep the entire trigger within the available bandwidth (a few hundred events per second), the trigger chains can be pre-scaled. Pre-scaled trigger chains will only select a fraction of the events which pass their selection. Pre-scales can be dynamically adjusted during data-taking as the instantaneous luminosity decreases. In this way, the maximum number of interesting events are always being recorded.

3.2.8. Data Quality

Not all data recorded by the ATLAS detector can be used for analysis. Detailed records are kept for each detector subsystem, with information on detector performance.

3.2.9. Luminosity Measurement - Forward Detectors

Two detector subsystems are used to determine the luminosity delivered to the ATLAS experiment: LUCID and ALFA. Both detectors are located around the beampipe, forward and backward of the ATLAS detector. LUCID (LUminosity measurement using a Cherenkov Integrating Detector) is located at ± 17 m from the interaction point, and consists of 20 1.5 m-long gas-filled tubes with photomultiplier tubes at the ends used to measure the relative luminosity bunch-by-bunch, as well as diffractive physics. The ALFA (Absolute Luminosity for ATLAS) sub-detector is located at ± 240 m from the interaction point, and is used to measure the total luminosity delivered to the ATLAS experiment. ALFA consists of eight scintillating fiber detectors inside roman pots, located above and below the beampipe. ALFA takes measurements during dedicated LHC runs, called vDM scans. An additional measurement of the luminosity is provided by the Zero-Degree Calorimeter (ZDC), located at ± 140 m from the interaction point.

CHAPTER IV

SIMULATION AND RECONSTRUCTION

This chapter describes the simulation of physics processes and the reconstruction of physics objects from recorded data and from simulation.

4.1. Simulation of pp Collisions

The ATLAS experiment uses Monte Carlo (MC) simulations to make predictions and to compare data to theoretical models. Simulations of Standard Model processes can be used as validation, to check that object reconstruction is working correctly. Simulations of new physics are used to predict what will be seen if a particular theory turns out to be true. A flow chart showing the process of simulation is shown in Figure 29.

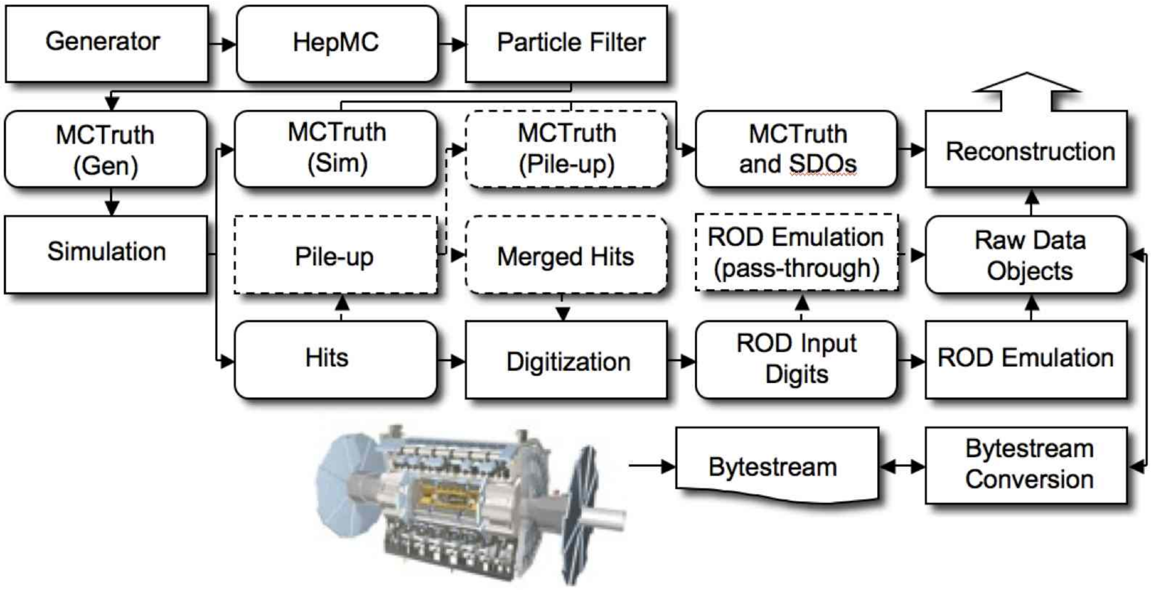

FIGURE 29. Flow chart which shows the process of ATLAS simulation, from event generation (top left) to reconstruction (top right). SDO = “Simulated Data Object”, ROD = “Read Out Driver” [43]

4.1.1. Monte Carlo Generators

Different generators specialize in simulating different physics processes. Monte Carlo generators can also be classified by the precision of their calculations (leading-order (LO) vs. next-to-leading-order (NLO), etc.). The Monte Carlo generators used in this search are summarized below.

ALPGEN*:* Alpgen is a leading-order generator for hard processes. It specializes in processes with high multiplicity final states [44]

HERWIG*:* Herwig is a general-purpose leading-order generator [45]

MADGRAPH*:* MadGraph is a leading-order generator for hard processes [46]

POWHEG*:* Powheg is a next-to-leading-order generator that can be interfaced with other generators (PYTHIA, for example) for showering [47, 48]

PROTOS*:* Protos is a specialized generator for anomalous top couplings [49, 50]

PYTHIA*:* Pythia can generate hard processes as well as perform showering. It is commonly interfaced to other generators [51]

SHERPA*:* Sherpa is a leading order generator [52, 53, 54, 55, 56]

In order to take advantage of powerful and well-validated generators of Standard Model processes, such as HERWIG and PYTHIA, a common input file format was designed in the Les Houches Accords [57]. This allows users to generate the hard process with a specialized generator, such as PROTOS, and then simulate the rest of the event (the parton showers, underlying event, hadronization, and ordinary decays) with HERWIG or PYTHIA.

4.2. Detector Simulation

In order to compare the simulated physics processes with data collected with the ATLAS detector, it is necessary to model the response of the detector [43] as particles move through it.

The interaction of particles with the detector materials is modeled in GEANT4 [58].

4.3. Object Reconstruction

This section describes the physics object selection and reconstruction. Events selected for this search include one lepton, one photon, at least two jets (exactly one of which is b-tagged), and missing transverse energy (which corresponds to a neutrino). Each species of particle leaves a unique signature in the ATLAS detector, as shown in Figure 30.

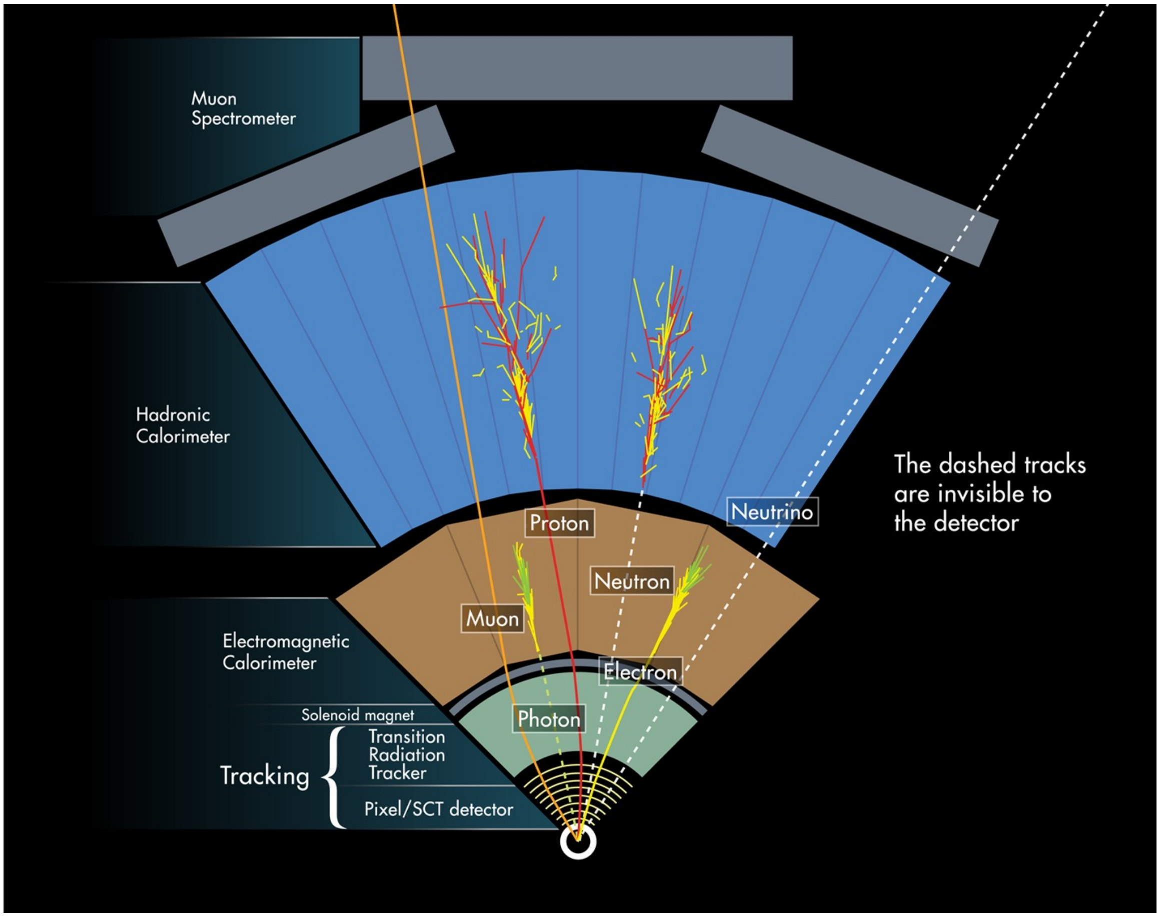

FIGURE 30. Particle identification with the ATLAS detector [59]

4.3.1. Electrons

When electrons interact with matter in the detector, showers form entirely by QED processes (bremsstrahlung and photon pair production). The process through which electrons form a shower in the detector, known as "cascade development", is a very regular process. Showers always look the same, and their longitudinal and lateral development are very correlated. It is possible simulate these showers with high precision.

Electron candidates are reconstructed from energy clusters in the electromagnetic calorimeter, which are then associated with charged tracks from the inner detector, as described in [60]. Electrons are required to have transverse energy, E_{T}, greater than 25 GeV, and $0 < |\eta_{cluster}| < 2.47$, with the crack region ($1.37 < |\eta_{cluster}| < 1.52$) excluded. `tight++` identification [61] for the cluster and track is used for electron candidates, following the specifications provided by the Egamma Combined Performance group. To separate electron candidates from QCD multi-jet background, cuts are placed on two isolation variables: the energy deposited in a cone of $\Delta R < 0.2$ around the electron candidate, and the transverse momentum of all the tracks within a cone of $\Delta R < 0.3$ around the electron candidate. The value of each cut is chosen to have 90% selection efficiency in simulation. Finally, the longitudinal impact parameter of the electron track with respect to the identified primary vertex of the event, z_0, is required to be less than 2 mm. Figure 31 shows an electron candidate in the xy-plane of the ATLAS detector, next to a muon candidate and a jet. Jets within $\Delta R < 0.2$ of an electron candidate are removed from the event. If another jet (with $p_{\mathrm{T}} > 25$ GeV and $|JVF| > 0.5$) is found within $\Delta R <0.4$ of the electron candidate, then the electron is removed.

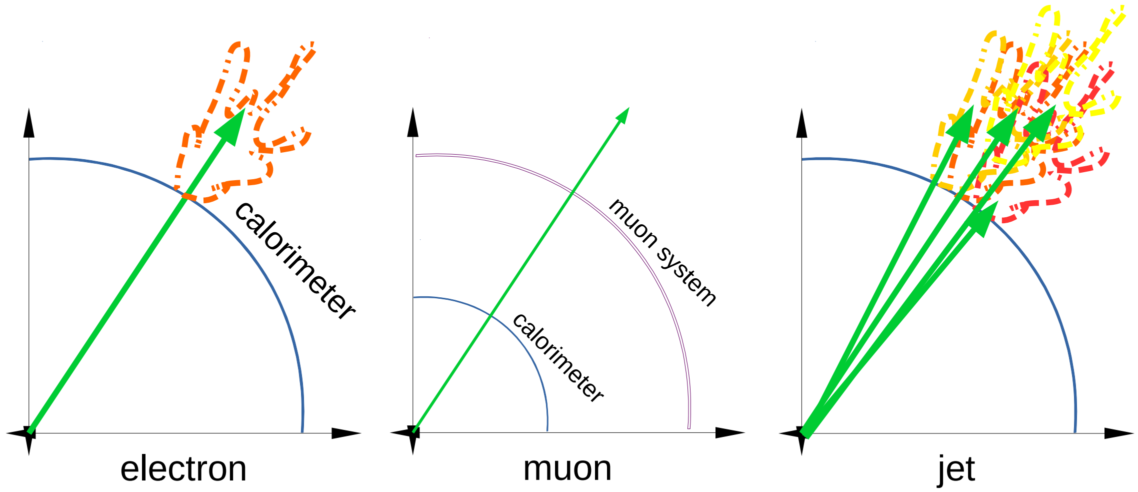

FIGURE 31. Discriminating leptons from jets in the detector

4.3.2. Jets

In contrast with the simple shower development from electrons, jets form showers through QCD processes. These are much harder to simulate well. The showers are also larger– so we need larger detectors to see the entire jet. There are many different jet-finding algorithms available. Some are better than others (and there the best choice of algorithm might depend on the final state that you are trying to model). The goal of jet-finding is to bring together all the final-state particles that originate from the same source and re-establish the original connections between particles coming from the same source.

In this search, jets are reconstructed with the anti-k_T algorithm [62] with a radius parameter R = 0.4, starting from energy clusters in the calorimeter reconstructed using the energy scale established for electromagnetic objects. The anti-k_T is preferred to naive seeded cone jet algorithms, because it is infrared and collinear safe. (Infrared safety implies that two jets should not be merged by a soft emission between them, that is, adding or removing a soft term should not change the jet finding results. Collinear safety means that the splitting of a high-p_T object should not affect the jet finding.) Selected jets have $p_\mathrm{T} > 25$ GeV, and $|\eta| < 2.5$. To reduce selected jets that originate from pileup interactions, a requirement on the jet vertex fraction (JVF) is made. The requirement ensures that at least 50% of the tracks associated with a jet with $p_\mathrm{T} > 50$ GeVand $|\eta| < 2.4$ are compatible with originating from the primary vertex.

4.3.2.1. b-tagging

Jets that originate from bottom quarks can be identified separately from light-flavor jets, since the lifetime of bottom quarks ($\approx 10^{-12}$s) is so much longer than that of light quarks. Due to this long lifetime, jets that originate from bottom quarks are displaced compared to the primary vertex, as can be seen in Figure 32. A multivariate algorithm (MV1 tagger) is used to select jets that are most compatible with the hadronization of a bottom quark. The b-tagging weights used as a cut in this search were determined from $t\bar{t}$ Monte Carlo samples to result in a 70% selection efficiency for jets with $p_\mathrm{T} > 20$ GeV, and $|\eta| < 2.4$.

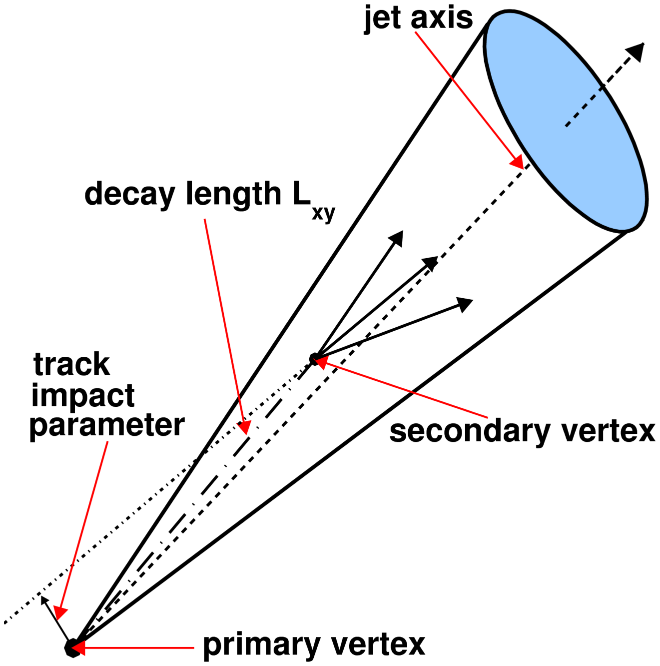

FIGURE 32. B-tagging variables [63]

4.3.3. Missing Transverse Energy

The missing transverse energy ($E_{\mathrm{T}}^{\mathrm{miss}}$) is calculated from the energy deposited in all electromagnetic and hadronic calorimeter cells in $|\eta| < 4.5$ range and from momenta of muon tracks reconstructed with $|\eta| < 2.7$, as described in [64].

4.3.4. Photons

Photon candidates are reconstructed from energy clusters in the electromagnetic calorimeter. Candidates are required to have $p_{\mathrm{T}} > 15$ GeV,

$0 < |\eta_{cluster}| < 2.37$ (excluding the crack region $1.37 < |\eta(cluster)| < 1.52$), and to meet the `tight` identification [65], as defined by the Egamma Combined Performance Group. The `tight` selection includes requirements on the total transverse energy deposited in the hadronic calorimeter (to reject neutral hadrons) and the shower shape in the strip and middle layers of the electromagnetic calorimeter (to reject neutral pion decays). The `tight` photon requirements are listed in Table 8.

Jets are removed from the event if they are within $\Delta R(\gamma,\mathrm{jet}) < 0.1$ of a selected photon. Figure 33 shows a photon candidate in the xy plane of the ATLAS detector, next to an electron, a neutral hadron decaying to a pair of photons, and a jet. Further photon selection is then implemented with isolation variables p_{T} cone20 and topoE_{T} cone40. p_{T} cone20 is a measure of the scalar sum of the track p_{T} in a cone of $\Delta R < 0.2$ around the photon candidate and topoE_{T} cone40 is the sum of E_{T} of clusters within $\Delta R < 0.4$ of the photon candidate.

TABLE 8. Photon identification variables

Variable	Description
w_{s3}	Shower width for in the EM strip layer for the three strips around the shower maximum
w_{stot}	Total shower width in the EM strip layer
F_{side}	Energy in three central strips / energy outside of three central strips but within seven
ΔE	Energy difference between the second shower maximum in the EM strip layer and the shower minimum between the 1st and 2nd maxima
E_{ratio}	Ratio of the first and second shower maxima over their energy sum
$w_{\eta 2}$	Shower width in the EM middle layer
R_{had_1}	Ratio of E_{T} in the first sampling of the hadronic calorimeter to E_{T} of the EM cluster
R_{had}	Ratio of E_{T} in all of the hadronic calorimeter to E_{T} of the EM cluster

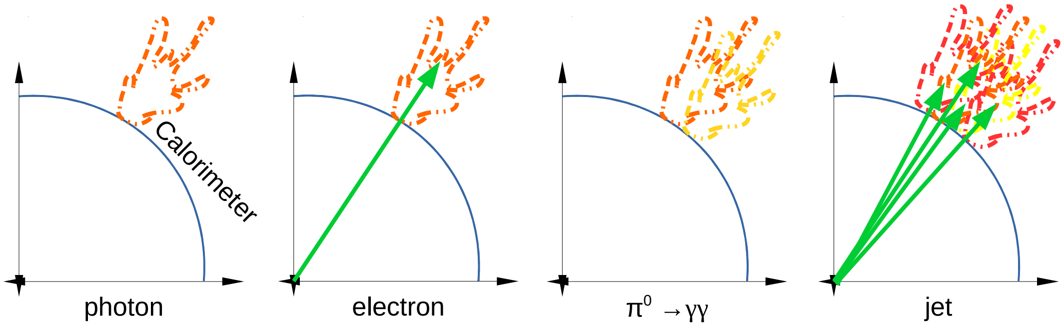

FIGURE 33. Discriminating photons from other objects in the detector

4.3.5. Muons

Muon candidates are selected by matching track segments from the muon chambers with tracks from the inner detector, as described in [66]. Candidates are required to have $p_{\mathrm{T}} > 25$ GeV and $|\eta_{track}| < 2.5$. Cosmic muons are rejected by requiring the longitudinal impact parameter of the track with respect to the selected primary vertex of the event, z_0, is less than 2 mm. Muon candidates are also required to pass the mini isolation requirement, MiniIso10_4/$p_{\mathrm{T}}^{muon} < 0.05$, as defined in [67]. Jets within $\Delta R < 0.2$ of a muon candidate are removed from the event. The muon candidate is required to be separated from selected jets (with p_{T} > 25 GeV and $|JVF| > 0.5$) by $\Delta R >$0.4 . Figure 31 shows a muon candidate in the xy-plane of the ATLAS detector, next to an electron candidate and a jet.

CHAPTER V

THE SEARCH FOR FCNC IN $t\bar{t}$ EVENTS

This chapter describes the search for the flavor-changing neutral current in $t\bar{t}$ events, where on top decays to a W boson and a bottom quark, and the other decays to a light quark (up or charm) and a photon: $t\bar{t} \rightarrow W\mathrm{bq}\gamma$.

5.1. Data and Simulation

The data used in this search were recorded in 2012 pp collisions at $\sqrt{s} =$ 8 TeV. Monte Carlo simulation samples are used to estimate backgrounds from Standard Model processes, as well as predict features of signal events.

5.1.1. 2012 ATLAS Data

This dissertation contains an search of the entire 2012 ATLAS dataset, collected between April and December 2012. The events analyzed are required to pass data quality requirements for physics in the standard "All Good" Good Runs List (GRL), which corresponds to 20.3 fb^{-1}. Single lepton (electron or muon) triggers are used to select events for this search. In both the Egamma (electrons and photons) and Muon data streams, a logical OR of the two lowest un-prescaled triggers which were available for the entire year are used.

Selected events in the Egamma stream must have fired either the `EF_e24vhi_medium1` or `EF_e60_medium1` triggers, which differ in p_{T} threshold and isolation requirement. `EF_e24vhi_medium1` requires a loose isolation cut, ptcone20/E$_T$ < 0.1. The electron trigger efficiency curves [68] are shown in Figure 34.

Selected events in the muon stream are required to pass `EF_mu24i_tight` or `EF_mu36_tight`. The isolation requirement in `EF_mu24i_tight` is ptcone20/$p_{\mathrm{T}} < 0.12$. Efficiency curves [69] for the `EF_mu24i_tight` and `EF_mu36_tight` triggers are shown in Figure 35.

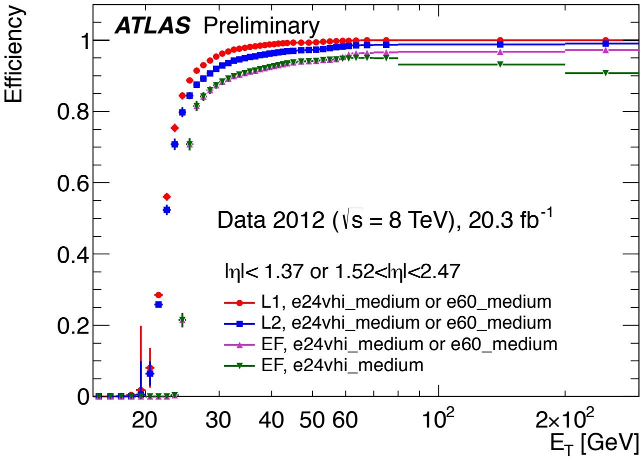

FIGURE 34. Efficiency curves for a logical OR of the electron triggers used in this search, `EF_e24vhi_medium1` and `EF_e60_medium1`

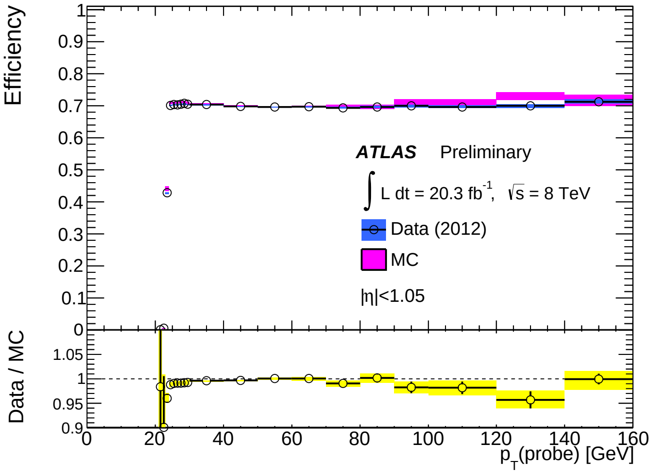

FIGURE 35. Efficiency curves for the logical OR of the muon triggers used in this search, `EF_mu24i_tight` and `EF_mu36_tight`

5.1.2. Monte Carlo Generators

Monte Carlo (MC) processes are used to simulate the signal and background events studied in this search. This section summarizes the generators used.

The signal Monte Carlo sample of 100,000 full simulation $t\bar{t}$ events, where $t\bar{t} \rightarrow W$bqγ (q=u,c) and the W boson decays leptonically, was produced using Protos 2.2 [49, 50] + Pythia 6.426 [51], with CTEQ6L1 PDF set [70] and 2011C tune.

5.1.2.1. Background Samples

There exist a large number of other Standard Model processes that result in the same final state topology as the signal process $t\bar{t} \rightarrow b\ell\nu q\gamma$. Those processes are also modeled with Monte Carlo (MC) simulation (with the exception of fake leptons and photons, which are not modeled well in MC, and therefore are estimated using data-driven methods that will be discussed later.) The nominal MC samples used in this search are listed in Table 9.

Non-all-hadronic Standard Model $t\bar{t}$ production is modeled with Powheg [47, 48] and Pythia 6.427 [51], with PDF set CT10 [71] and P2011C tune. The h_{damp} parameter is set to the top mass [72]. (The h_{damp} parameter in Powheg is used to regulate matrix element and parton shower matching, and regulates the high-p_{T} radiation. It is normally set to infinity, but better data- Monte Carlo agreement for observables such as $t\bar{t}$ p_{T} was seen when h_{damp} was set to the top mass.) This is a full-simulation sample. The top cross-section is calculated to be $\sigma_t = 252.9\ ^{+6.4}_{-8.6}$ (scale) ± 11.7 (PDF + α_S) pb using the Top++2.0 program to next-to-next-to-leading order in perturbative QCD, assuming m$_{top}$ = 172.5 GeV[73]. The uncertainties come from varying the factorization and normalization

TABLE 9. Signal and background MC samples used in this search. More details can be found in Appendix B

Process	Generator
FCNC $t\bar{t}$	Protos + Pythia
SM $t\bar{t}$	Powheg + Pythia
$t\bar{t}$ +V+jets	Madgraph + Pythia
W+jets	Alpgen + Pythia
W+heavy flavor+jets	Alpgen + Pythia
Z+jets	Alpgen + Pythia
Z+heavy flavor+jets	Alpgen + Pythia
Diboson	Herwig
Single Top	Powheg + Pythia
Single Top + γ	Sherpa
V+γ +jets	Sherpa
W+γ +jets	Alpgen + Pythia
$t\bar{t}$ + γ	Madgraph + Pythia

scales, and from varying the PDF following the PDF4LHC prescription with the MSTW2008, CT10, and NNPDF2.3 5f FFN PDF sets [74, 75, 76, 77]. More details on the sample can be found in Table 19 (see Appendix B for Tables 18-25).

W+jets and Z+jets backgrounds were simulated with Alpgen [44] and Pythia 6.426 [51] On-The-Fly, with P2011C tune and CTEQ6L1 PDF set, using full simulation. These samples contain up to five extra partons, with light-flavor and heavy-flavor extra jets separated. Overlap between light- and heavy-flavor samples is removed using the Heavy Flavor Overlap Removal (HFOR) tool. The W and Z decay leptonically. More details on these samples can be found in Tables 20, 22, 21, and 23.

Diboson processes WW, WZ, and ZZ are simulated with Herwig 6.520.2 [45], with AUET2 tune and PDF set CTEQ6L1, using fast simulation with `ATLFASTII`. More details on these samples can be found in Table 24.

$t\bar{t}$ + W,Z events with up to two extra partons are simulated with MADGRAPH [46] + PYTHIA 6.426 [51], with AUET2B tune and CTEQ6L1 PDF set, using full simulation. More details on these samples can be found in Table 24.

Standard model processes with an associated photon are also modelled. $t\bar{t}$ + γ events are simulated with MADGRAPH [46] + PYTHIA 6.427 [51], with P2011C tune and CTEQ6L1 PDF set, using full simulation. Photons in the sample have truth $p_{\mathrm{T}} > 10$ GeV. Single top + γ events are modelled with SHERPA 1.4.5 [52, 53, 54, 55, 56], with PDF set CT10, using full simulation. The simulated top quarks decays to a W boson and a bottom quark, and the W boson decays leptonically. W or Z + γ samples are generated with SHERPA 1.4.1 [52, 53, 54, 55, 56], with PDF set CT10, using full simulation. The W and Z bosons decay leptonically. There are up to three extra partons, and the truth photon has $p_{\mathrm{T}} > 8$ GeV. A comparison is made in the W+γ validation region between the SHERPA W+γ samples and ALPGEN + PYTHIA W+γ samples. The ALPGEN + PYTHIA W+γ samples are filtered with lepton $p_{\mathrm{T}} > 18$ GeVand photon $p_{\mathrm{T}} > 8$ GeV, for more statistics. More details on these samples can be found in Table 25.

Overlap removal is applied between samples with and without a real photon. For example, there may be overlap between Standard Model $t\bar{t}$ and $t\bar{t}$ +γ samples. Events are removed from the $t\bar{t}$, W+jets, Z+jets, and single top samples if they are outside of the truth phase space for the sample with photons, and they contain a truth photon which does not originate from a hadron or lepton, as determined by the `MCTruthClassifier` tool.

5.1.3. Background Estimate Summary

The dominant backgrounds in this search are SM $t\bar{t}$, SM $t\bar{t}$ with an associated photon ($t\bar{t}$ +γ), and W+jets with an associated photon (W+γ). Most backgrounds are modeled with Monte Carlo, with some data-driven estimates and corrections. This is a reference list on how different backgrounds are modeled in this search:

SM processes: Standard Model processes $t\bar{t}$, W+jets, Z+jets, single top, diboson, and $t\bar{t}$ +V are modeled with Monte Carlo simulation. Control regions are defined to test the performance of the largest background contributions, $t\bar{t}$ and W+jets. More details are given in Section 5.4.2.

SM processes with an extra photon: Standard Model + extra photon processes $t\bar{t}$ +γ, W+γ, Z+γ and single top + γ are modeled with Monte Carlo simulation. Overlap removal is applied between SM and SM+γ samples. More details are given in Section 5.4.1.

Fake leptons: The number of events with fake leptons is estimated using the matrix method, as in Section 5.4.4.1.

Fake photons: The number of events with fake photons are estimate using $Z \rightarrow e^+e^-$ tag-and-probe ($e \rightarrow \gamma$ fakes, Section 5.4.3) and the ABCD method (jet $\rightarrow \gamma$ fakes, Section 5.4.4.2)

5.2. Event Selection

This search is performed in $t\bar{t}$ candidate events where one top quark decays to a W boson and a bottom quark (and the W boson then decays leptonically– to an electron or muon and associated neutrino, $W \rightarrow \ell\nu$) and the other top quark decays to a light quark and a photon, $t \rightarrow q\gamma$. The selected events are then $t\bar{t} \rightarrow$ Wbqγ

$\rightarrow \ell\nu bj\gamma$. Selected events will contain at least two jets (exactly one of which is b-tagged, using the MV1 tagger), exactly one isolated lepton (an electron or a muon), one high-p_{T} photon, a large amount of missing transverse energy ($E_{\mathrm{T}}^{\mathrm{miss}}$), and large transverse W mass ($m_{\mathrm{T}}^{\mathrm{W}} = \sqrt{2 * p_{T_\ell} * E_{\mathrm{T}}^{\mathrm{miss}} * (1 - cos(\phi_\ell - \phi_{MET}))}$). The transverse W mass requirement selects events with a lepton and $E_{\mathrm{T}}^{\mathrm{miss}}$ which are consistent with a W decay.

5.2.1. Pre-selection

The pre-selection is defined to select events with exactly one good lepton (and electron or muon), at least two jets (at least one of which is b-tagged), missing transverse momentum, and at least one photon. The expected final-state topology for this signal is shown in Figure 36.

- OR lowest un-prescaled isolated and non-isolated triggers
- Require a primary vertex with $\mathrm{N}_{tracks} > 4$
- Exactly one good lepton ($p_{\mathrm{T}} > 25$ GeV)
- Require trigger matching

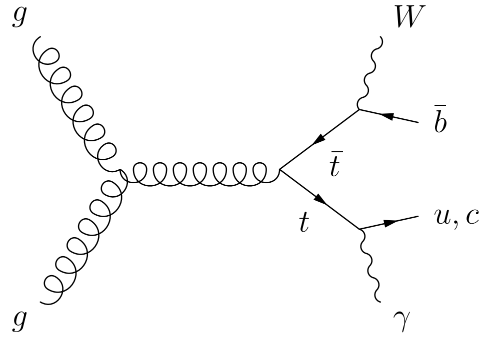

FIGURE 36. A candidate FCNC $t\bar{t}$ event, where one top decays to Wb and the other decays to $q\gamma$

- Overlap removal
- At least two good jets ($p_{\mathrm{T}} > 25$ GeV)
- $E_{\mathrm{T}}^{\mathrm{miss}} > 30$ GeV and $m_{\mathrm{T}}^{\mathrm{W}} > 30$ GeV (electron channel)
- $E_{\mathrm{T}}^{\mathrm{miss}} > 20$ GeV and $E_{\mathrm{T}}^{\mathrm{miss}} + m_{\mathrm{T}}^{\mathrm{W}} > 60$ GeV (muon channel)
- At least one b-tag (MV1 at 70% - at least one good jet has MV1 > 0.7892)
- Exactly one good photon, $p_{\mathrm{T}} > 15$ GeV

5.3. Event Reconstruction

Once the candidate events have been selected, it is necessary to reconstruct the W boson and top quarks from the final state particles. There is only one way to reconstruct these events (no combinatorics!), but there is an ambiguity in the choice of neutrino z-momentum (one can only measure $p_{x\nu}$ and $p_{y\nu}$ with the ATLAS detector). By minimizing $\chi^2 = \frac{(m_{bjet,\ell,\nu} - m_t)^2}{\sigma^2_{SMtop}} + \frac{(m_{\ell,\nu} - m_W)^2}{\sigma^2_W}$, one can find $p_{z\nu}$. Widths σ_{SMtop} and σ_W are determined from signal Monte Carlo (truth information is used for neutrino, reconstructed objects are used for lepton, jets, photon), as shown in Figure 37:

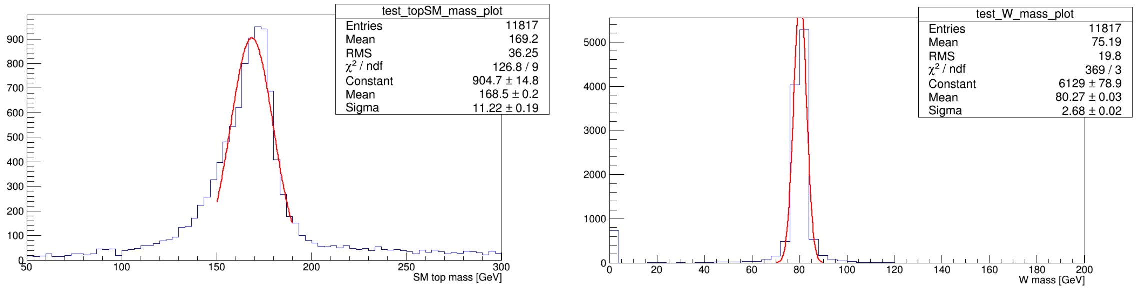

FIGURE 37. Widths for the SM top quark (σ_{SMtop}) and W boson (σ_W) are determined from Monte Carlo: $\sigma_{SMtop} = 11.2$ GeV, $\sigma_W = 2.7$ GeV

Reconstruction of W bosons and top quarks is as follows:

- Vary $p_{z\nu}$ to minimize χ^2

- Finally, reconstruct W and top quarks: W = neutrino + lepton, top_{SM} = Wboson + b-tagged jet, top_{FCNC} = photon + highest-p_{T} light jet

The reconstructed mass m($\ell\nu b$) of the candidate SM top quark, and the reconstructed mass of the candidate FCNC top quark m($q\gamma$) is shown in Figure 45, after signal region pre-selection, for the electron (a) and muon (b) channels.

5.3.1. Final Selection

The final selection adds more cuts on kinematic variables, as well as further refining the signal selection. These cuts are designed to reduce background contributions from Standard Model processes, while retaining the maximum number of signal events. Further constraints are applied to the photon candidate to improve signal purity (background processes enter the signal region when jets or electrons are mis-indentified as photons). The final selection is shown below as a list, and then each cut is described in further detail.

Final photon-related cuts:

- Photon $p_{\mathrm{T}} > 50$ GeV
- $\Delta R(\gamma$, closest jet$) > 0.4$
- $\Delta R(\gamma, \ell) > 0.7$
- Photon isolation:
    - p_{T} cone20 < 3 GeV
    - topoE_{T} cone40 < 4 GeV

The signal photons are very high p_{T}, since they originate from top decays, whereas background photons are typically from soft processes. Therefore, a cut on photon candidates at high p_{T} removes much of the backgrounds, as shown in Figure 38. In order to remove photon contributions from initial- or final-state radiation, events are removed where the photon candidate is too close to another object. If the photon candidate is within ΔR=0.4 of the closest jet, or within ΔR=0.7 of the lepton candidate, the event is removed. Candidate photons are required to be isolated from other objects and from other activity in the detector. Two isolation variables are used: ptcone20, which is the scalar sum of the p_{T} of all of the tracks within ΔR=0.2 of the photon candidate, and topoE_{T} cone40, which the the sum of clusters in the calorimeters within ΔR=0.4 of the photon candidate. Both isolation variables are shown in Figure 39.

Other final cuts:

- EXACTLY one b-tag (Exactly one good jet has MV1 $>$ 0.7892)
- $|m_{e\gamma} - m_Z| > 10$ GeV (electron channel only)
- $m_{e\gamma} > 5$ GeV(electron channel only)
- $E_{\mathrm{T}}^{\mathrm{miss}} + H_{\mathrm{T}} < 350$ GeV, to minimize $t\bar{t}$ and W backgrounds, where $H_{\mathrm{T}} = \Sigma p_{\mathrm{T}}$
- Top mass requirement: $|m_{b\ell\nu} - m_{top}| < 50$ GeV, $|m_{q\gamma} - m_{top}| < 50$ GeV

Background processes involving Standard Model $t\bar{t}$ production and decay (Figure 40), $t\bar{t} \to$ WbWb, which are a large part of the background to this search, can be rejected by requiring exactly one b-tagged jet. The rejection power of this cut is illustrated in Figure 41, which shows the b-tagged jet multiplicity after the pre-selection.

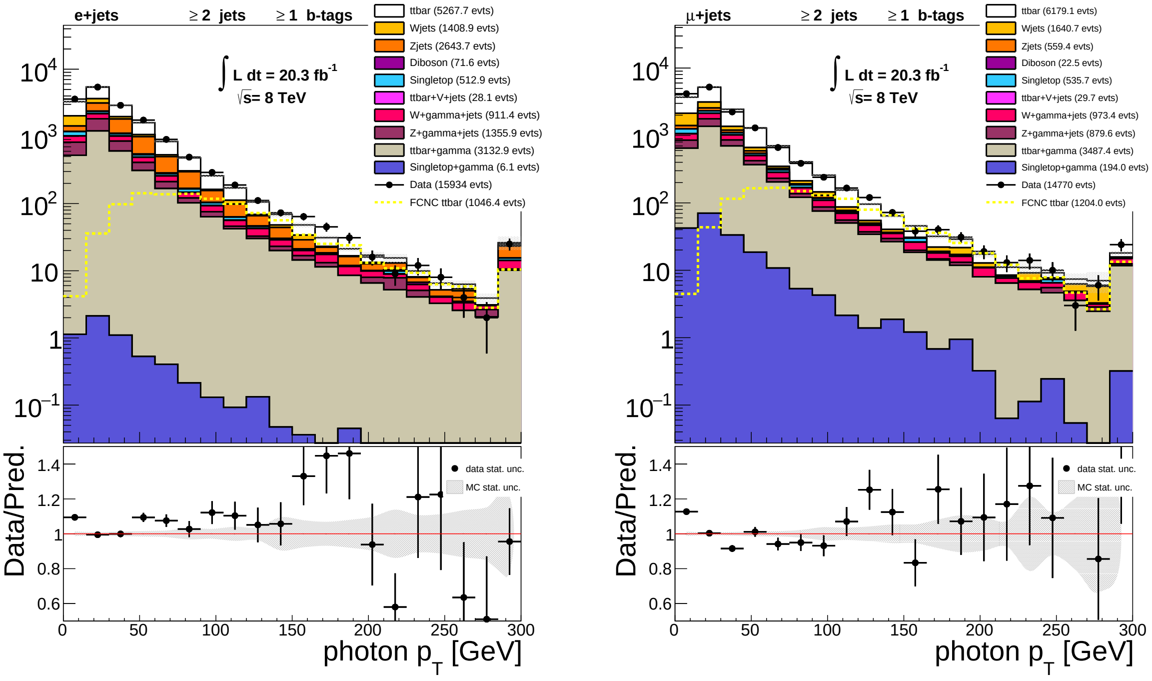

(a) electron channel

(b) muon channel

FIGURE 38. Photon candidate p_{T} after the signal region pre-selection, in the electron and muon channels. FCNC signal BR($t \to q\gamma$) is scaled to 1% on these plots. A photon candidate p_{T} cut of 50 GeV is applied to the final signal selection.

The Z+jets background (as shown in Figure 42) is a large contribution to the signal region in the electron channel. Z+jets events can enter the signal region if the Z boson decays to an electron-positron pair, and one electron is mis-reconstructed as a photon. This background can be rejected by eliminating events with invariant mass m(e, γ) within 5 GeV of the Z boson mass, 91 GeV, as shown in Figure 43.

Signal-like events should have several high-p_{T} objects in the final state. Therefore, the variable S_T is a good discriminator between signal and background. S_T is the scalar sum of the p_{T} of each object in the event, plus $E_{\mathrm{T}}^{\mathrm{miss}}$. This takes into account all of the visible objects, as well as the neutrino, which is not visible in the detector. The S_T distribution after pre-selection is shown in Figure 44.

Selected events in the signal region are selected to have reconstructed top candidate masses m($\ell\nu b$) and m($q\gamma$) within 50 GeV and 20 GeV of the top mass, 172.5 GeV, as shown in Figure 45. The single best discriminator between signal and background is the FCNC top candidate mass, m($q\gamma$).

Further plots for the signal pre-selection (photon, lepton, and jet p_{T}, $E_{\mathrm{T}}^{\mathrm{miss}}$, $m_{\mathrm{T}}^{\mathrm{W}}$, and jet multiplicity) are shown in Figures 46 and Figure 47, for the electron and muon channels, respectively.

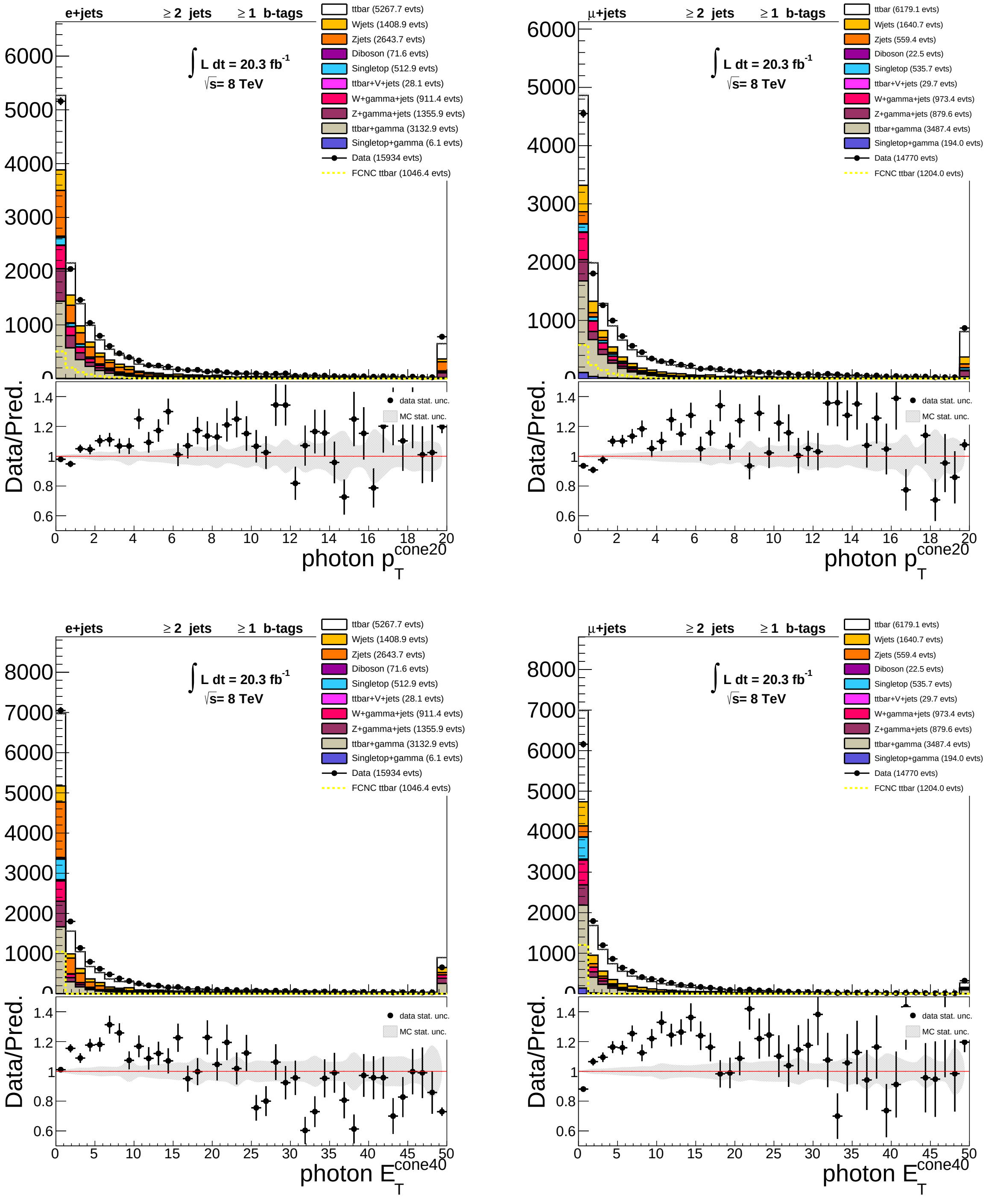

(a) electron channel

(b) muon channel

FIGURE 39. Photon isolation variables, after the signal region pre-selection, in the electron and muon channels. FCNC signal BR($t \rightarrow q\gamma$) is scaled to 1% on these plots. Isolation cuts of topoE$_T$cone40 < 4 GeV and p$_T$cone20 < 3 GeV are applied to the final signal selection.

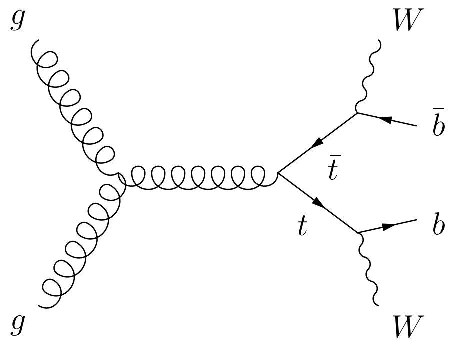

FIGURE 40. SM $t\bar{t}$ production and decay

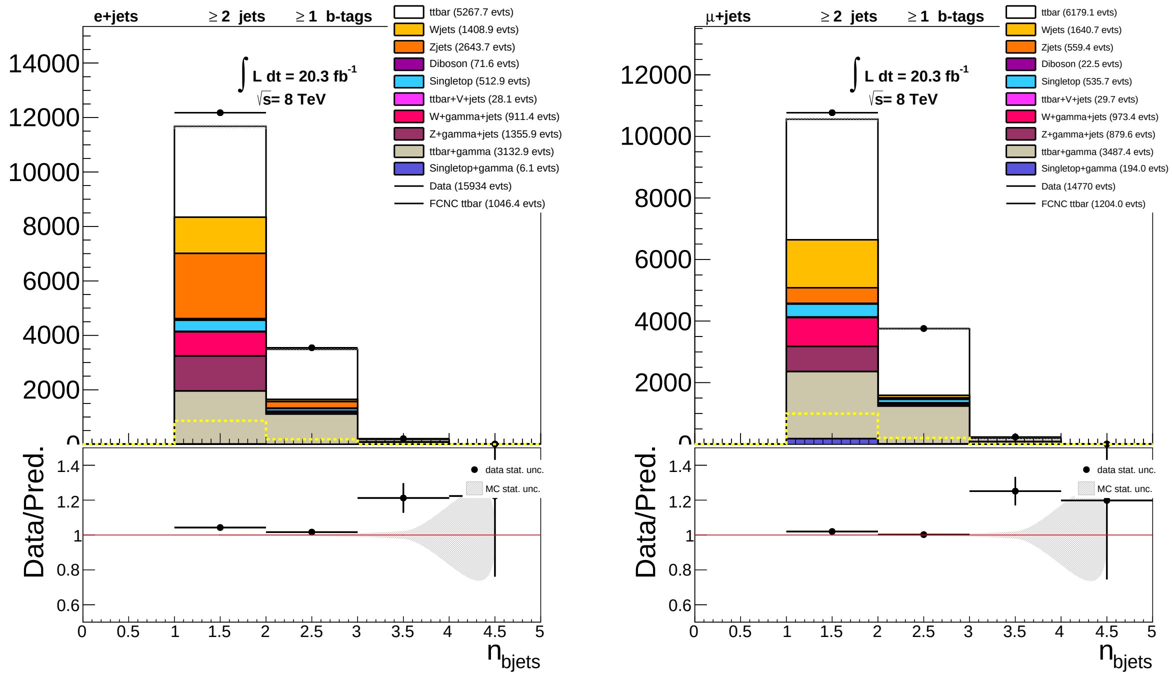

(a) electron channel (b) muon channel

FIGURE 41. B-tagged jet multiplicity after the signal region pre-selection, in the electron and muon channels. FCNC signal BR($t \rightarrow q\gamma$) is scaled to 1% on these plots. For the final signal selection, events with exactly one b-tagged jet are chosen.

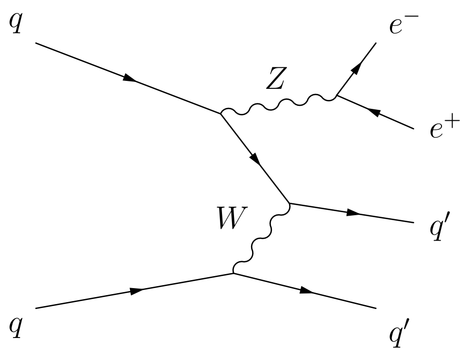

FIGURE 42. $Z \rightarrow e^+e^- + \text{jets}$

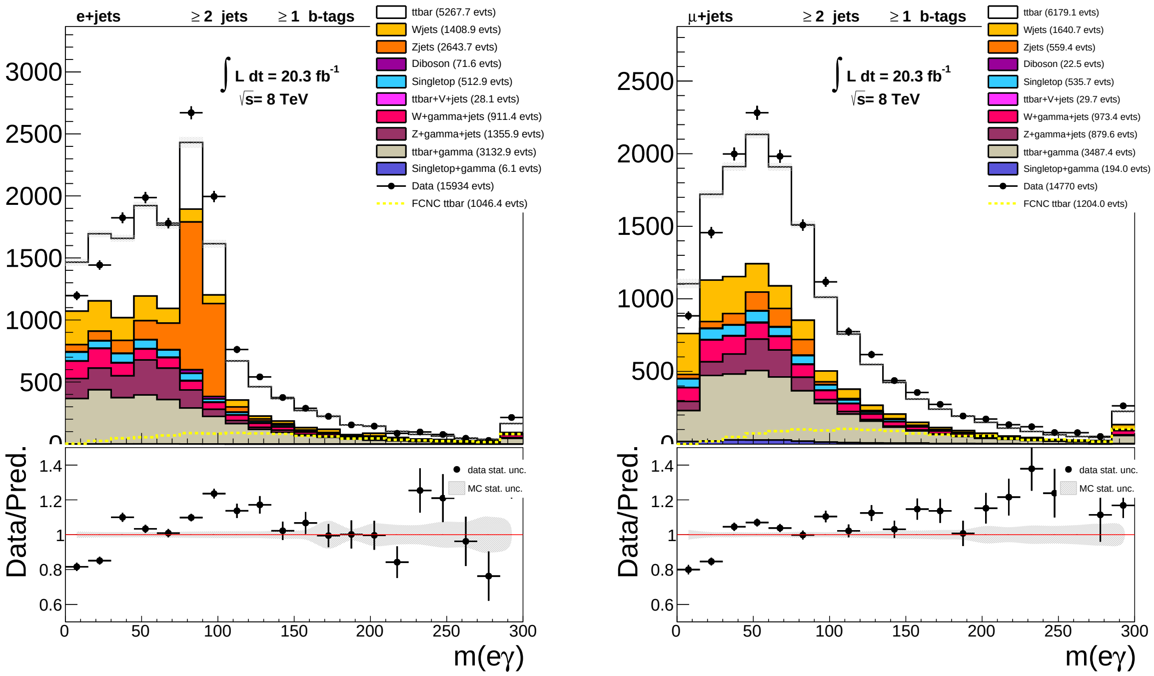

(a) electron channel

(b) muon channel

FIGURE 43. Invariant mass of the electron and photon candidates, m($e\gamma$), after the signal region pre-selection, in the electron and muon channels. FCNC signal BR($t \rightarrow q\gamma$) is scaled to 1% on these plots. A cut of |m($e\gamma$) - m$_Z$| > 5 GeV is applied to the final signal selection.

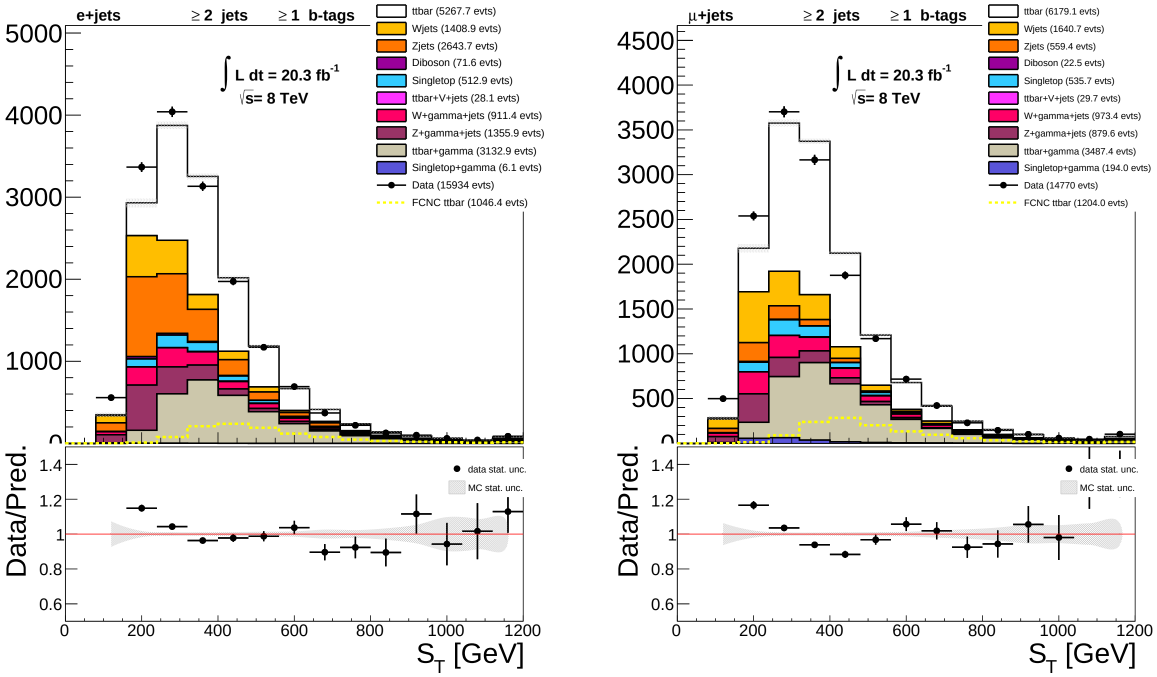

(a) electron channel

(b) muon channel

FIGURE 44. S_T after the signal region pre-selection, in the electron and muon channels. FCNC signal BR($t \rightarrow q\gamma$) is scaled to 1% on these plots. A cut of $S_T >$ 375 GeV is applied to the final signal selection.

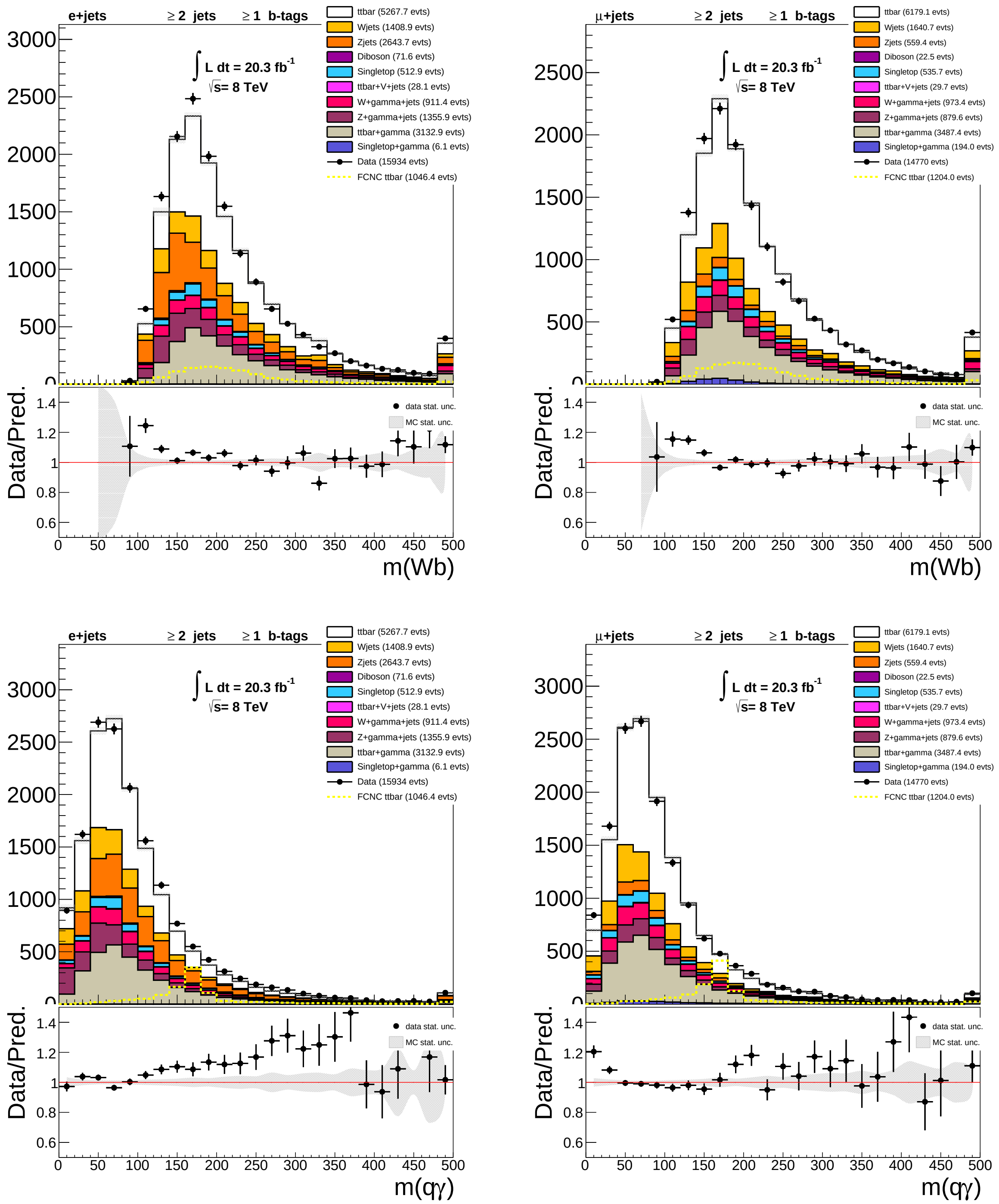

(a) electron channel

(b) muon channel

FIGURE 45. Candidate top masses, m($\ell\nu b$) and m($q\gamma$), after the signal region preselection, in the electron and muon channels. FCNC signal BR($t \to q\gamma$) is scaled to 1% on these plots. Cuts |m(Wb) - m$_{top}$| $<$ 50 GeV and |m($q\gamma$) - m$_{top}$| $<$ 20 GeV are applied to the final signal selection.

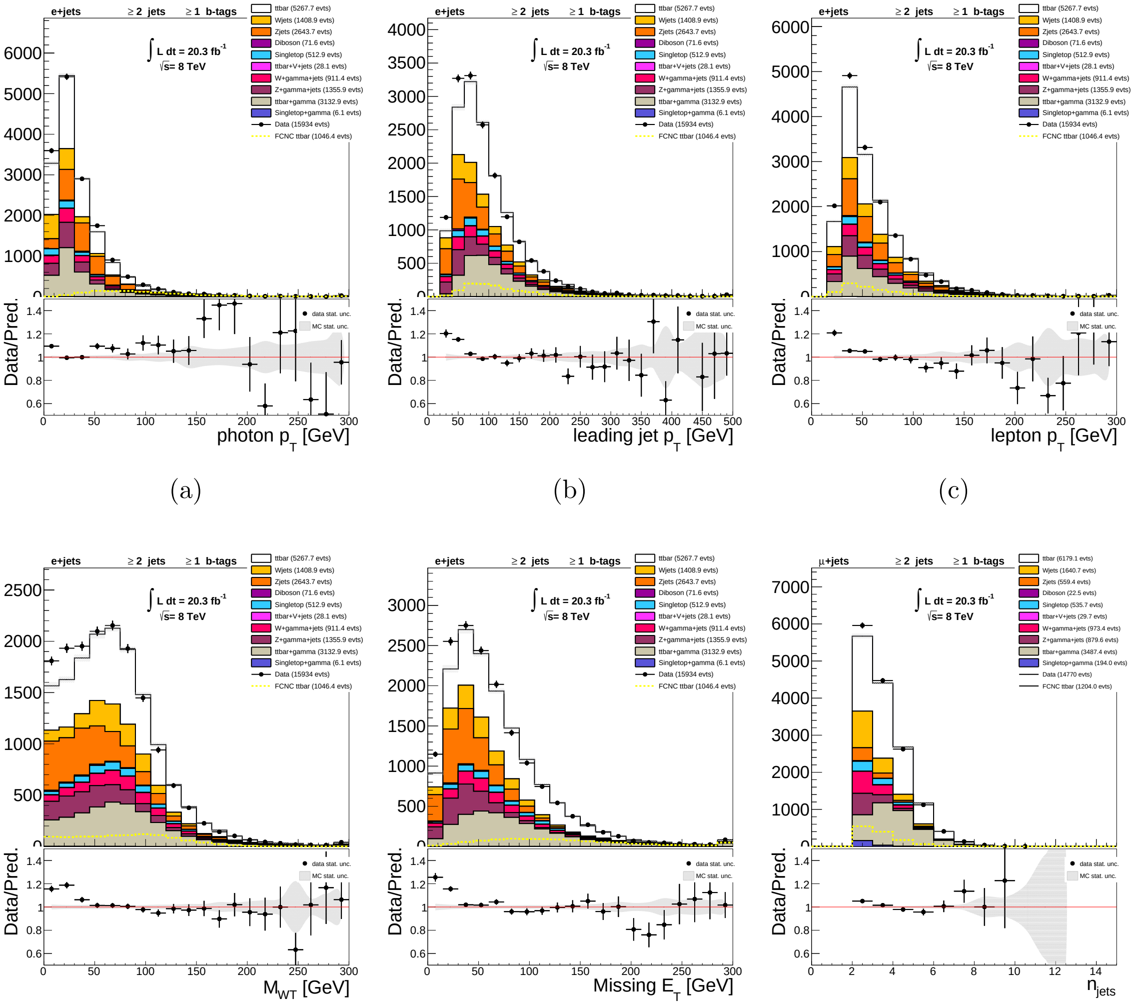

(a) (b) (c)

(d) (e) (f)

FIGURE 46. Photon p_{T} (a), leading jet p_{T} (b), lepton p_{T} (c), $m_{\mathrm{T}}^{\mathrm{W}}$(d), $E_{\mathrm{T}}^{\mathrm{miss}}$ (e), and N$_{jets}$ (f) plots in the signal pre-selection region (electron channel)

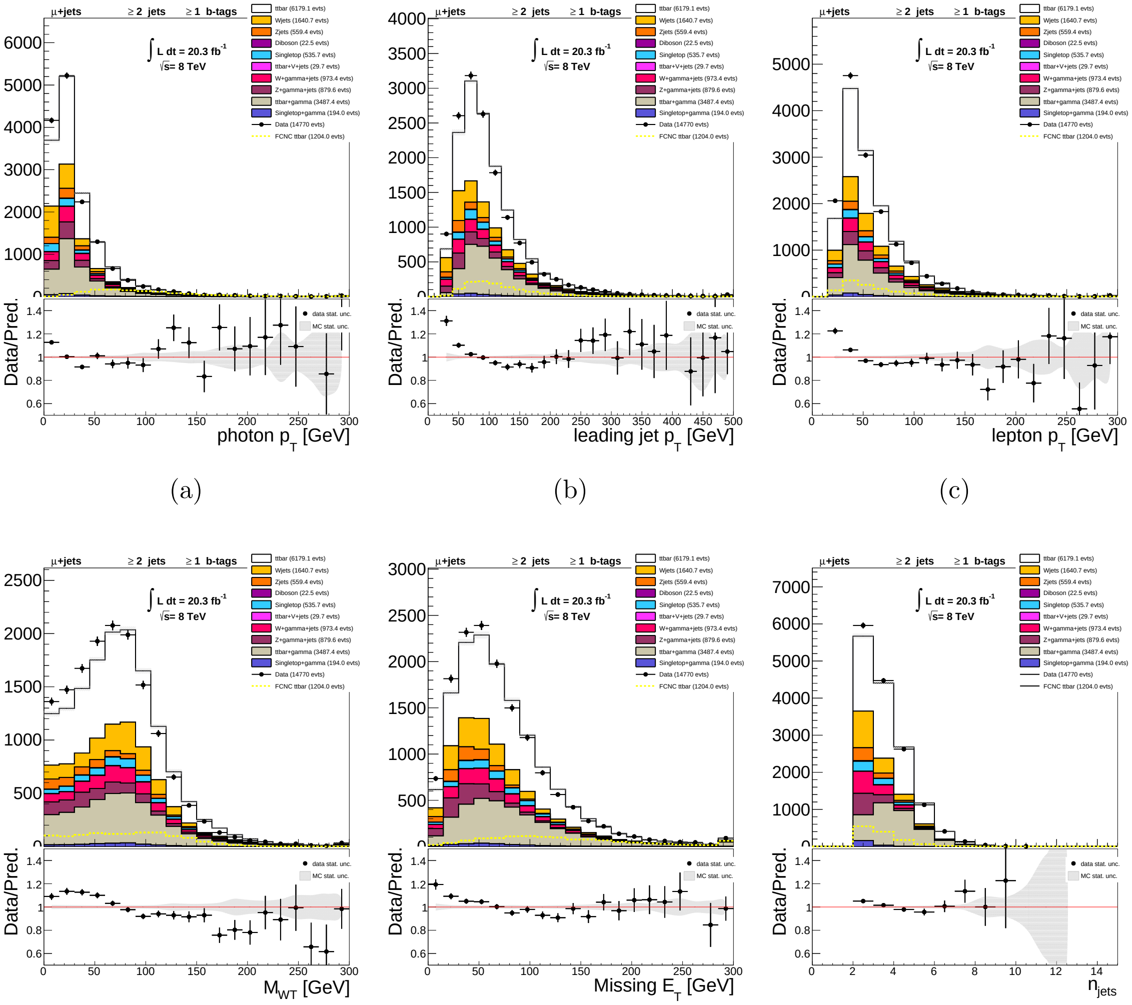

(a) (b) (c)

(d) (e) (f)

FIGURE 47. Photon p_{T} (a), leading jet p_{T} (b), lepton p_{T} (c), $m_{\mathrm{T}}^{\mathrm{W}}$(d), $E_{\mathrm{T}}^{\mathrm{miss}}$ (e), and N$_{jets}$ (f) plots in the signal pre-selection region (muon channel)

5.4. Background Evaluation

In order to test the performance of the Monte Carlo samples, control regions are designed to isolate different physics processes. Scale factors which will scale the backgrounds to the data in the control regions can be determined and then tested in another region, for validation. The control and validation regions should be close enough to the signal region so that the derived scale factors can be translated into the signal region. The control and validation region selections should be orthogonal to the signal region selection, so that there is no signal contamination. The main backgrounds are Standard Model $t\bar{t}$ events ($t\bar{t} \rightarrow WbWb$) and W+jets events, as well as $t\bar{t}$ and W+jets events produced with an associated photon ($t\bar{t}$ $+\gamma$, $W$$+\gamma$). In order to best characterize those backgrounds, control regions are defined in the next sections.

5.4.1. Backgrounds With Real Photons

Standard Model processes with an extra real photon are irreducible. $t\bar{t}$ $+\gamma$ and $W$$+\gamma$ +jets backgrounds are the largest contributors to this region. Overlapping events between W+jets and $W$$+\gamma$ backgrounds and $t\bar{t}$ and $t\bar{t}$ $+\gamma$ backgrounds are removed using the `MCTruthClassifier` tool. Signal photons, which do not originate from hadrons or leptons, as identified by the `MCTruthClassifier` tool, are removed from the $t\bar{t}$ MC sample and from the W+jets MC sample.

5.4.1.1. $W$$+\gamma$

The $W$$+\gamma$ validation region selection is as follows:

- OR lowest un-prescaled isolated and non-isolated triggers

– Require a primary vertex with $\mathrm{N}_{tracks} > 4$

– Exactly one good lepton ($p_{\mathrm{T}} > 25$ GeV)

– Require trigger matching

– Overlap removal

– At least 2 good jets ($p_{\mathrm{T}} > 25$ GeV)

– $E_{\mathrm{T}}^{\mathrm{miss}} > 30$ GeV and $m_{\mathrm{T}}^{\mathrm{W}} > 30$ GeV (electron channel)

– $E_{\mathrm{T}}^{\mathrm{miss}} > 20$ GeV and $E_{\mathrm{T}}^{\mathrm{miss}} + m_{\mathrm{T}}^{\mathrm{W}} > 60$ GeV (muon channel)

– Exactly zero b-tagged jets (MV1 at 70%)

– Exactly one good photon with $p_{\mathrm{T}} > 50$ GeV

– Photon isolation cuts: p_{T} cone20 $<$ 3 GeVand topoE_{T} cone40 $<$ 4 GeV

– Z mass cut: $|\mathrm{m}(e\gamma)$ - $\mathrm{m}_Z| > 5$ GeV

Sample distributions in the W+γ validation region are compared in Figures 48 and 49.

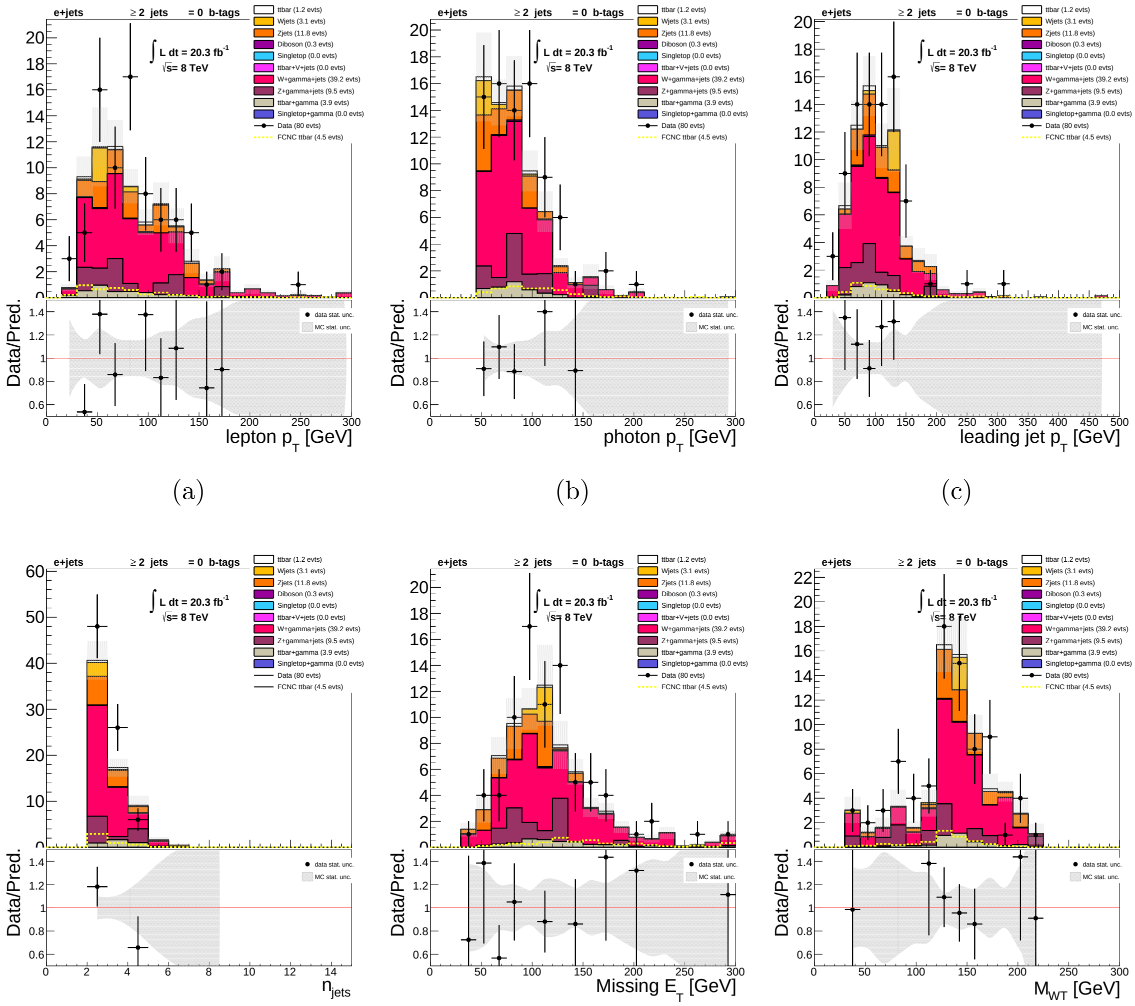

(a) (b) (c)

(d) (e) (f)

FIGURE 48. Lepton p_{T} (a), photon p_{T} (b), leading jet p_{T} (c), N_{jets} (d), $E_{\mathrm{T}}^{\mathrm{miss}}$ (e), and $m_{\mathrm{T}}^{\mathrm{W}}$(f) distributions for the $W+\gamma$ validation region (electron channel). FCNC signal BR($t \to q\gamma$) is scaled to 0.1%

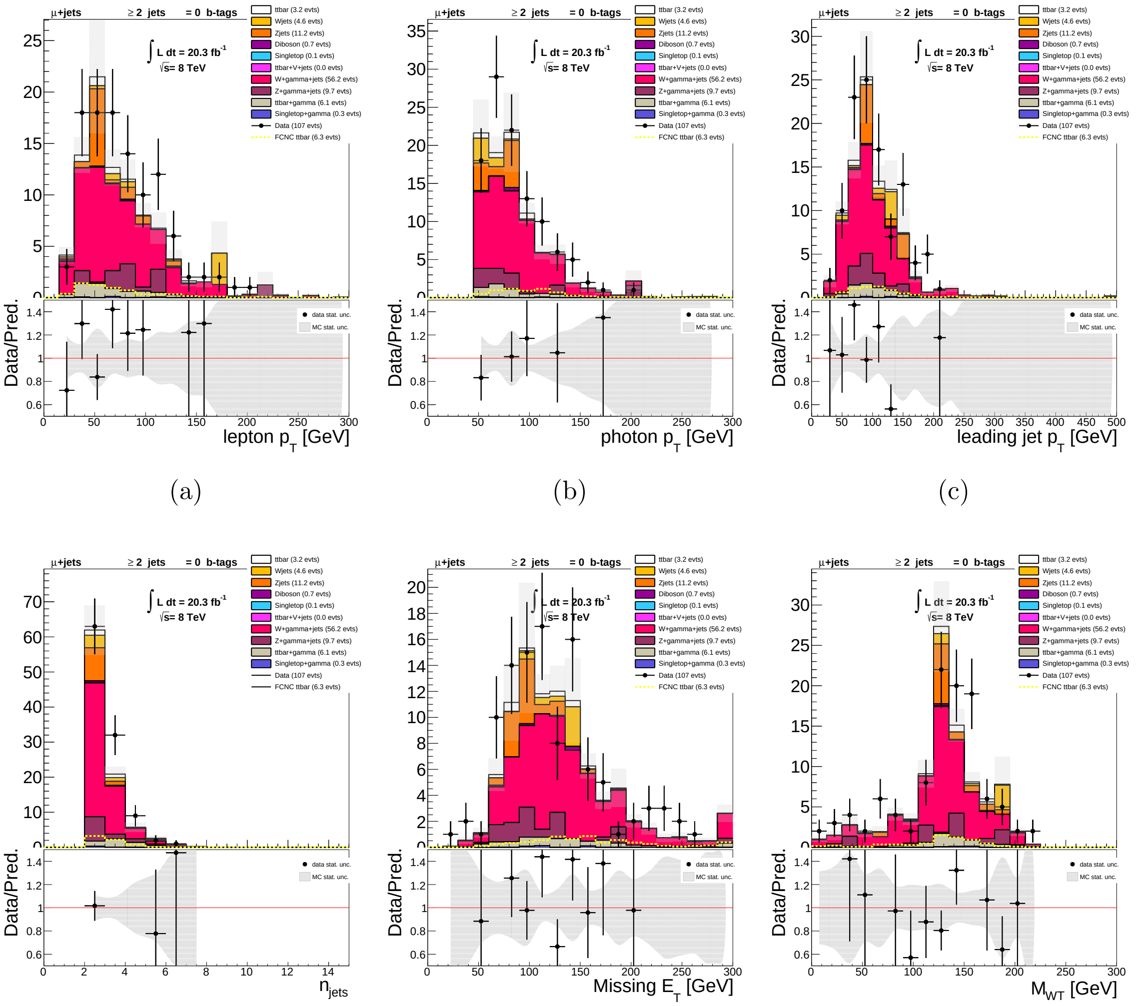

(a) (b) (c)

(d) (e) (f)

FIGURE 49. Lepton p_{T} (a), photon p_{T} (b), leading jet p_{T} (c), N_{jets} (d), $E_{\mathrm{T}}^{\mathrm{miss}}$ (e), and $m_{\mathrm{T}}^{\mathrm{W}}$(f) distributions for the W+γ validation region (muon channel). FCNC signal BR($t \to q\gamma$) is scaled to 0.1%

5.4.1.2. $t\bar{t}$ +γ

The $t\bar{t}$ +γ validation region selection is as follows:

- OR lowest un-prescaled isolated and non-isolated triggers
- Require a primary vertex with $\mathrm{N}_{tracks} > 4$
- Exactly one good lepton ($p_{\mathrm{T}} > 25$ GeV)
- Require trigger matching
- Overlap removal
- At least 4 good jets ($p_{\mathrm{T}} > 25$ GeV)
- $E_{\mathrm{T}}^{\mathrm{miss}} > 30$ GeV and $m_{\mathrm{T}}^{\mathrm{W}} > 30$ GeV (electron channel)
- $E_{\mathrm{T}}^{\mathrm{miss}} > 20$ GeV and $E_{\mathrm{T}}^{\mathrm{miss}} + m_{\mathrm{T}}^{\mathrm{W}} > 60$ GeV (muon channel)
- At least 1 b-tagged jet (MV1 at 70%)
- Exactly one good photon with $p_{\mathrm{T}} > 15$ GeV
- Reverse m(qγ) cut – orthogonal to FCNC signal region
- Photon isolation cuts, as in signal region

The $t\bar{t}$ +γ validation region is shown in Figures 50 and 51. These distributions include the same photon isolation cuts used in the signal selection: p_{T} cone20 < 3 GeVand topoE_{T} cone40 < 4 GeV. Good data-MC agreement is observed.

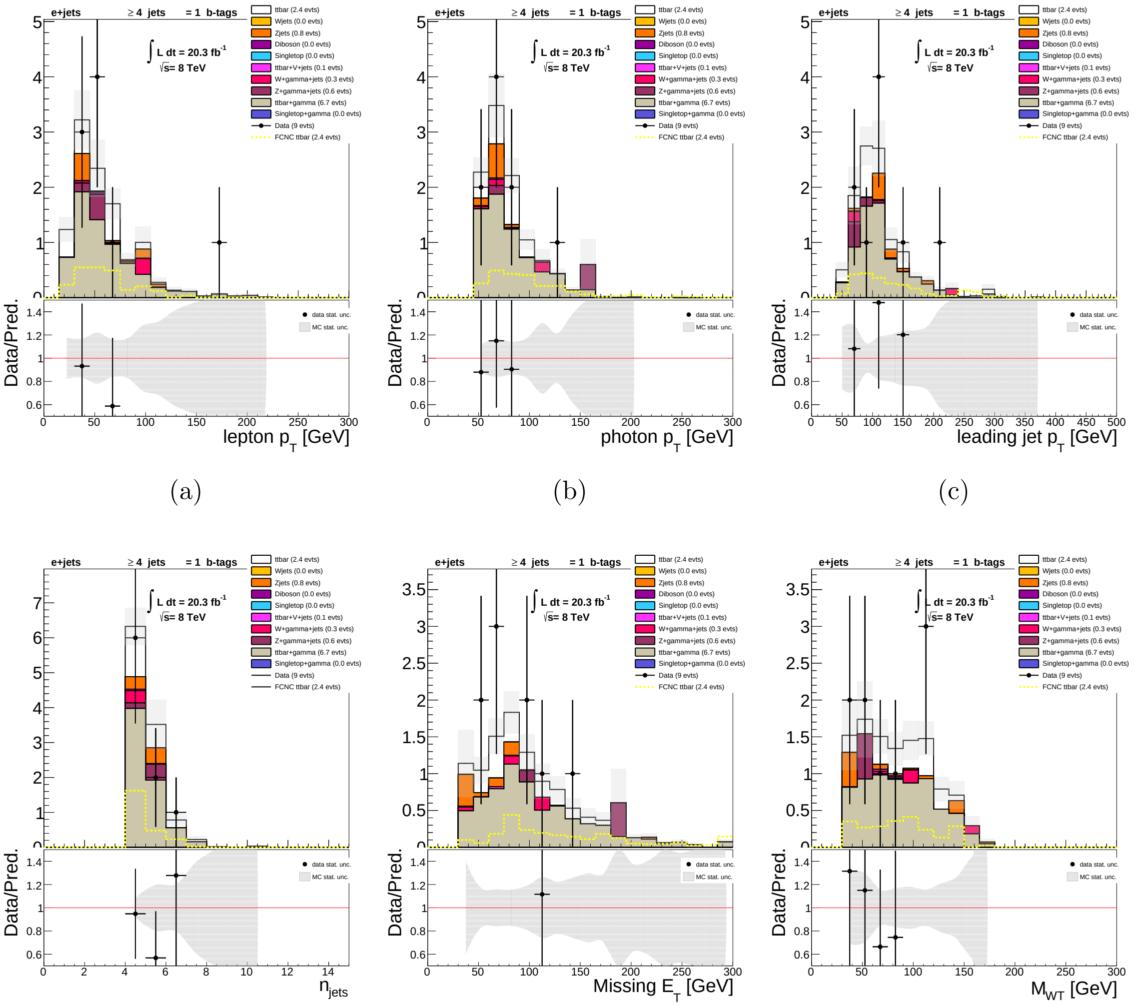

(a) (b) (c)

(d) (e) (f)

FIGURE 50. Lepton p_{T} (a), photon p_{T} (b), leading jet p_{T} (c), N_{jets} (d), $E_{\mathrm{T}}^{\mathrm{miss}}$ (e), and $m_{\mathrm{T}}^{\mathrm{W}}$(f) distributions in the $t\bar{t}$ $+\gamma$ validation region (electron channel). FCNC signal BR($t \to q\gamma$) is scaled to 0.1%.

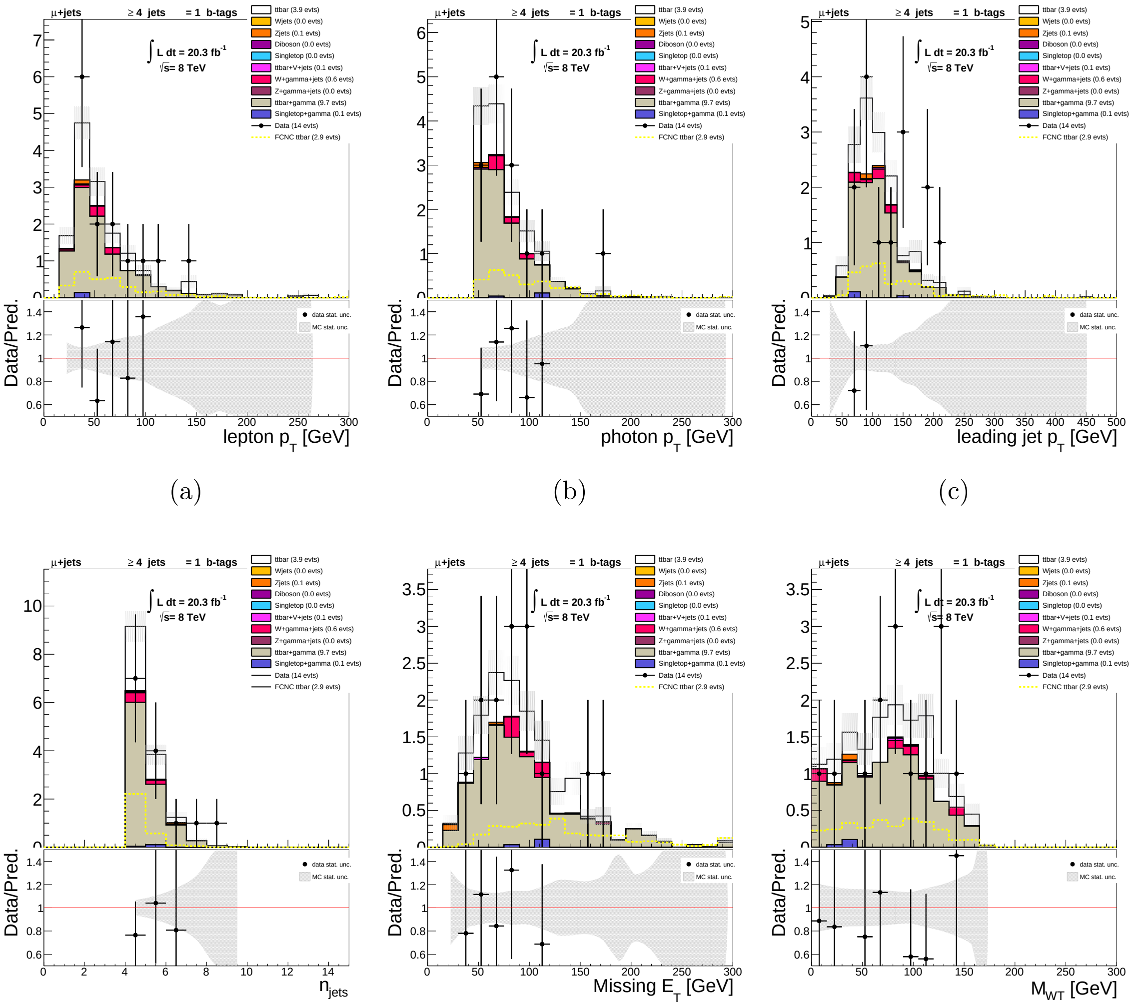

(a) (b) (c)

(d) (e) (f)

FIGURE 51. Lepton p_{T} (a), photon p_{T} (b), leading jet p_{T} (c), N_{jets} (d), $E_{\mathrm{T}}^{\mathrm{miss}}$ (e), and $m_{\mathrm{T}}^{\mathrm{W}}$(f) distributions in the $t\bar{t}$ $+\gamma$ validation region (muon channel). FCNC signal BR($t \to q\gamma$) is scaled to 0.1%.

5.4.2. Backgrounds With No Real Photons

Background processes that contain no real photons can enter the signal region if an electron or jet is mis-reconstructed as a photon. Standard Model $t\bar{t}$ and W+jets production are the largest contributors. Two control regions are designed to isolate the $t\bar{t}$ and W+jets processes. It is difficult to design a single $t\bar{t}$ or W+jets control region which is adequately close to the signal region, so two regions are designed, one of which is W+jets-rich and the other which is $t\bar{t}$-rich. Scale factors are derived from both regions simultaneously, and then tested in a validation region, before being applied in the signal region.

The $t\bar{t}$ and W+jets control region selection is as follows:

- OR lowest un-prescaled isolated and non-isolated triggers
- Require a primary vertex with $\mathrm{N}_{tracks} > 4$
- Exactly one good lepton ($p_{\mathrm{T}} > 25$ GeV)
- Require trigger matching
- Overlap removal
- At least 3/4/5+ good jets ($p_{\mathrm{T}} > 25$ GeV)
- $E_{\mathrm{T}}^{\mathrm{miss}} > 30$ GeV and $m_{\mathrm{T}}^{\mathrm{W}} > 30$ GeV (electron channel)
- $E_{\mathrm{T}}^{\mathrm{miss}} > 20$ GeV and $E_{\mathrm{T}}^{\mathrm{miss}} + m_{\mathrm{T}}^{\mathrm{W}} > 60$ GeV (muon channel)
- Exactly one b-tagged jet (MV1 at 70% - at least one good jet has MV1 > 0.7892)
- Zero good photons with $p_{\mathrm{T}} > 10$ GeV

The region with exactly three jets is the W+jets-rich region, while the region with 5+ jets is the $t\bar{t}$-rich region. The efficacy of the scale factors can then be tested in the validation region, which has exactly 4 jets, before being applied to the signal region. The S_T distribution is shown for all three regions in Figure 52.

Scale factors for the $t\bar{t}$ and W+jets MC are then derived as follows:

$$\begin{bmatrix} N(W)_{3j} & N(t\bar{t})_{3j} \\ N(W)_{5j} & N(t\bar{t})_{5j} \end{bmatrix} \begin{bmatrix} W_{SF} \\ t\bar{t}_{SF} \end{bmatrix} = \begin{bmatrix} N(data - bkg)_{3j} \\ N(data - bkg)_{5j} \end{bmatrix}$$

Figures 53 and 54 show the control region distributions after the scale factors are applied:

- $W_{SF} = 1.29(1.26)$, e(μ)
- $t\bar{t}_{SF} = 0.98(0.96)$, e($\mu$)

The derived scale factors are then applied to the $t\bar{t}$ and W+jets MC in the signal region.

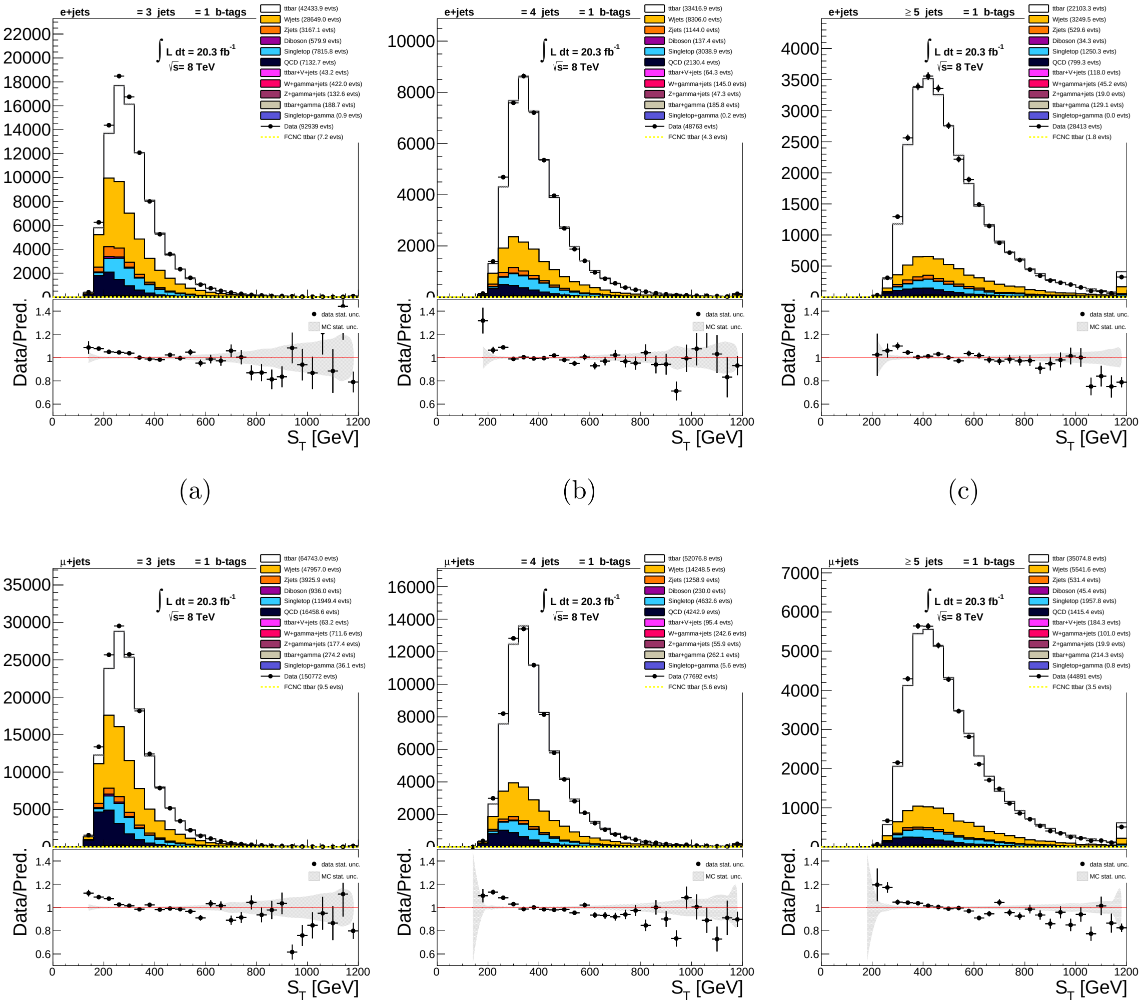

(a) (b) (c)

(d) (e) (f)

FIGURE 52. S_T distribution in 3, 4, and 5+ jets $t\bar{t}/W$+jets control region, before scale factors are determined

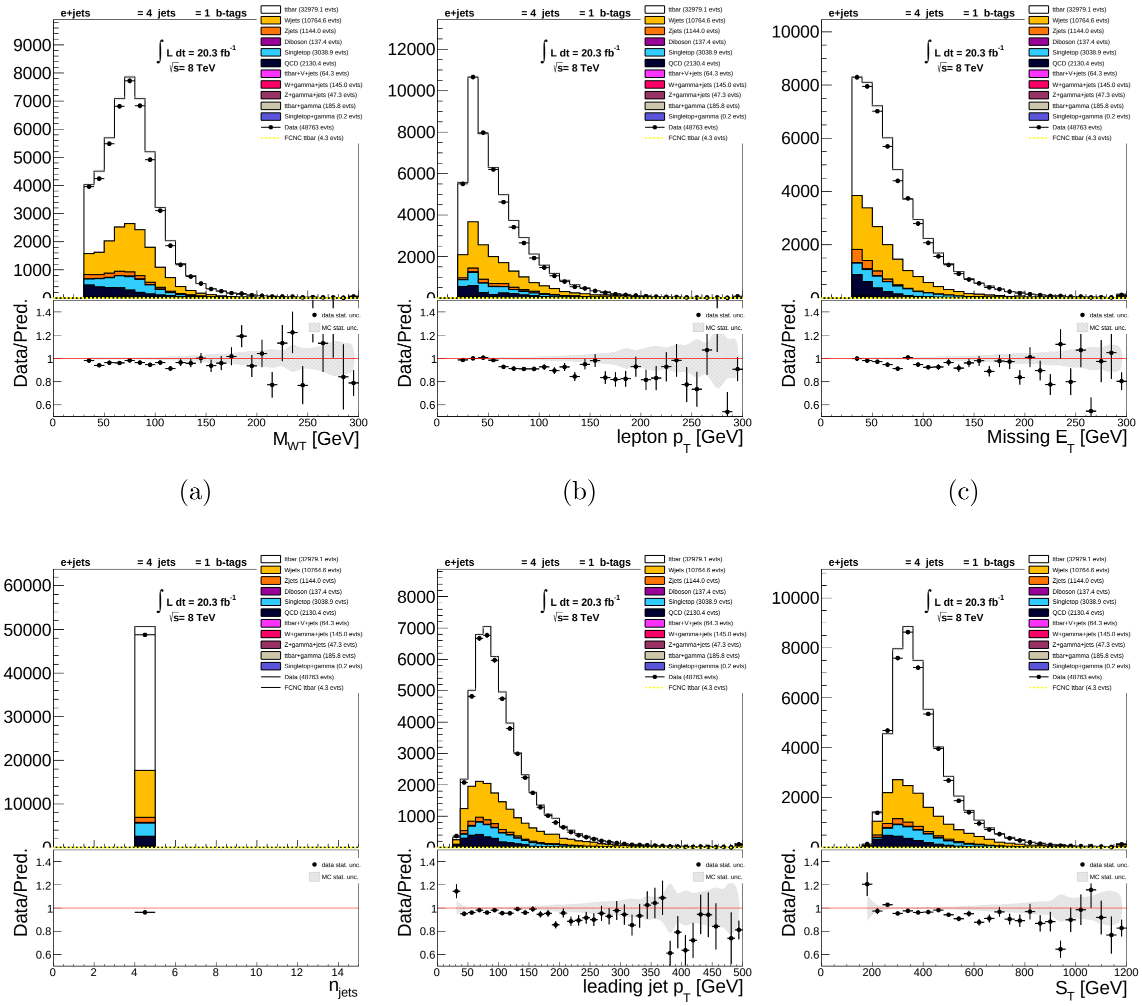

(a) (b) (c)

(d) (e) (f)

FIGURE 53. Event-level variables in $t\bar{t}$ and W+jets validation region with exactly 4 jets (electron channel), after scale factors are applied

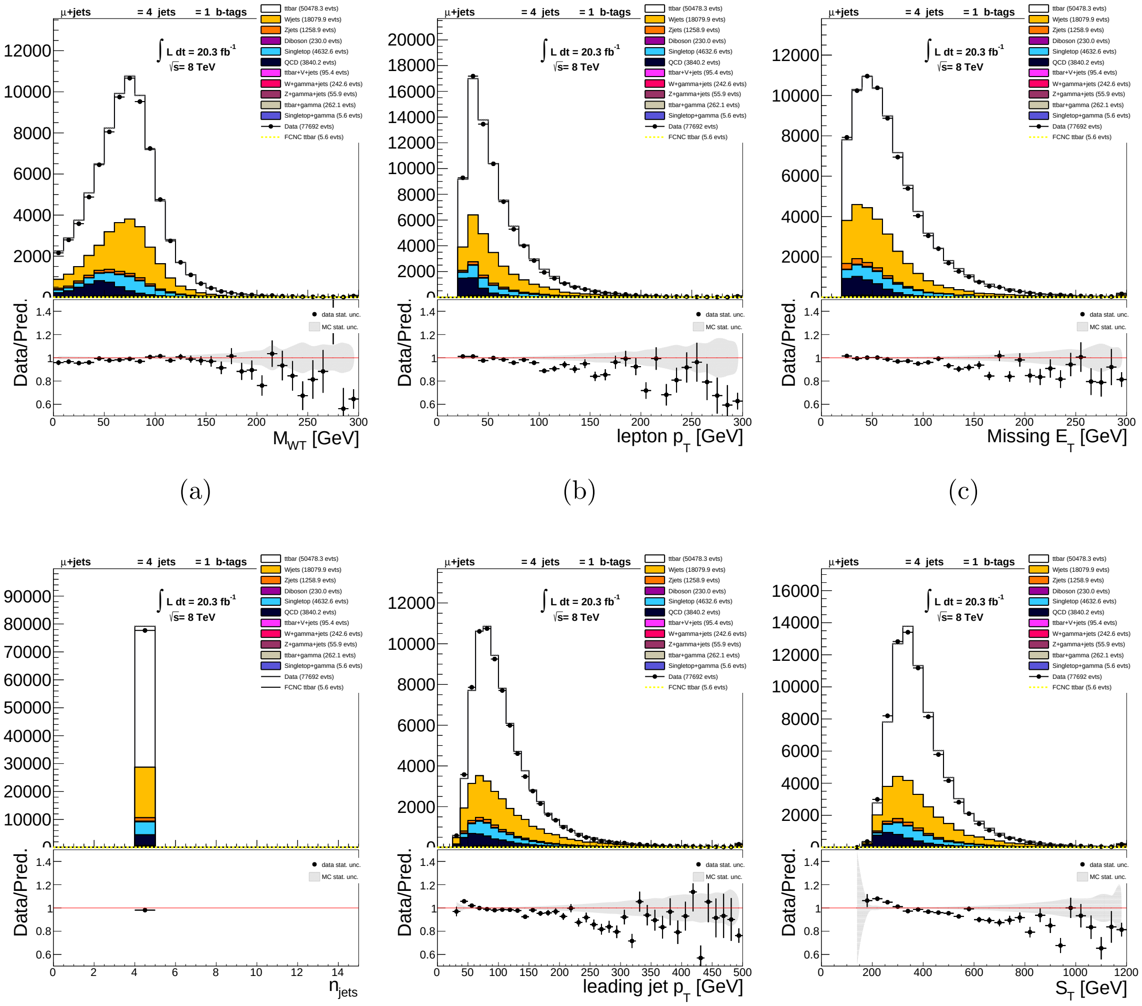

(a) (b) (c)

(d) (e) (f)

FIGURE 54. Event-level variables in $t\bar{t}$ and W+jets validation region with exactly 4 jets (muon channel), after scale factors are applied

5.4.3. $e \to \gamma$ Fakes

There are several scenarios in which electrons can be reconstructed as photons with the ATLAS detector. For example, if it is not possible to associate the track and the shower in the electromagnetic calorimeter, the object can be misreconstructed as a photon instead of an electron. Similarly, if an electron radiates all of its energy to a photon, the object will be correctly reconstructed as a photon, but does not correspond to a signal-like prompt photon, since it came from an electron.

Therefore, backgrounds with an extra real electron can enter the signal region: dilepton $t\bar{t}$ events where both W bosons decay to an electron and a neutrino, $Z \to \ell^+\ell^-$ events with two electrons, or a variety of diboson events with more than one electron in the final state. $Z \to e^+e^-$ and $Z \to e``\gamma"$ processes are shown in Figure 55. Since the rate of $e \to \gamma$ fakes is slightly different in data and MC, it is possible to identify (in data and MC) how often electrons are reconstructed as photons, and then apply an appropriate scale factor to MC events which contain a fake photon.

A tag-and-probe method is used to determine the rate of $e \to \gamma$ fakes in data and in $Z \to e^+e^-$ MC. A $Z \to e^+e^-$ selection is designed to be similar to the signal selection:

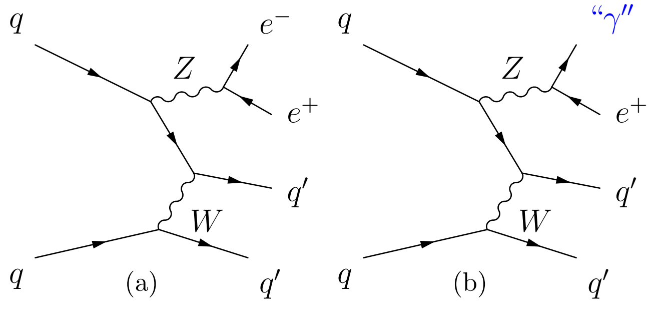

FIGURE 55. $Z \to e^+e^-$+jets and $Z \to e``\gamma"$+jets

- OR lowest unprescaled isolated and non-isolated triggers:
    - Electron triggers: EF_e24vhi_medium1 and EF_e60_medium1
- Require a primary vertex with $N_{tracks} > 4$
- At least one good electron ($p_T > 25$ GeV)
- Require trigger matching
- At least two good jets ($p_T > 25$ GeV)
- $E_{\mathrm{T}}^{\mathrm{miss}} > 30$ GeV
- At least one b-tagged jet (MV1 @ 70%)
- At least one more electron ($p_T > 15$ GeV)
- 86 GeV < $m(e^+e^-)$ < 96 GeV (Z mass requirement)

Then, a $Z \rightarrow e\gamma$ selection is defined:

- OR lowest unprescaled isolated and non-isolated triggers:
    - Electron triggers: EF_e24vhi_medium1 and EF_e60_medium1
- Require a primary vertex with $N_{tracks} > 4$
- At least one good electron ($p_T > 25$ GeV)
- Require trigger matching
- At least two good jets ($p_T > 25$ GeV)
- $E_{\mathrm{T}}^{\mathrm{miss}} > 30$ GeV
- At least one b-tagged jet (MV1 @ 70%)

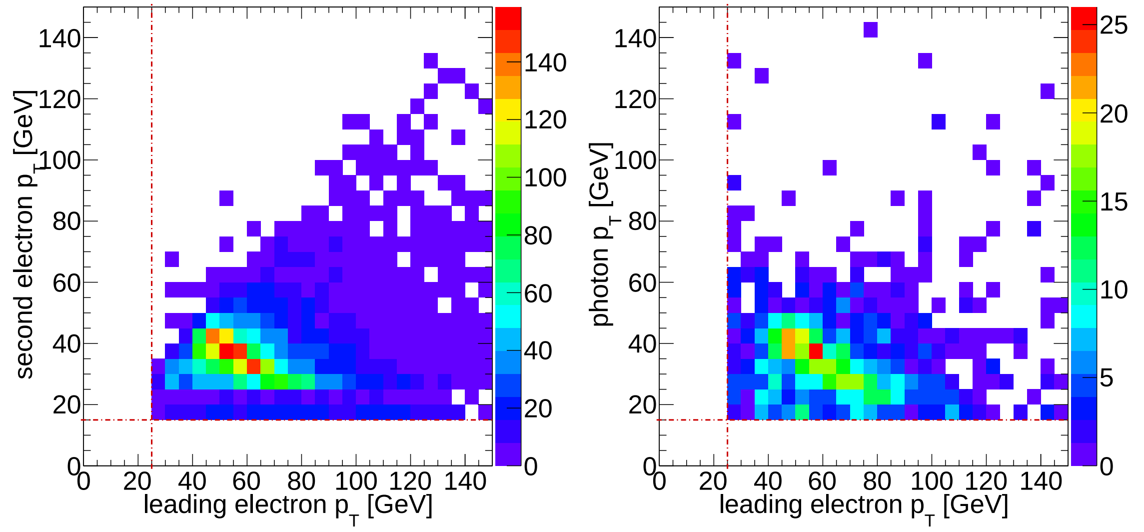

(a)

(b)

FIGURE 56. Sub-leading electron p_{T} vs. leading electron p_{T} (a) and photon p_{T} vs. leading electron p_{T} (b), in data

- At least one good photon ($p_T > 15$ GeV)

- 86 GeV < m(e“γ”) < 96 GeV (Z mass requirement)

The p_{T} distribution for the leading and sub-leading electrons, and for the electron and photon candidate, for data and MC, are shown in Figures 56 and 57.

To determine the fake rate: Select ($Z \rightarrow e^+e^-$ + jets + MET) and ($Z \rightarrow e$“γ” + jets + MET) events, with m(e^+e^-) and m(e“γ”) near the Z mass. Then, $\dfrac{N(e“\gamma”)}{N(e^+e^-) + N(e“\gamma”)}$ = fake rate. The fake rate is shown, binned by photon candidate p_{T} and η, in Figure 58. We are only interested in events which could enter the signal region, that is, where the fake photon has p_{T} greater than 50 GeV. The fake rate does not depend heavily on photon p_{T} above 50 GeV, as shown in Figure 59. The final fake rate (for high-p_{T} objects) in data and MC is shown in Figure 60, and listed in Table 10.

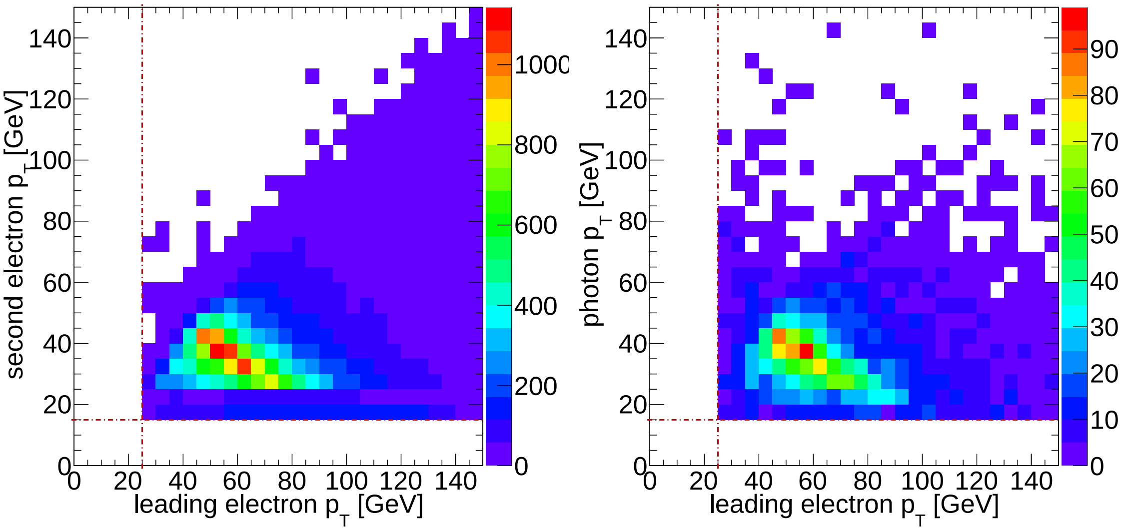

(a) (b)

FIGURE 57. Sub-leading electron p_{T} vs. leading electron p_{T} (a) and photon p_{T} vs. leading electron p_{T} (b), in $Z \to e^+e^-$ MC

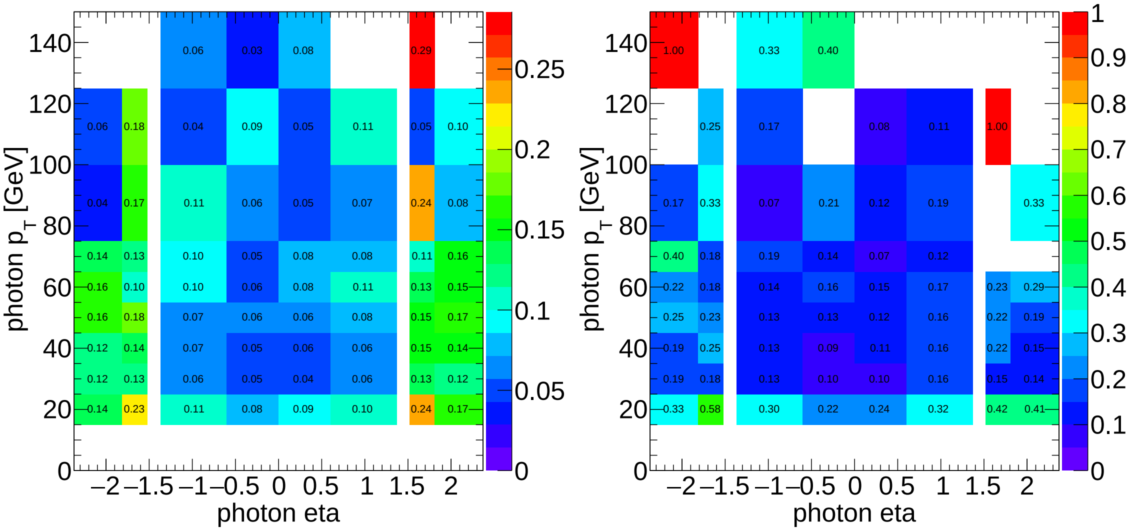

(a) (b)

FIGURE 58. $e \to \gamma$ fake rate in MC (a) and data (b), binned by photon candidate p_{T} and η.

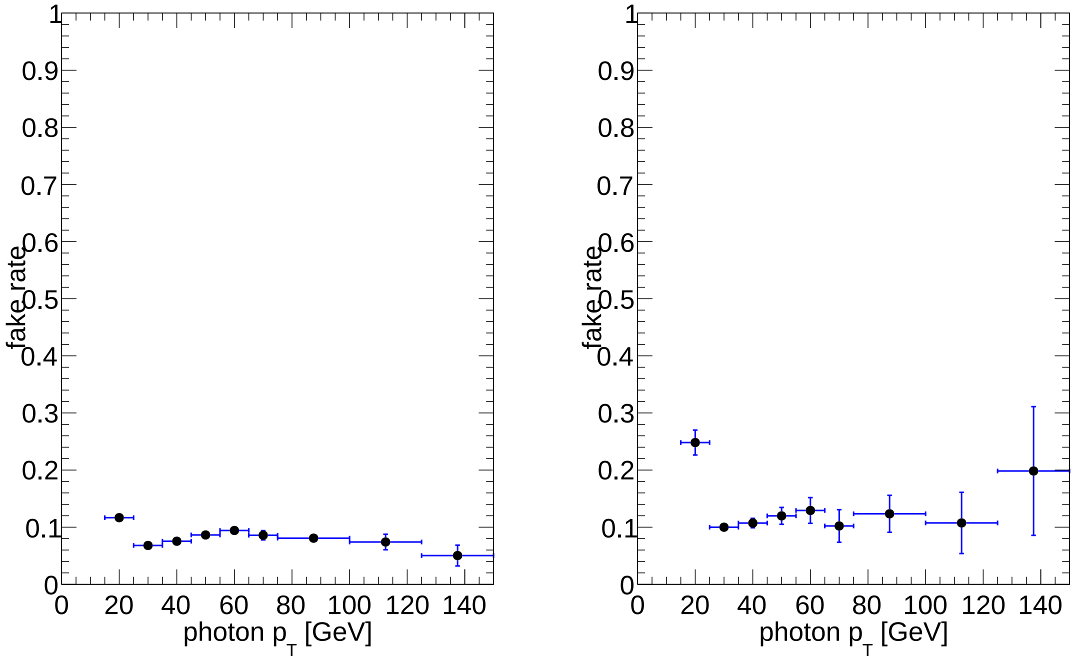

(a) (b)

FIGURE 59. $e \rightarrow \gamma$ fake rate in MC (a) and data (b) as a function of photon p_{T}

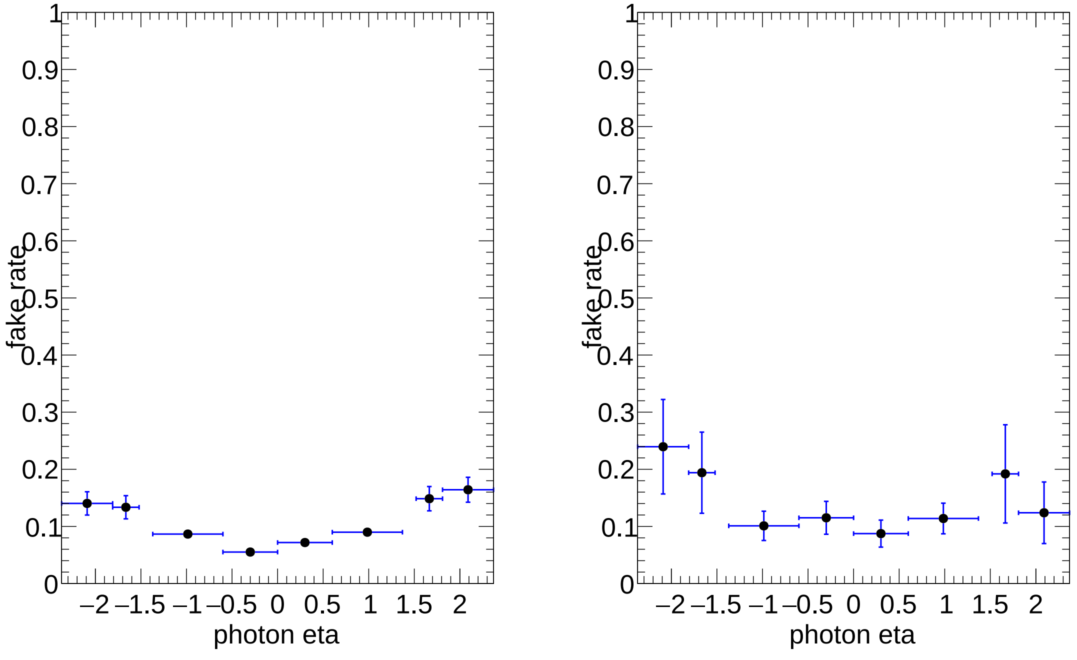

(a) (b)

FIGURE 60. $e \rightarrow \gamma$ fake rate in MC (a) and data (b) as a function of photon η, after photon candidate p_{T} cut

TABLE 10. Fake rate (F.R.) measured in $Z \rightarrow e^+e^-$ MC and in data. The data over MC scale factor (S.F.) is applied to events in MC identified by `MCTruthClassifer` as having originated from electrons.

$\gamma\ \eta$	0. - 0.6	0.6 - 1.37	1.52 - 1.81	1.81 - 2.37
Z MC F.R.	0.07 ± 0.01	0.09 ± 0.01	0.15 ± 0.02	0.16 ± 0.02
data F.R.	0.09 ± 0.02	0.11 ± 0.03	0.19 ± 0.09	0.12 ± 0.05
S.F. (data/Z)	1.22 ± 0.287	1.27 ± 0.249	1.29 ± 0.470	0.755 ± 0.455

5.4.4. Jet → Lepton and Jet → Photon Fakes

To estimate the number of jet fakes that enter the signal region, two methods are used. To estimate the multi-jet background with lepton fakes, the matrix method is used, and to estimate the multi-jet background with photon fakes, an ABCD method is used.

5.4.4.1. Matrix Method for Lepton Fakes

A data-driven matrix method [78] is used to determine the rate of jets faking leptons in semi-leptonic $t\bar{t}$ events. This method uses efficiencies for selecting tight and loose-only leptons in data, to estimate fake contributions.

5.4.4.2. ABCD Method for Photon Fakes

The multi-jet → photon background is modeled by dividing the data into four regions, where region A is the final signal selection, and regions B-D are background-enriched control regions that will be used to estimate the number of multi-jet events in region A. The distribution of data and signal MC are shown in Figure 61.

ABCD selection:

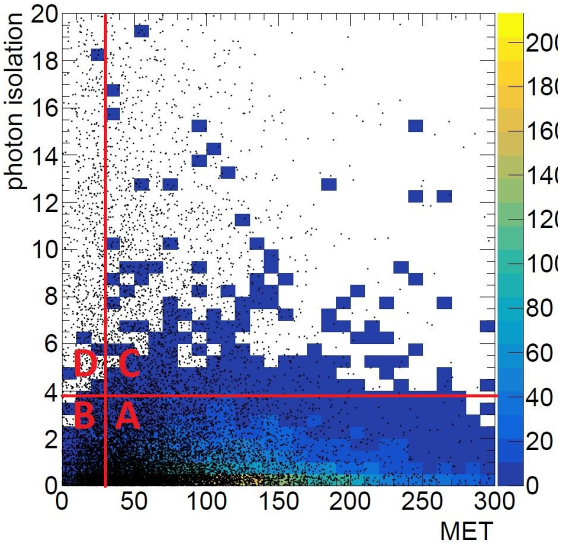

FIGURE 61. A,B,C, and D regions are shown for ABCD method cuts on $E_{\mathrm{T}}^{\mathrm{miss}}$ and photon isolation

TABLE 11. Jet to photon fake yield in electron and muon channels

	j $\rightarrow \gamma$ yield
electron channel	0.238 ± 1.65 (stat.)
muon channel	1.59 ± 1.75 (stat.)

A: isolated photon, $m_{\mathrm{T}}^{\mathrm{W}}$and $E_{\mathrm{T}}^{\mathrm{miss}}$ cuts

B: isolated photon, $m_{\mathrm{T}}^{\mathrm{W}}$and $E_{\mathrm{T}}^{\mathrm{miss}}$ cuts reversed

C: non-isolated photon, $m_{\mathrm{T}}^{\mathrm{W}}$and $E_{\mathrm{T}}^{\mathrm{miss}}$ cuts

D: non-isolated photon, $m_{\mathrm{T}}^{\mathrm{W}}$and $E_{\mathrm{T}}^{\mathrm{miss}}$ cuts reversed

Then, for each region, the difference between the data and the sum of the other background estimates (denoted "MC") is taken to be equivalent to the number of jet → photon fakes. We can then estimate the number of jet → photon fakes in region A with: $N^A_{fakes} = (N^B_{data} - N^B_{MC})(N^C_{data} - N^C_{MC})/(N^D_{data} - N^D_{MC})$. The jet → γ fake estimates are shown in Table 11 for the electron and muon channels.

TABLE 12. Number of events in the signal region, after all cuts (stat. errors only)

sample	evts±stat. (el)	evts±stat. (mu)
signal (BR($t \to q\gamma$)=10^{-3})	13.05 ± 0.57	19.22 ± 0.71
$t\bar{t}$	6.57 ± 0.67	10.39 ± 0.91
W+jets	0.00 ± 0.00	0.00 ± 0.00
Z+jets	1.59 ± 0.58	0.28 ± 0.13
$t\bar{t}$ +γ	11.56 ± 0.48	17.17 ± 0.61
W+γ +jets	2.84 ± 0.69	3.29 ± 0.70
Z+γ +jets	1.30 ± 0.84	1.19 ± 0.77
Single top	0.52 ± 0.38	0.17 ± 0.10
Single top+γ	0.04 ± 0.02	2.01 ± 0.46
Diboson	0.25 ± 0.22	0.00 ± 0.00
$t\bar{t}$ +V+jets	0.07 ± 0.02	0.12 ± 0.03
total MC	24.75 ± 1.55	34.61 ± 1.59
data	27	31

5.5. Signal Region

Figures 62, 63, 64, and 65 show distributions in the signal region, with final selection cuts and scale factors applied. The signal MC is scaled to BR($t \to q\gamma$) = 0.01%. Table 12 shows the total number of signal and background events in the signal region, after all the final selection cuts.

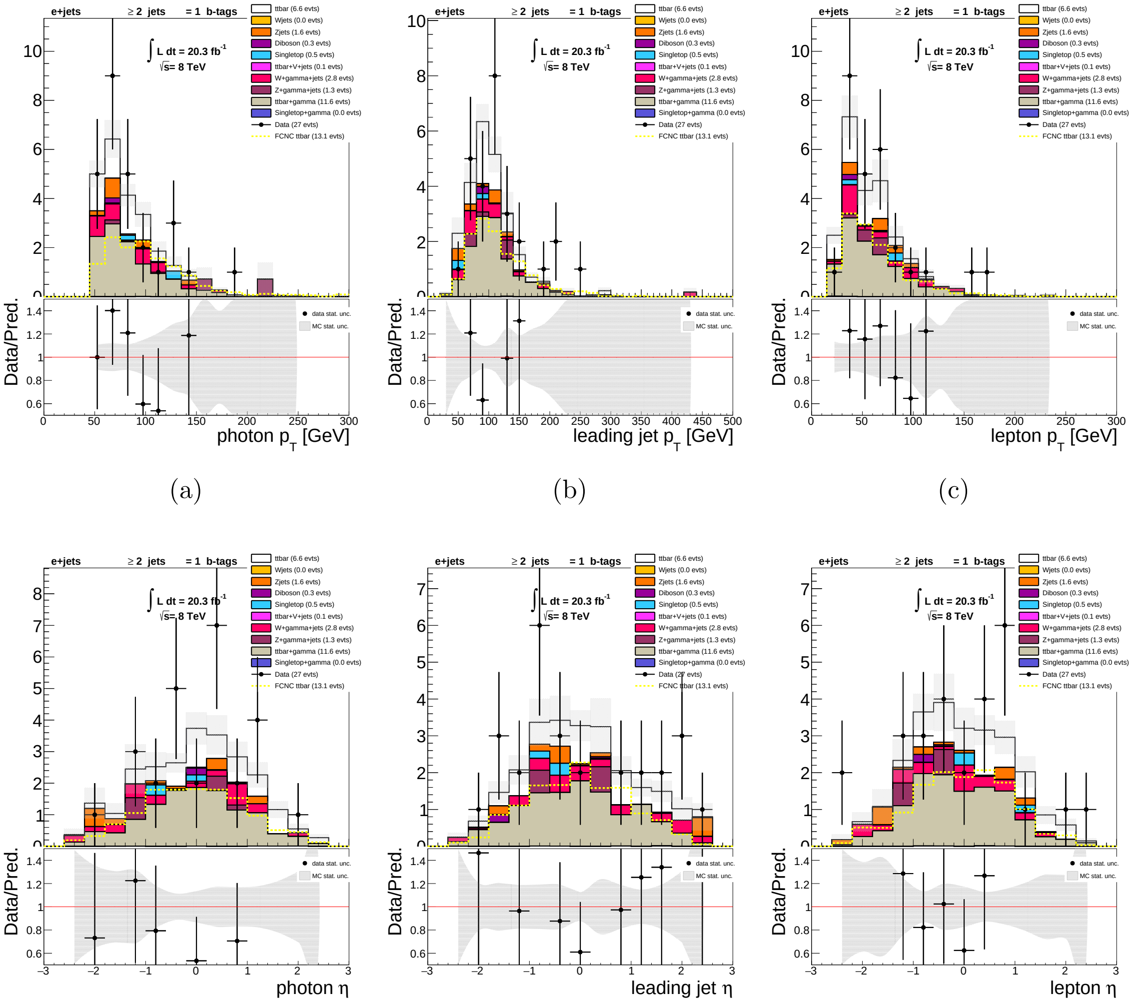

(a) (b) (c)

(d) (e) (f)

FIGURE 62. Photon p_{T} (a), leading jet p_{T} (b), lepton p_{T} (c), photon η (d), leading jet η (e), and lepton η (f) plots in the signal region, with scale factors applied (electron channel)

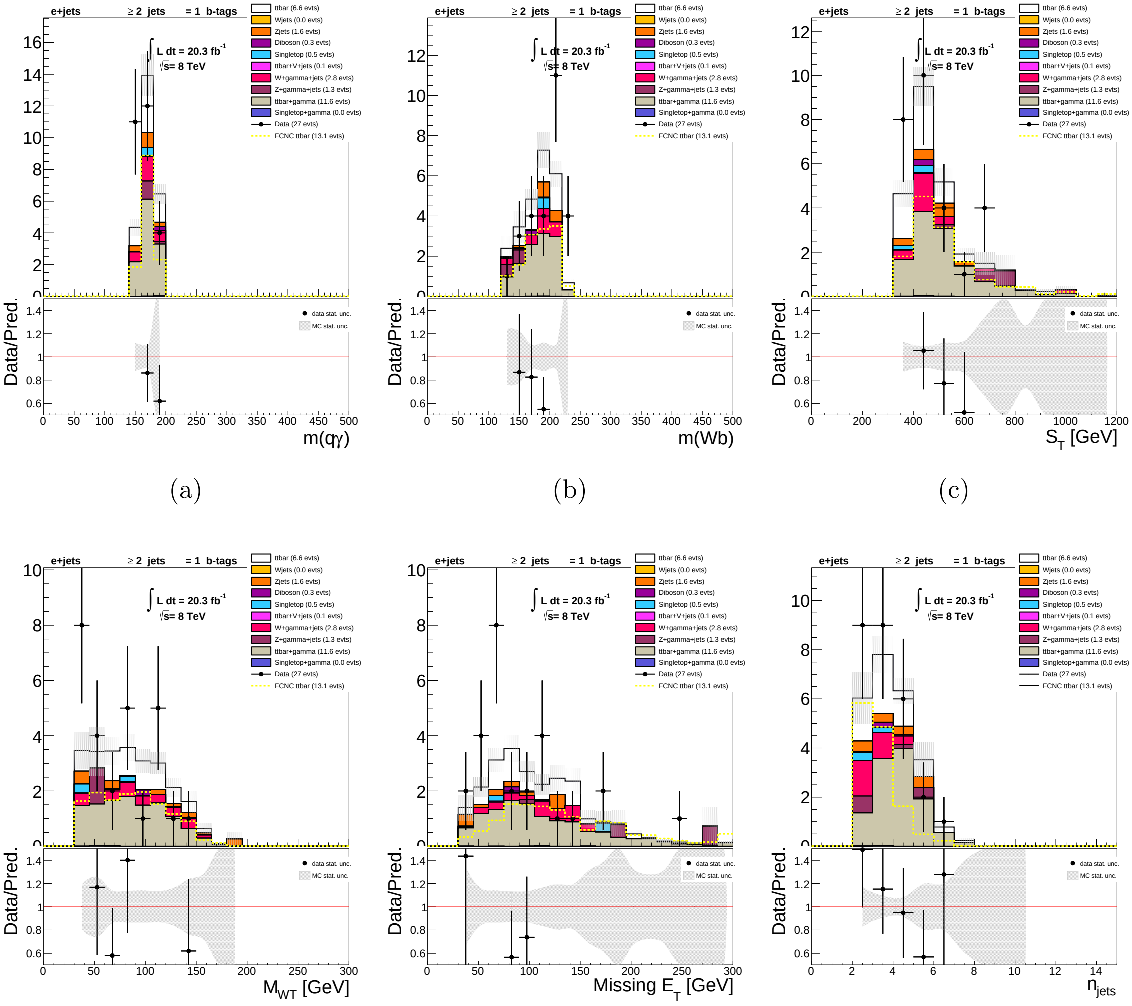

(a) (b) (c)

(d) (e) (f)

FIGURE 63. FCNC top mass (a), SM top mass (b), S$_T$ (c), $m_{\mathrm{T}}^{\mathrm{W}}$(d), $E_{\mathrm{T}}^{\mathrm{miss}}$ (e), and N$_{jets}$ (f) plots in the signal region, with scale factors applied (electron channel)

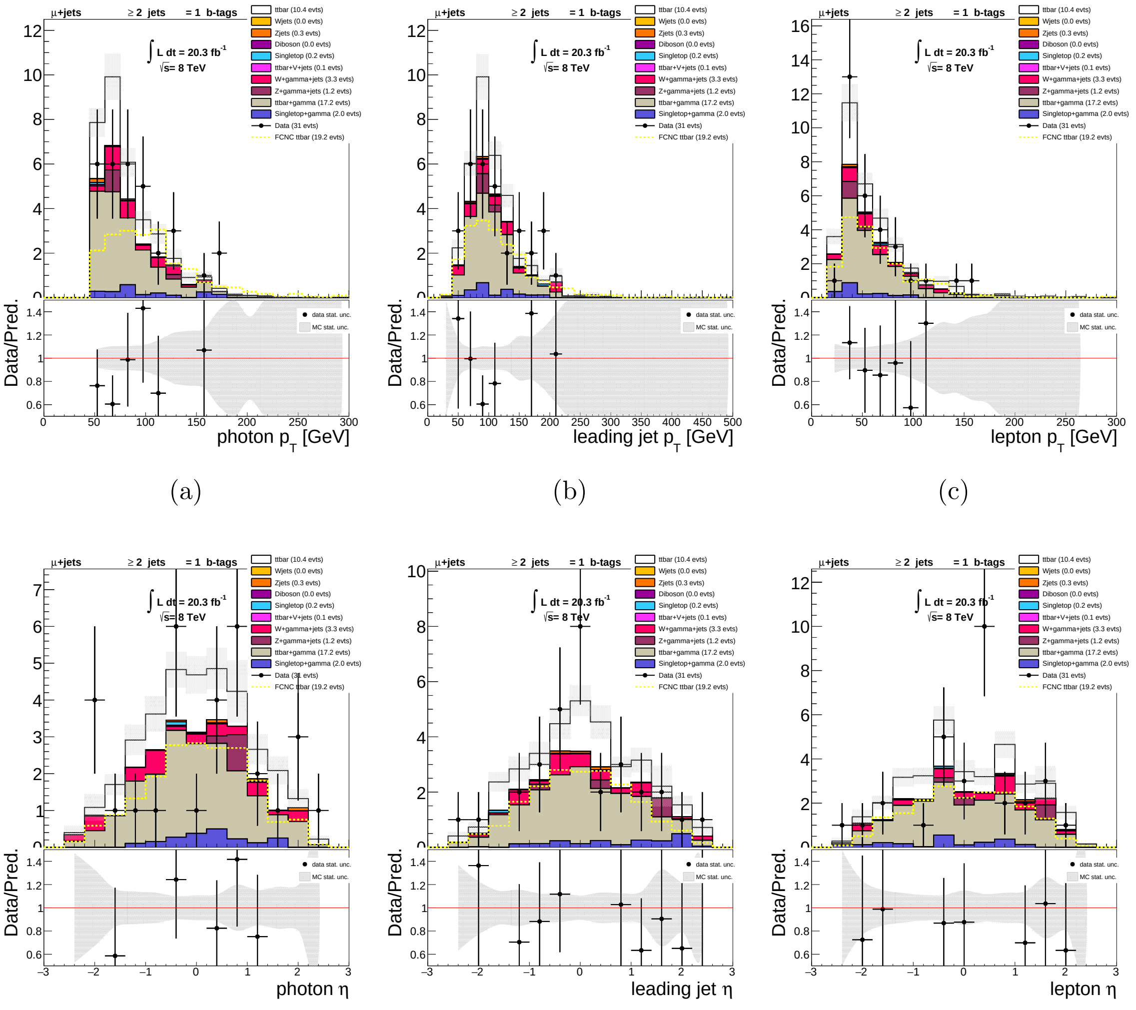

(a) (b) (c)

(d) (e) (f)

FIGURE 64. Photon p_{T} (a), leading jet p_{T} (b), lepton p_{T} (c), photon η (d), leading jet η (e), and lepton η (f) plots in the signal region, with scale factors applied (muon channel)

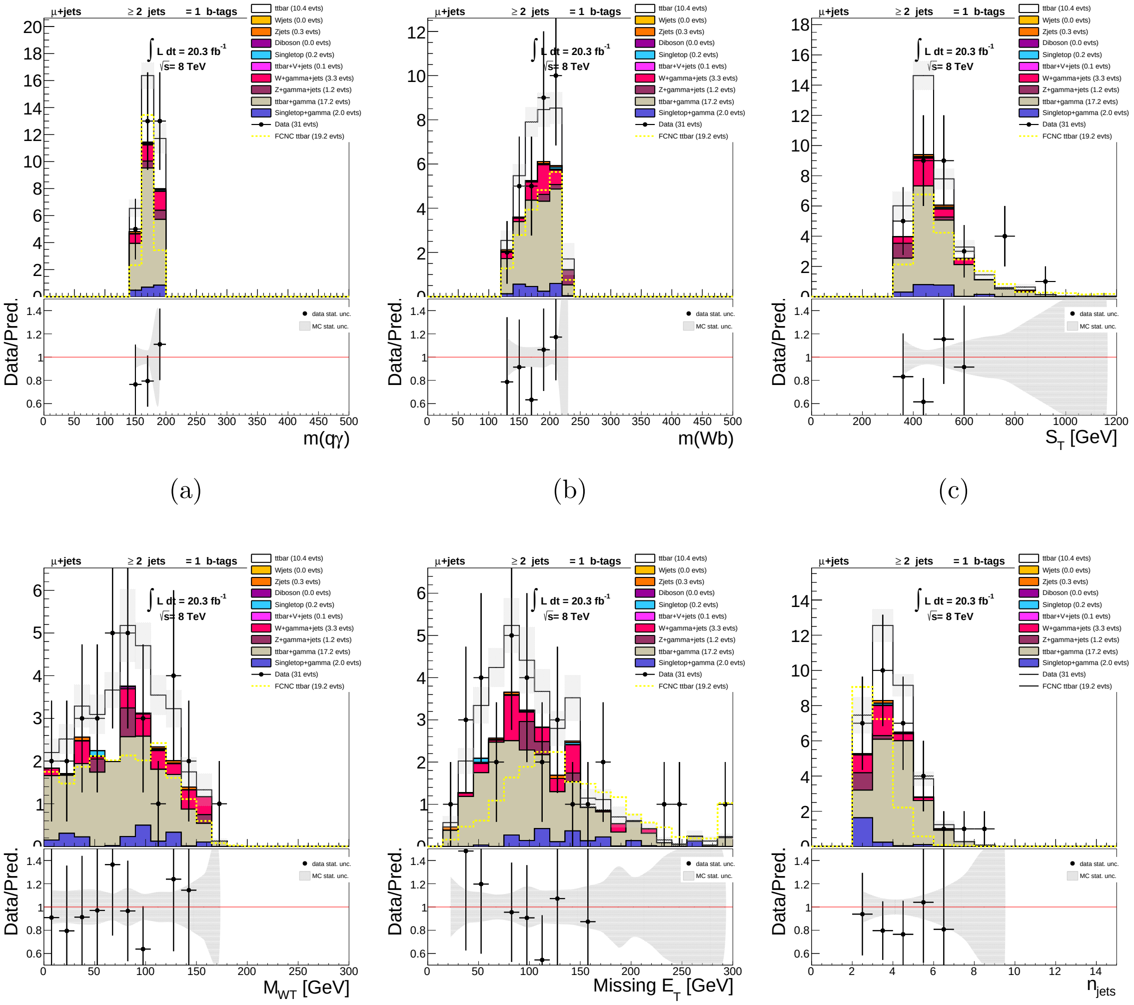

(a) (b) (c)

(d) (e) (f)

FIGURE 65. FCNC top mass (a), SM top mass (b), S$_T$ (c), $m_{\mathrm{T}}^{\mathrm{W}}$(d), $E_{\mathrm{T}}^{\mathrm{miss}}$ (e), and N$_{jets}$ (f) plots in the signal region, with scale factors applied (muon channel)

CHAPTER VI

RESULTS

The purpose of this search is to either observe the FCNC top decay $t \to q\gamma$, or set an upper limit on the branching ratio BR($t \to q\gamma$). As no significant excess of events is observed in data, an upper limit on the branching ratio BR($t \to q\gamma$) will be set. In this chapter, the methods used to set the upper limit on the branching ratio BR($t \to q\gamma$) and to determine the systematic uncertainties on that limit are discussed.

6.1. Systematic Uncertainties

There are systematic uncertainties which influence the observed number of events in data and simulation. Those uncertainties and the tools used to derive them are described below, and enumerated in Tables 13 and 14.

Luminosity: The uncertainty on the integrated luminosity is $\pm 2.8\%$. It is derived, following the same methodology as that detailed in Ref. [79], from a preliminary calibration of the luminosity scale derived from beam-separation scans performed in November 2012.

Lepton Identification and Trigger: Lepton identification and trigger efficiency differ between data and simulation. Scale factors are determined by the Egamma and Muon Combined Performance groups, by comparing $Z \to \ell^+\ell^-$ tag-and-probe techniques in data and Monte Carlo. Scale factors are applied to Monte Carlo.

Electron Reconstruction Efficiency: Scale factors are determined from $Z \to e^+e^-$ tag-and-probe. This systematic is evaluated by varying the scale factors up and down by 1σ and repeating the event selection.

Electron Energy Scale and Resolution: The accuracy of the electron energy scale and resolution in Monte Carlo are validated by comparing $Z \to e^+e^-$ and $J/\psi \to e^+e^-$ mass distributions in data and Monte Carlo.

Muon Reconstruction Efficiency: The muon reconstruction efficiency is different in data and Monte Carlo, so a scale factor is applied to Monte Carlo to bring them into agreement, as recommended by the Muon Combined Performance group. In addition, the muon momentum is smeared in Monte Carlo to make the momentum resolution agree with data.

Muon Momentum Scale and Resolution: The muon momentum scale and resolution are varied, using the method described in [80].

Photon Energy Scale and Resolution: Photon energy scale and resolution are varied in Monte Carlo.

MET Uncertainties: Jet and lepton variations are propagated to $E_{\mathrm{T}}^{\mathrm{miss}}$ when calculating each uncertainty. In addition, uncertainties in MET CellOut and SoftJet scale and resolution are considered.

Jet Energy Scale: The jet energy scale (JES) systematic uncertainty is derived from a variety of sources. In-situ measurements were performed in 8 TeV data to determine the uncertainties due to jet energy scale. Each input to the JES uncertainty depends on modeling, detector, mixed (both detector and modeling), or statistics. Further uncertainties due to flavor composition of the samples used, pileup, and η intercalibration are also considered.

Jet Energy Resolution: As only a small difference is seen in the jet energy resolution (JER) between data and Monte Carlo, the energy of each jet in the Monte Carlo is smeared, the event selection is repeated, and then the difference between the data and MC is taken as a systematic uncertainty, as recommended by the Jet/EtMiss Combined Performance Group.

TABLE 13. Systematic uncertainties (electron channel)

uncertainty	bg stat.	bg syst. (%)	sig stat.	sig syst. (%)
nominal	2.25	–	0.57	—
err_down	2.25	-0.11	0.57	0.05
err_up	2.25	0.30	0.58	-0.74
ees_down	2.25	-0.53	0.58	-0.67
ees_up	2.25	0.49	0.57	0.09
jes_down_EffectiveNP_Statistical1	2.25	0.40	0.57	0.84
jes_down_EffectiveNP_Statistical2	2.25	-0.08	0.57	-0.06
jes_down_EffectiveNP_Statistical3	2.20	2.27	0.57	0.73
jes_down_EffectiveNP_Statistical4	2.25	-0.46	0.57	0.94
jes_down_EffectiveNP_Modelling1	2.10	3.36	0.57	2.01
jes_down_EffectiveNP_Modelling2	2.25	-0.15	0.57	0.12
jes_down_EffectiveNP_Modelling3	2.25	0.49	0.57	0.73
jes_down_EffectiveNP_Modelling4	2.25	-0.18	0.57	0.04
jes_down_EffectiveNP_Detector1	2.21	0.93	0.57	0.42
jes_down_EffectiveNP_Detector2	2.25	0.18	0.57	0.94
jes_down_EffectiveNP_Detector3	2.25	-0.07	0.57	-0.07
jes_down_EffectiveNP_Mixed1	2.25	-0.56	0.57	0.39
jes_down_EffectiveNP_Mixed2	2.25	0.14	0.57	0.11
jes_down_EffectiveNP_Mixed3	2.25	0.42	0.57	0.55
jes_down_EffectiveNP_Mixed4	2.25	0.00	0.57	0.00
jes_down_EtaIntercalibration_Modelling	2.21	1.33	0.57	1.24
jes_down_EtaIntercalibration_TotalStat	2.25	0.01	0.57	0.56
jes_down_MuOffsetTerm	3.51	-10.52	0.57	0.28
jes_down_NPVOffsetTerm	2.10	3.74	0.57	1.92
jes_down_PileupPtTerm	2.25	0.39	0.57	0.49
jes_down_RhoTopology	2.25	0.17	0.57	1.26
jes_down_SingleParticle_HighPt	2.25	0.00	0.57	0.00
jes_down_FlavourComp	2.10	3.17	0.57	2.52
jes_down_FlavourResponse	3.51	-11.44	0.57	-0.27
jes_down_BJESUncert	2.25	-0.32	0.58	-0.48
jes_down_PunchThrough	2.25	0.00	0.57	0.21
jes_up_EffectiveNP_Statistical1	2.25	0.08	0.57	-0.47
jes_up_EffectiveNP_Statistical2	2.25	0.26	0.57	0.25
jes_up_EffectiveNP_Statistical3	2.25	-0.17	0.57	0.03
jes_up_EffectiveNP_Statistical4	2.25	0.46	0.57	0.31
jes_up_EffectiveNP_Modelling1	3.49	-8.47	0.57	1.59
jes_up_EffectiveNP_Modelling2	2.25	0.25	0.57	0.45
jes_up_EffectiveNP_Modelling3	2.25	-0.18	0.57	0.26
jes_up_EffectiveNP_Modelling4	2.25	0.50	0.57	0.12

TABLE 13. (continued)

uncertainty	bg stat.	bg syst. (%)	sig stat.	sig syst. (%)
jes_up_EffectiveNP_Detector1	3.51	-9.19	0.57	1.04
jes_up_EffectiveNP_Detector2	2.25	0.13	0.57	0.05
jes_up_EffectiveNP_Detector3	2.25	0.43	0.57	0.27
jes_up_EffectiveNP_Mixed1	2.24	1.39	0.57	0.76
jes_up_EffectiveNP_Mixed2	2.25	0.11	0.57	0.85
jes_up_EffectiveNP_Mixed3	2.25	-0.18	0.57	0.34
jes_up_EffectiveNP_Mixed4	2.25	0.11	0.57	-0.00
jes_up_EtaIntercalibration_Modelling	2.25	-0.20	0.57	0.15
jes_up_EtaIntercalibration_TotalStat	2.25	0.18	0.57	0.33
jes_up_MuOffsetTerm	2.20	1.74	0.57	0.50
jes_up_NPVOffsetTerm	2.24	0.95	0.57	0.19
jes_up_PileupPtTerm	2.25	0.27	0.57	0.72
jes_up_RhoTopology	3.52	-11.15	0.57	1.39
jes_up_SingleParticle_HighPt	2.25	0.00	0.57	0.00
jes_up_FlavourComp	3.49	-8.83	0.57	1.37
jes_up_FlavourResponse	2.21	1.62	0.57	2.76
jes_up_BJESUncert	2.20	3.09	0.57	1.80
jes_up_PunchThrough	2.25	0.00	0.57	0.21
jeff	2.25	-0.06	0.57	0.00
jer_DataMC_Difference	2.25	0.00	0.57	0.00
jer_up_NP0	2.18	5.34	0.57	0.81
jer_up_NP1	2.20	2.19	0.57	0.27
jer_up_NP2	2.23	3.51	0.57	-0.46
jer_up_NP3	2.20	3.42	0.57	2.74
jer_up_NP4	2.25	-0.52	0.57	0.98
jer_up_NP5	2.23	2.97	0.57	1.81
jer_up_NP6	2.20	3.36	0.57	0.35
jer_up_NP7	2.21	0.67	0.57	0.60
jer_up_NP8	2.25	0.00	0.57	0.00
met_res_soft_down	2.23	0.77	0.57	1.23
met_res_soft_up	3.51	-9.73	0.57	1.55
met_sc_soft_down	3.51	-10.54	0.57	0.13
met_sc_soft_up	2.25	0.22	0.57	0.20
ph_erdown	2.24	0.72	0.57	0.63
ph_erup	2.25	-0.23	0.57	0.12
ph_esdown	2.25	-0.93	0.58	-0.72
ph_esup	2.24	1.43	0.57	2.16

TABLE 14. Systematic uncertainties (muon channel)

uncertainty	bg stat.	bg syst. (%)	sig stat.	sig syst. (%)
nominal	4.62	–	0.71	—
mu_idres	4.62	-0.04	0.71	0.15
mu_msres	4.62	-0.21	0.70	0.68
mu_scaledown	4.62	0.04	0.71	0.05
mu_scaleup	4.62	0.00	0.71	0.10
jes_down_EffectiveNP_Statistical1	4.62	0.75	0.71	0.14
jes_down_EffectiveNP_Statistical2	4.62	0.15	0.71	-0.00
jes_down_EffectiveNP_Statistical3	4.63	-0.20	0.71	-0.35
jes_down_EffectiveNP_Statistical4	4.62	0.15	0.70	0.57
jes_down_EffectiveNP_Modelling1	4.62	0.37	0.70	0.82
jes_down_EffectiveNP_Modelling2	4.62	0.07	0.71	0.16
jes_down_EffectiveNP_Modelling3	4.62	0.29	0.71	-0.21
jes_down_EffectiveNP_Modelling4	4.62	0.45	0.71	-0.01
jes_down_EffectiveNP_Detector1	4.62	-0.08	0.71	0.38
jes_down_EffectiveNP_Detector2	4.62	0.08	0.71	0.13
jes_down_EffectiveNP_Detector3	4.62	0.42	0.71	-0.00
jes_down_EffectiveNP_Mixed1	4.62	0.38	0.70	0.69
jes_down_EffectiveNP_Mixed2	4.62	-0.20	0.71	-0.13
jes_down_EffectiveNP_Mixed3	4.62	0.44	0.71	-0.03
jes_down_EffectiveNP_Mixed4	4.62	0.23	0.71	-0.00
jes_down_EtaIntercalibration_Modelling	4.62	0.39	0.70	0.50
jes_down_EtaIntercalibration_TotalStat	4.62	0.48	0.70	0.57
jes_down_MuOffsetTerm	4.62	0.42	0.71	0.33
jes_down_NPVOffsetTerm	4.63	-0.84	0.70	1.17
jes_down_PileupPtTerm	4.62	-0.38	0.71	0.36
jes_down_RhoTopology	4.62	0.67	0.71	0.55
jes_down_SingleParticle_HighPt	4.62	0.00	0.71	0.00
jes_down_FlavourComp	4.62	1.08	0.70	1.12
jes_down_FlavourResponse	4.62	-0.76	0.71	-0.98
jes_down_BJESUncert	4.62	0.48	0.70	0.61
jes_down_PunchThrough	4.62	-0.07	0.71	-0.01
jes_up_EffectiveNP_Statistical1	4.62	-0.30	0.71	-0.34
jes_up_EffectiveNP_Statistical2	4.62	0.36	0.71	-0.00
jes_up_EffectiveNP_Statistical3	4.62	0.32	0.71	0.29
jes_up_EffectiveNP_Statistical4	4.62	0.14	0.71	-0.16
jes_up_EffectiveNP_Modelling1	4.63	-1.03	0.71	-0.84
jes_up_EffectiveNP_Modelling2	4.62	0.18	0.71	0.01
jes_up_EffectiveNP_Modelling3	4.62	0.02	0.70	0.44
jes_up_EffectiveNP_Modelling4	4.62	0.13	0.71	0.02

TABLE 14. (continued)

uncertainty	bg stat.	bg syst. (%)	sig stat.	sig syst. (%)
jes_up_EffectiveNP_Detector1	4.62	0.21	0.71	0.15
jes_up_EffectiveNP_Detector2	4.62	0.05	0.71	-0.14
jes_up_EffectiveNP_Detector3	4.62	0.01	0.71	0.02
jes_up_EffectiveNP_Mixed1	4.63	-0.34	0.71	0.08
jes_up_EffectiveNP_Mixed2	4.62	0.24	0.71	-0.07
jes_up_EffectiveNP_Mixed3	4.62	-0.07	0.70	0.43
jes_up_EffectiveNP_Mixed4	4.62	-0.03	0.71	-0.00
jes_up_EtaIntercalibration_Modelling	4.62	0.15	0.71	0.24
jes_up_EtaIntercalibration_TotalStat	4.62	-0.46	0.71	-0.20
jes_up_MuOffsetTerm	4.62	-0.05	0.71	-0.29
jes_up_NPVOffsetTerm	4.62	0.19	0.71	-0.63
jes_up_PileupPtTerm	4.62	-0.07	0.71	-0.41
jes_up_RhoTopology	4.63	-0.87	0.71	-0.23
jes_up_SingleParticle_HighPt	4.62	0.00	0.71	0.00
jes_up_FlavourComp	4.63	-1.93	0.71	-0.45
jes_up_FlavourResponse	4.62	0.44	0.70	1.19
jes_up_BJESUncert	4.63	-0.35	0.70	0.45
jes_up_PunchThrough	4.62	0.00	0.71	0.00
jeff	4.62	0.13	0.71	0.06
jer_DataMC_Difference	4.62	0.00	0.71	0.00
jer_up_NP0	4.56	-0.58	0.69	3.81
jer_up_NP1	4.56	0.77	0.70	0.52
jer_up_NP2	4.57	-0.82	0.70	1.12
jer_up_NP3	4.56	0.79	0.71	0.17
jer_up_NP4	4.56	1.63	0.71	-0.13
jer_up_NP5	4.63	-1.55	0.70	2.58
jer_up_NP6	4.62	-0.52	0.71	0.22
jer_up_NP7	4.62	0.04	0.71	-0.32
jer_up_NP8	4.62	0.00	0.71	0.00
met_res_soft_down	4.62	0.09	0.71	0.54
met_res_soft_up	4.62	0.27	0.71	-0.14
met_sc_soft_down	4.62	0.24	0.71	0.07
met_sc_soft_up	4.62	0.15	0.70	0.48
ph_erdown	4.62	0.74	0.71	0.14
ph_erup	4.62	0.15	0.71	-0.25
ph_esdown	4.62	-0.94	0.71	-1.73
ph_esup	4.62	1.36	0.70	1.19

6.2. Statistical Treatment

The CL$_s$ technique [81, 82] is used to set an upper limit on BR($t \rightarrow q\gamma$). A test statistic, q_μ, is constructed to depend on nuisance parameters, $\Theta(\mu)$.

$$q_\mu = -2ln\frac{L(\mu, \Theta(\hat{\hat{\mu}}))}{L(\mu, \Theta(\hat{\mu}))}$$

μ is the signal strength parameter, the ratio of the signal cross section to the predicted signal cross section: $\mu = \frac{\sigma}{\sigma_{prediction}}$, so the background-only hypothesis is fulfilled when $\mu = 0$. In this search,

$$\begin{aligned} \mu &= \frac{\mathrm{BR}(t \rightarrow q\gamma)\mathrm{BR}(t \rightarrow Wb)}{\mathrm{BR}_{\mathrm{ref}}(t \rightarrow q\gamma)\mathrm{BR}_{\mathrm{ref}}(t \rightarrow Wb)} \\ &= \frac{\mathrm{BR}(t \rightarrow q\gamma)[1 - \mathrm{BR}(t \rightarrow q\gamma)]}{\mathrm{BR}_{\mathrm{ref}}(t \rightarrow q\gamma)[1 - \mathrm{BR}_{\mathrm{ref}}(t \rightarrow q\gamma)]} \\ &\sim \frac{\mathrm{BR}(t \rightarrow q\gamma)}{\mathrm{BR}_{\mathrm{ref}}(t \rightarrow q\gamma)} \end{aligned}$$

.

Then, values of μ from 0 to 2 (background-only to 2x the nominal branching ratio) are tested.

$$CL_s = \frac{p_\mu}{1 - p_b} \text{ where } p_\mu = \int_{q_{\mu,obs}}^{\infty} f(q_\mu)dq_\mu, 1 - p_b = \int_{q_{\mu,obs}}^{\infty} f(q_\mu)dq_\mu$$

In order to calculate expected and observed limits, 5,000 toy Monte Carlo simulations were thrown. In the toy Monte Carlos, the nuisance parameters are set to their conditional estimate ($\Theta = \hat{\Theta_\mu}$), while global variables b_0 are varied:

$$L = \text{Pois}(n_{observed}|\mu s + b)\text{Gaus}(b_0|b, \sigma_b)$$

To set expected limits, the p-value was computed for quantiles (median, $\pm 1\sigma$, $\pm 2\sigma$) of the background-only ($\mu = 0$) test statistic distribution, and that value was used for for $q_{observed}$.

6.3. Setting a Limit on BR($t \rightarrow q\gamma$)

Limits were calculated using the CL$_S$ method, implemented in RooStats [83]. Table 15 shows the observed and expected limits separately in the electron and muon channels, and Figure 66 shows the variation in observed and expected CL$_S$ for increasing values of μ. Table 16 shows the combined limit for both channels together. Figure 67 shows the variation in observed and expected CL$_S$ for increasing values of μ, for both the electron and muon channels together.

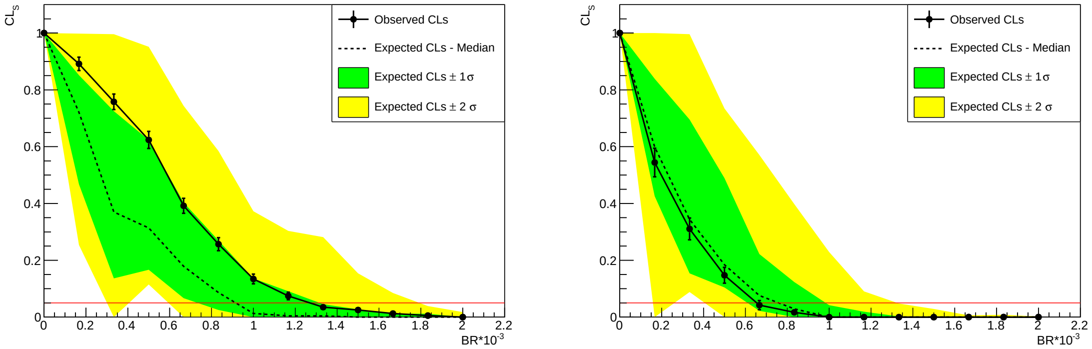

(a) (b)

FIGURE 66. Expected and observed upper limits on the branching ratio BR($t \to q\gamma$) for the electron (a) and muon (b) channels

TABLE 15. Expected and observed upper limits on BR($t \to q\gamma$)

channel	obs. limit	exp. limit -σ	exp. limit	exp. limit +σ
e	$1.27 \pm 0.05 * 10^{-3}$	$0.733 * 10^{-3}$	$0.916 * 10^{-3}$	$1.32 * 10^{-3}$
μ	$0.654 \pm 0.048 * 10^{-3}$	$0.610 * 10^{-3}$	$0.759 * 10^{-3}$	$0.984 * 10^{-3}$

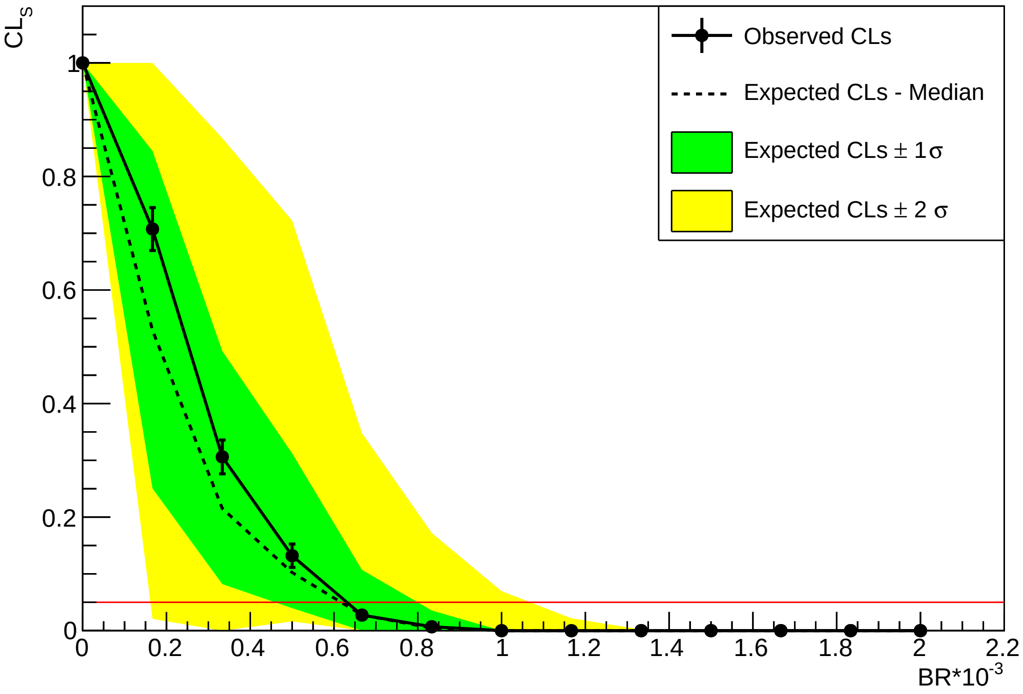

(a)

FIGURE 67. Combined electron and muon channel upper limits on the branching ratio BR($t \rightarrow q\gamma$)

TABLE 16. Combined upper limits on the branching ratio BR($t \rightarrow q\gamma$)

obs. limit	exp. limit -σ	exp. limit	exp. limit $+\sigma$
$0.631 \pm 0.0362 * 10^{-3}$	$0.492 * 10^{-3}$	$0.617 * 10^{-3}$	$0.799 * 10^{-3}$

CHAPTER VII

OUTLOOK AND CONCLUSIONS

The Standard Model of particle physics is hugely successful, and has stood up to the vast majority of experimental tests to date. It is interesting, therefore, to look for ways in which the Standard Model does not work. These broken pieces could be indicative of new physics beyond the Standard Model. This new physics might be something that has already been predicted, or even something else entirely. Top quarks are an ideal portal for new physics searches, since they decay immediately and are produced in very large numbers at the Large Hadron Collider.

7.1. Future Directions

It will be interesting to repeat this search in the ATLAS Run 2 dataset which is being collected now. During Run 2, the Large Hadron Collider is colliding protons at a higher energy, with higher instantaneous luminosity, and with closer spacing between the bunches of protons. With pp collisions at $\sqrt{s} = 13$ TeV, the probability to produce new, heavy particles will increase. At the same time, the $t\bar{t}$ production cross section goes up by almost a factor of three, which means that there will be more top quark pairs produced, and more chances to observe rare top decays. Higher instantaneous luminosity and close bunch spacing will allow the ATLAS experiment to collect data faster. All of these factors will result in a larger and better dataset in which to search for new physics with top quarks.

7.2. Conclusions

A search has been performed for the flavor-changing neutral current in top decays, in the $t\bar{t} \to b\ell\nu q\gamma$ channel. This search was performed in data from proton-proton collisions, collected by the ATLAS detector at the Large Hadron Collider in 2012. The full dataset from 2012 consists of 20.3 fb^{-1} of $\sqrt{s} = 8$ TeV data. As no signal was observed, an observed (expected) upper limit on the branching ratio BR($t \to q\gamma$) of 0.063% (0.062%) was presented.

APPENDIX A

UNITS AND COMMON ABBREVIATIONS

A.1. Natural Units

Particle physics results are presented in natural units, where c (the speed of light - 299,792,458 m/s), $\hbar$ (the reduced Planck constant - 1.054$*10^{-34}$ Js), and k_B (the Boltzmann constant - 1.380$*10^{-23}$ J/K) are set to 1. In this system of units, all quantities can be defined in terms of one unit: the electron-volt. An electron-volt (eV) is the amount of energy needed to accelerate an electron across once volt of potential difference. Physical quantities are then presented in units of electron-volts (eV): mass and energy both have units of eV, while distance and time have units of eV^{-1}. One eV of mass is equivalent to 1.783$*10^{-36}$ kg. The SI prefixes for powers of ten (shown in Table 17) are also used.

Power of ten	Number	Prefix
10^{-15}	0.000000000000001	femto-
10^{-12}	0.000000000001	pico-
10^{-9}	0.000000001	nano-
10^{-6}	0.000001	micro-
10^{-3}	0.001	milli-
10^{-2}	0.01	centi-
10^{-1}	0.1	deci-
10^{0}	1	-
10^{1}	10	deca-
10^{2}	100	hecto-
10^{3}	1000	kilo-
10^{6}	1000000	mega-
10^{9}	1000000000	giga-
10^{12}	1000000000000	tera-
10^{15}	1000000000000000	peta-

TABLE 17. Powers of Ten

A.2. ATLAS Common Abbreviations

A (non-exhaustive) list of the acronyms and abbreviations used by the ATLAS Collaboration:

ADC Analog-to-Digital Converter

ALFA Absolute Luminosity for ATLAS

ATLAS A Toroidal LHC ApparatuS (deprecated)

BCID Bunch Crossing IDentification

BCM Beam Conditions Monitor

CERN European Organization for Nuclear Research

COOL ATLAS-wide conditions database

CSC Cathode Strip Chambers

CTP Central Trigger Processor

DAQ Data AcQuisition system

EF Event Filter

EMEC Electro-Magnetic End-cap Calorimeter

FCAL Forward Calorimeter

FPGA Field-Programmable Gate Array

HEC Hadronic End-cap Calorimeter

HLT High-Level Trigger

JES Jet Energy Scale

JER Jet Energy Resolution

L1Calo Level-1 Calorimeter Trigger

L1 Level-1 Trigger

L2 Level-2 Trigger

LAr Liquid Argon

LHC Large Hadron Collider

LUCID LUminosity measurement using Cerenkov Integrating Detector

MDT Monitoring Drift Tubes

MIP Minimum Ionizing Particle

ROB ReadOut Buffer

ROD ReadOut Driver

RoIB Region of Interest Builder

RoI Region of Interest

RPC Resistive Plate Chambers

SCT SemiConductor Tracker

TDAQ Trigger and Data AcQuisition

TGC Thin Gap Chambers

TileCal Tile Calorimeter

TLA Three Letter Acronym

TRT Transition Radiation Tracker

ZDC Zero Degree Calorimeter

APPENDIX B

DATA AND MC SAMPLE DETAILS

B.1. 2012 ATLAS Data-Taking Periods

Table 18 shows the data-taking periods in 2012 and their corresponding triggers.

Period	Run Numbers	*e* Triggers	μ Triggers	L [pb^{-1}]
A	200804-201556	e24vhi_medium1 + e60_medium1	mu24i_tight + mu36_tight	794
B	202660-205113	e24vhi_medium1 + e60_medium1	mu24i_tight + mu36_tight	5095
C	206248-207397	e24vhi_medium1 + e60_medium1	mu24i_tight + mu36_tight	1406
D	207447-209025	e24vhi_medium1 + e60_medium1	mu24i_tight + mu36_tight	3288
E	209074-210308	e24vhi_medium1 + e60_medium1	mu24i_tight + mu36_tight	2526
G	211522-212272	e24vhi_medium1 + e60_medium1	mu24i_tight + mu36_tight	1275
H	212619-213359	e24vhi_medium1 + e60_medium1	mu24i_tight + mu36_tight	1445
I	213431-213819	e24vhi_medium1 + e60_medium1	mu24i_tight + mu36_tight	1016
J	213900-215091	e24vhi_medium1 + e60_medium1	mu24i_tight + mu36_tight	2596
L	215414-215643	e24vhi_medium1 + e60_medium1	mu24i_tight + mu36_tight	840

TABLE 18. 2012 data periods, triggers, and integrated luminosity after the good runs list has been applied.

B.2. Monte Carlo Samples

Process	Simulation	DSID	Number of Events	Cross Section [pb]	K-Factor
$t\bar{t} \to Wbq\gamma$	fullsim	110605	99999	–	1
$t\bar{t} \to Wbq\gamma$	AFII	110605	200000	–	1
$t\bar{t}$ non-all-hadronic	fullsim	110404	49948212	114.48	1.1995

TABLE 19. Details of the $t\bar{t}$ Monte Carlo samples used in this search.

Process	DSID	Number of Events	Cross Section [pb]	K-Factor
$W \rightarrow e\nu$ + Np0	147025	29464244	8126.7	1.1330
$W \rightarrow e\nu$ + Np1	147026	47936004	1792.7	1.1330
$W \rightarrow e\nu$ + Np2	147027	17495947	542.18	1.1330
$W \rightarrow e\nu$ + Np3	147028	4855289	147.65	1.1330
$W \rightarrow e\nu$ + Np4	147029	5403283	37.736	1.1330
$W \rightarrow e\nu$ + Np5 incl.	147030	2787277	11.962	1.1330
$W \rightarrow \mu\nu$ + Np0	147033	31965655	8127.1	1.1330
$W \rightarrow \mu\nu$ + Np1	147034	43622615	1792.9	1.1330
$W \rightarrow \mu\nu$ + Np2	147035	17611454	542.24	1.1330
$W \rightarrow \mu\nu$ + Np3	147036	4796077	147.66	1.1330
$W \rightarrow \mu\nu$ + Np4	147037	5498881	37.745	1.1330
$W \rightarrow \mu\nu$ + Np5 incl.	147038	2790985	11.970	1.1330
$W \rightarrow \tau\nu$ + Np0	147041	31877158	8127.1	1.1330
$W \rightarrow \tau\nu$ + Np1	147042	48070179	1792.8	1.1330
$W \rightarrow \tau\nu$ + Np2	147043	17586943	542.21	1.1330
$W \rightarrow \tau\nu$ + Np3	147044	4982982	147.61	1.1330
$W \rightarrow \tau\nu$ + Np4	147045	2553295	37.738	1.1330
$W \rightarrow \tau\nu$ + Np5 incl.	147046	794096	11.905	1.1330

TABLE 20. Details of the ALPGEN + PYTHIA OTF W+jets Monte Carlo samples used in this search.

Process	DSID	Number of Events	Cross Section [pb]	K-Factor
$Z \rightarrow e^+e^- +$ Np0	147105	6298988	718.97	1.1800
$Z \rightarrow e^+e^- +$ Np1	147106	8184476	175.70	1.1800
$Z \rightarrow e^+e^- +$ Np2	147107	389996	58.760	1.1800
$Z \rightarrow e^+e^- +$ Np3	147108	894995	15.636	1.1800
$Z \rightarrow e^+e^- +$ Np4	147109	398597	4.0116	1.1800
$Z \rightarrow e^+e^- +$ Np5	147110	229700	1.2592	1.1800
$Z \rightarrow \mu^+\mu^- +$ Np0	147113	6298796	719.16	1.1800
$Z \rightarrow \mu^+\mu^- +$ Np1	147114	8193384	175.74	1.1800
$Z \rightarrow \mu^+\mu^- +$ Np2	147115	389999	58.795	1.1800
$Z \rightarrow \mu^+\mu^- +$ Np3	147116	894799	15.673	1.1800
$Z \rightarrow \mu^+\mu^- +$ Np4	147117	393200	4.0057	1.1800
$Z \rightarrow \mu^+\mu^- +$ Np5	147118	229200	1.2543	1.1800
$Z \rightarrow \tau^+\tau^- +$ Np0	147121	19202764	718.87	1.1800
$Z \rightarrow \tau^+\tau^- +$ Np1	147122	10674582	175.76	1.1800
$Z \rightarrow \tau^+\tau^- +$ Np2	147123	3765893	58.856	1.1800
$Z \rightarrow \tau^+\tau^- +$ Np3	147124	1096994	15.667	1.1800
$Z \rightarrow \tau^+\tau^- +$ Np4	147125	398798	4.0121	1.1800
$Z \rightarrow \tau^+\tau^- +$ Np5	147126	229799	1.2561	1.1800

TABLE 21. Details of the ALPGEN + PYTHIA OTF Z+jets Monte Carlo samples used in this search.

Process	DSID	Number of Events	Cross Section [pb]	K-Factor
$W + b\bar{b}$ + Np0	200256	1599997	52.237	1.1330
$W + b\bar{b}$ + Np1	200257	1398396	45.628	1.1330
$W + b\bar{b}$ + Np2	200258	699398	23.955	1.1330
$W + b\bar{b}$ + Np3 incl.	200259	398397	13.633	1.1330
$W + c\bar{c}$ + Np0	200156	4299592	149.39	1.1330
$W + c\bar{c}$ + Np1	200157	4137891	143.90	1.1330
$W + c\bar{c}$ + Np2	200158	2394394	84.227	1.1330
$W + c\bar{c}$ + Np3 incl.	200159	985295	44.277	1.1330
$W + c$ + Np0	200056	22999046	758.93	1.52
$W + c$ + Np1	200057	8198769	274.47	1.52
$W + c$ + Np2	200058	2090290	71.643	1.52
$W + c$ + Np3	200059	499498	16.482	1.52
$W + c$ + Np4 incl.	200060	199499	4.7824	1.52

TABLE 22. W + heavy flavor + jets Monte Carlo samples
Details of the W + heavy flavor + jets Monte Carlo samples used in this search.

Process	DSID	Number of Events	Cross Section [pb]	K-Factor
$Z \rightarrow e^+e^- + b\bar{b}$ + Np0	200332	1799992	6.5083	1.1800
$Z \rightarrow e^+e^- + b\bar{b}$ + Np1	200333	999896	3.2948	1.1800
$Z \rightarrow e^+e^- + b\bar{b}$ + Np2	200334	994594	1.2546	1.1800
$Z \rightarrow e^+e^- + b\bar{b}$ + Np3 incl.	200335	885392	0.61800	1.1800
$Z \rightarrow \mu^+\mu^- + b\bar{b}$ + Np0	200340	1799797	6.5056	1.1800
$Z \rightarrow \mu^+\mu^- + b\bar{b}$ + Np1	200341	999897	3.2909	1.1800
$Z \rightarrow \mu^+\mu^- + b\bar{b}$ + Np2	200342	999395	1.2585	1.1800
$Z \rightarrow \mu^+\mu^- + b\bar{b}$ + Np3 incl.	200343	880894	0.61808	1.1800
$Z \rightarrow \tau^+\tau^- + b\bar{b}$ + Np0	200348	300000	6.5062	1.1800
$Z \rightarrow \tau^+\tau^- + b\bar{b}$ + Np1	200349	100000	3.2935	1.1800
$Z \rightarrow \tau^+\tau^- + b\bar{b}$ + Np2	200350	50000	1.2485	1.1800
$Z \rightarrow \tau^+\tau^- + b\bar{b}$ + Np3 incl.	200351	49800	0.61363	1.1800
$Z \rightarrow e^+e^- + c\bar{c}$ + Np0	200432	284999	11.763	1.1800
$Z \rightarrow e^+e^- + c\bar{c}$ + Np1	200433	499500	7.1280	1.1800
$Z \rightarrow e^+e^- + c\bar{c}$ + Np2	200434	498997	3.3603	1.1800
$Z \rightarrow e^+e^- + c\bar{c}$ + Np3 incl.	200435	443697	1.7106	1.1800
$Z \rightarrow \mu^+\mu^- + c\bar{c}$ + Np0	200440	298998	11.795	1.1800
$Z \rightarrow \mu^+\mu^- + c\bar{c}$ + Np1	200441	499799	7.1254	1.1800
$Z \rightarrow \mu^+\mu^- + c\bar{c}$ + Np2	200442	499500	3.3694	1.1800
$Z \rightarrow \mu^+\mu^- + c\bar{c}$ + Np3 incl.	200443	443999	1.7003	1.1800
$Z \rightarrow \tau^+\tau^- + c\bar{c}$ + Np0	200448	299000	11.760	1.1800
$Z \rightarrow \tau^+\tau^- + c\bar{c}$ + Np1	200449	199998	7.1410	1.1800
$Z \rightarrow \tau^+\tau^- + c\bar{c}$ + Np2	200450	99800	3.3582	1.1800
$Z \rightarrow \tau^+\tau^- + c\bar{c}$ + Np3 incl.	200451	49400	1.7046	1.1800

TABLE 23. Details of the Alpgen + Pythia OTF Z + heavy flavor + jets Monte Carlo samples used in this search.

Process	DSID	Number of Events	Cross Section [pb]	K-Factor
WW	161995	9992987	32.486	1.6833
ZZ	161996	19988481	12.007	1.5496
WZ	161997	1999999	4.6891	1.9011
t-channel single top ($t \rightarrow W \rightarrow \ell\nu$)	110090	4994481	17.520	1.0500
t-channel single top ($\bar{t} \rightarrow W \rightarrow \ell\nu$)	110091	4999879	9.3932	1.0616
s-channel single top ($t \rightarrow W \rightarrow \ell\nu$)	110119	5999781	1.6424	1.1067
Wt-channel single top (incl.)	110140	999692	20.461	1.0933
$t\bar{t}$ + W + Np0	119353	399497	0.10410	1.1700
$t\bar{t}$ + W + Np1	174830	399896	0.053372	1.1700
$t\bar{t}$ + W + Np2 incl.	174831	399798	0.041482	1.1700
$t\bar{t}$ + Z + Np0	119355	399996	0.067690	1.3500
$t\bar{t}$ + Z + Np1	174832	399995	0.045357	1.3500
$t\bar{t}$ + Z + Np2 incl.	174833	398798	0.039772	1.3500

TABLE 24. Details of the diboson, single top, and $t\bar{t}$+V Monte Carlo samples used in this search.

Process	DSID	Number of Events	Cross Section [pb]	K-Factor
$t\bar{t} + \gamma$	117478	200000	1.4329	1.8
single top ($W \to e\nu$) + γ	185832	799997	0.21984	1
single top ($W \to \mu\nu$) + γ	185833	794999	0.21984	1
single top ($W \to \tau\nu$) + γ	185834	799998	0.21969	1
$W \to e\nu + \gamma$	126739	11798964	162.88	1
$W \to \mu\nu + \gamma$	126742	11798473	162.89	1
$W \to \tau\nu + \gamma$	126856	6559890	162.96	1
$Z \to e^+e^- + \gamma$	145161	8849673	32.298	1
$Z \to \mu^+\mu^- + \gamma$	145162	9178579	32.326	1
$Z \to \tau^+\tau^- + \gamma$	126854	3999409	32.317	1

TABLE 25. Details of the Standard Model + associated photon Monte Carlo samples used in this search.

REFERENCES CITED

[1] S. L. Glashow, Nucl. Phys. **22** (1961) 579–588.

[2] S. Weinberg, Phys. Rev. Lett. **19** (1967) 1264–1266.

[3] A. Salam, Conf. Proc. **C680519** (1968) 367–377.

[4] K. A. Olive et al., Chin. Phys. **C38** (2014) 090001.

[5] F. Abe et al., Phys. Rev. Lett. **74** (1995) 2626–2631, `arXiv:hep-ex/9503002 [hep-ex]`.

[6] S. Abachi et al., Phys. Rev. Lett. **74** (1995) 2632–2637, `arXiv:hep-ex/9503003 [hep-ex]`.

[7] CMS Collaboration, `arXiv:1511.03951 [hep-ex]`.

[8] L. Evans and P. Bryant, JINST **3** (2008) S08001.

[9] J. M. Yang, B.-L. Young, and X. Zhang, Phys. Rev. D **58** (1998) 055001, `arXiv:hep-ph/9705341 [hep-ph]`.

[10] J. A. Aguilar-Saavedra, Acta Phys. Polon. **B35** (2004) 2695–2710, `arXiv:hep-ph/0409342 [hep-ph]`.

[11] ATLAS Collaboration, JHEP **12** (2015) 061, `arXiv:1509.06047 [hep-ex]`.

[12] CMS Collaboration,.

[13] ATLAS Collaboration, JHEP **11** (2015) 211, `arXiv:1508.03372 [hep-ex]`.

[14] CMS Collaboration, Phys. Lett. **B749** (2015) 337–362, `arXiv:1502.07400 [hep-ex]`.

[15] N. Cabibbo, Phys. Rev. Lett. **10** (1963) 531–533. [,648(1963)].

[16] M. Kobayashi and T. Maskawa, Prog. Theor. Phys. **49** (1973) 652–657.

[17] LHCb Collaboration, `arXiv:1506.00903 [hep-ex]`.

[18] D. Atwood, L. Reina, and A. Soni, Phys. Rev. **D55** (1997) 3156–3176, `arXiv:hep-ph/9609279 [hep-ph]`.

[19] J. A. Aguilar-Saavedra and B. M. Nobre, Phys. Lett. **B553** (2003) 251–260, `arXiv:hep-ph/0210360 [hep-ph]`.

[20] J. A. Aguilar-Saavedra, Phys. Rev. **D67** (2003) 035003, `arXiv:hep-ph/0210112 [hep-ph]`. [Erratum: Phys. Rev.D69,099901(2004)].

[21] J. J. Cao, G. Eilam, M. Frank, K. Hikasa, G. L. Liu, I. Turan, and J. M. Yang, Phys. Rev. **D75** (2007) 075021, `arXiv:hep-ph/0702264 [hep-ph]`.

[22] K. Agashe, G. Perez, and A. Soni, Phys. Rev. **D75** (2007) 015002, `arXiv:hep-ph/0606293 [hep-ph]`.

[23] M. Trodden, `arXiv:hep-ph/9805252 [hep-ph]`.

[24] ATLAS Collaboration, Eur. Phys. J. **C76** no. 2, (2016) 55, `arXiv:1509.00294 [hep-ex]`.

[25] ATLAS Collaboration, Eur. Phys. J. **C76** no. 1, (2016) 12, `arXiv:1508.05796 [hep-ex]`.

[26] ATLAS Collaboration, ATLAS-CONF-2013-081 (2013).

[27] H. Abramowicz et al., Phys. Lett. B **708** (2012) 27–36, `arXiv:1111.3901 [hep-ex]`.

[28] H1 Collaboration, F. D. Aaron et al., Phys. Lett. **B678** (2009) 450–458, `arXiv:0904.3876 [hep-ex]`.

[29] DELPHI Collaboration, J. Abdallah et al., Phys. Lett. **B590** (2004) 21–34, `arXiv:hep-ex/0404014 [hep-ex]`.

[30] L3 Collaboration, P. Achard et al., Phys. Lett. **B549** (2002) 290–300, `arXiv:hep-ex/0210041 [hep-ex]`.

[31] CDF Collaboration, F. Abe et al., Phys. Rev. Lett. **80** (1998) 2525–2530.

[32] ATLAS Collaboration, JINST **3** (2008) S08003.

[33] CMS Collaboration, JINST **3** (2008) S08004.

[34] LHCb Collaboration, JINST **3** (2008) S08005.

[35] ALICE Collaboration, JINST **3** (2008) S08002.

[36] C. Lefèvre,, "The CERN accelerator complex.." Dec, 2008.

[37] ATLAS Collaboration, JINST **3** (2008) S08003.

[38] J. Pequenao,, "Computer generated image of the whole ATLAS detector." Mar, 2008.

[39] J. Pequenao,, "Computer generated image of the ATLAS inner detector." Mar, 2008.

[40] J. Pequenao,, "Computer Generated image of the ATLAS calorimeter." Mar, 2008.

[41] J. Pequenao,, "Computer generated image of the ATLAS Muons subsystem." Mar, 2008.

[42] ATLAS Collaboration, Eur. Phys. J. C **72** (2012) 1849, `arXiv:1110.1530 [hep-ex]`.

[43] ATLAS Collaboration, Eur. Phys. J. **C70** (2010) 823–874, `arXiv:1005.4568 [physics.ins-det]`.

[44] M. L. Mangano et al., JHEP **0307** (2003) 001, `arXiv:hep-ph/0206293 [hep-ph]`.

[45] G. Corcella et al., JHEP **0101** (2001) 010, `arXiv:hep-ph/0011363 [hep-ph]`.

[46] J. Alwall, M. Herquet, F. Maltoni, O. Mattelaer, and T. Stelzer, JHEP **1106** (2011) 128, `arXiv:1106.0522 [hep-ph]`.

[47] P. Nason, JHEP **0411** (2004) 040, `arXiv:hep-ph/0409146 [hep-ph]`.

[48] S. Frixione, P. Nason, and C. Oleari, JHEP **0711** (2007) 070, `arXiv:0709.2092 [hep-ph]`.

[49] J. A. Aguilar-Saavedra, Nucl. Phys. **B812** (2009) 181–204, `arXiv:0811.3842 [hep-ph]`.

[50] J. A. Aguilar-Saavedra, Nucl. Phys. **B837** (2010) 122–136, `arXiv:1003.3173 [hep-ph]`.

[51] T. Sjostrand, S. Mrenna, and P. Z. Skands, JHEP **0605** (2006) 026, `arXiv:hep-ph/0603175`.

[52] T. Gleisberg, S. Hoche, F. Krauss, M. Schonherr, S. Schumann, et al., JHEP **0902** (2009) 007, `arXiv:0811.4622 [hep-ph]`.

[53] S. Hoche, F. Krauss, S. Schumann, and F. Siegert, JHEP **0905** (2009) 053, `arXiv:0903.1219 [hep-ph]`.

[54] T. Gleisberg and S. Hoche, JHEP **0812** (2008) 039, `arXiv:0808.3674 [hep-ph]`.

[55] S. Schumann and F. Krauss, JHEP **0803** (2008) 038, `arXiv:0709.1027 [hep-ph]`.

[56] M. Schonherr and F. Krauss, JHEP **0812** (2008) 018, `arXiv:0810.5071 [hep-ph]`.

[57] J. Alwall et al., Comput. Phys. Commun. **176** (2007) 300–304, `arXiv:hep-ph/0609017 [hep-ph]`.

[58] GEANT4 Collaboration, S. Agostinelli et al., Nucl. Instrum. Meth. **A506** (2003) 250–303.

[59] J. Pequenao and P. Schaffner,, "A computer generated image representing how ATLAS detects particles." Jan, 2013.

[60] ATLAS Collaboration, ATLAS-CONF-2014-032 (2014).

[61] ATLAS Collaboration, Eur. Phys. J. **C74** no. 7, (2014) 2941, `arXiv:1404.2240 [hep-ex]`.

[62] M. Cacciari, G. P. Salam, and G. Soyez, JHEP **04** (2008) 063, `arXiv:0802.1189 [hep-ph]`.

[63] ATLAS Collaboration, ATL-PHYS-PUB-2014-014 (2014).

[64] ATLAS Collaboration, ATLAS-CONF-2013-082 (2013).

[65] ATLAS Collaboration, ATLAS-CONF-2012-123 (2012).

[66] ATLAS Collaboration, Eur. Phys. J. **C74** no. 11, (2014) 3130, `arXiv:1407.3935 [hep-ex]`.

[67] ATLAS Collaboration, ATLAS-CONF-2013-088 (2013).

[68] ATLAS Collaboration, ATL-COM-DAQ-2015-091 (2015).

[69] ATLAS Collaboration, Eur. Phys. J. **C75** (2015) 120, `arXiv:1408.3179 [hep-ex]`.

[70] J. Pumplin et al., JHEP **07** (2002) 012, `arXiv:hep-ph/0201195`.

[71] H.-L. Lai, M. Guzzi, J. Huston, Z. Li, P. M. Nadolsky, J. Pumplin, and C. P. Yuan, Phys. Rev. **D82** (2010) 074024, `arXiv:1007.2241 [hep-ph]`.

[72] ATLAS Collaboration, ATL-PHYS-PUB-2014-008 (2014).

[73] M. Czakon and A. Mitov, Comput. Phys. Commun. **185** (2014) 2930, `arXiv:1112.5675 [hep-ph]`.

[74] M. Botje et al., `arXiv:1101.0538 [hep-ph]`.

[75] A. D. Martin, W. J. Stirling, R. S. Thorne, and G. Watt, Eur. Phys. J. **C64** (2009) 653–680, `arXiv:0905.3531 [hep-ph]`.

[76] J. Gao, M. Guzzi, J. Huston, H.-L. Lai, Z. Li, P. Nadolsky, J. Pumplin, D. Stump, and C. P. Yuan, Phys. Rev. **D89** no. 3, (2014) 033009, `arXiv:1302.6246 [hep-ph]`.

[77] R. D. Ball et al., Nucl. Phys. **B867** (2013) 244–289, `arXiv:1207.1303 [hep-ph]`.

[78] ATLAS Collaboration, ATLAS-CONF-2014-058 (2014).

[79] ATLAS Collaboration, Eur. Phys. J. **C73** no. 8, (2013) 2518, `arXiv:1302.4393 [hep-ex]`.

[80] ATLAS Collaboration, ATLAS-CONF-2011-003 (2011).

[81] A. L. Read, J. Phys. **G28** (2002) 2693–2704.

[82] T. Junk, Nucl. Instrum. Meth. **A434** (1999) 435–443, `arXiv:hep-ex/9902006 [hep-ex]`.

[83] K. Cranmer, G. Lewis, L. Moneta, A. Shibata, and W. Verkerke, CERN-OPEN-2012-016 (2012).